LA-7453-T
Thesis

Quasielastic Pion Scattering near the (3, 3) Resonance

University of California

LOS ALAMOS SCIENTIFIC LABORATORY
Post Office Box 1663 Los Alamos, New Mexico 87545

LA-7453-T
Thesis

UC-34c
Issued: December 1978

Quasielastic Pion Scattering near the (3, 3) Resonance

Philip Varghese*

*Guest Scientist. Telos Computing, Inc., 3231 Ocean Park Boulevard, Santa Monica, CA 90405

CONTENTS

ABSTRACT xi

CHAPTER

I PION INTERACTIONS 1

II QUASIELASTIC PION SCATTERING 19

III THEORETICAL CONSIDERATIONS 40

IV EXPERIMENTAL DETAILS 97

V DATA ANALYSIS AND RESULTS 123

ACKNOWLEDGMENTS 152

APPENDIX A 153

APPENDIX B 156

APPENDIX C 161

APPENDIX D 165

APPENDIX E 170

APPENDIX F 177

REFERENCES 182

LIST OF TABLES

Table		Page
I-1	Expansion of $\|\pi,N\rangle$ states in terms of $\|T, T_z\rangle$ states	5
I-2	Representation of πP differential cross section below 300 MeV in terms of phase shifts	9
III-1	Representation of matrix elements Mij in terms of σ's	49
III-2	Input parameters to QUASEX	54
III-3	P's and Q's and the theoretical ratio of π^+ to π^- cross sections for (π,p) measurement on:	
(a)	^{12}C; $\theta_p = 55°$	58
(b)	^{27}Al; $\theta_p = 55°$	59
(c)	^{63}Cu; $\theta_p = 55°$	60
(d)	^{208}Pb; $\theta_p = 55°$	61
(e)	^{12}C; $\theta_p = 64°$	62
(f)	^{27}Al; $\theta_p = 64°$	63
(g)	^{63}Cu; $\theta_p = 64°$	64
(h)	^{208}Pb; $\theta_p = 64°$	65
III-4	Parameters entering the $(\pi,\pi p)$ calculation for $T_\pi = 255$ MeV:	
(a)	^{12}C; θ_p, $\theta_\pi = 55°$, 50°	72
(b)	^{27}Al; θ_p, $\theta_\pi = 55°$, 50°	73
(c)	^{63}Cu; θ_p, $\theta_\pi = 55°$, 50°	74
(d)	^{208}Pb; θ_p, $\theta_\pi = 55°$, 50°	75
(e)	^{12}C; θ_p, $\theta_\pi = 64°$, 37.5°	76
(f)	^{27}Al; θ_p, $\theta_\pi = 64°$, 37.5°	77
(g)	^{63}Cu; θ_p, $\theta_\pi = 64°$, 37.5°	78
(h)	^{208}Pb, θ_p, $\theta_\pi = 64°$, 37.5°	79

Table		Page
III-5	P's and Q's and the theoretical ratio of π^+ to π^- cross section from the $(\pi,\pi p)$ calculations with σ_N, abs $\neq$ 0:	
(a)	^{12}C; θ_p, θ_π = 55°, 50°	80
(b)	^{27}Al; θ_p, θ_π = 55°, 50°	81
(c)	^{63}Cu; θ_p, θ_π = 55°, 50°	82
(d)	^{208}Pb; θ_p, θ_π = 55°, 50°	83
(e)	^{12}C; θ_p, θ_π = 55°, 50°	84
(f)	^{27}Al; θ_p, θ_π = 55°, 50°	85
(g)	^{63}Cu; θ_p, θ_π = 55°, 50°	86
(h)	^{208}Pb, θ_p, θ_π = 55°, 50°	87
III-6	P's and Q's and the theoretical ratios of π^+ to π^- cross sections from the $(\pi,\pi P)$ calculations with σ_N, abs $\neq$ 0:	
(a)	^{12}C; θ_p, θ_π = 55°, 50°	88
(b)	^{27}Al; θ_p, θ_π = 55°, 50°	89
(c)	^{63}Cu; θ_p, θ_π = 55°, 50°	90
(d)	^{208}Pb; θ_p, θ_π = 55°, 50°	91
(e)	^{12}C; θ_p, θ_π = 64°, 37.5°	92
(f)	^{27}Al; θ_p, θ_π = 64°, 37.5°	93
(g)	^{63}Cu; θ_p, θ_π = 64°, 37.5°	94
(h)	^{208}Pb; θ_p, θ_π = 64°, 37.5°	95
IV-1	Detection Equipment Details	103
IV-2	MWPC Calibration Parameters	116
IV-3	Calibration Parameters for Counters	119
V-1	List of parameters calculated by QUASEL	127
V-2	Measured π^+ and π^- differential cross sections for ^{27}Al:	
(a)	θ_p = 45°	137

Table		Page
(b)	$\theta_p = 55°$	138
(c)	$\theta_p = 64°$	139
(d)	$\theta_p = 90°$	140
V-3	Measured π^+ and π^- differential cross sections for ^{208}Pb:	
(a)	$\theta_p = 45°$	141
(b)	$\theta_p = 55°$	142
(c)	$\theta_p = 64°$	143
V-4	Ratio of π^+ to π^- cross sections from singles data for ^{27}Al and ^{208}Pb	144
V-5	Ratio of π^+ to π^- cross sections from coincidence data for ^{27}Al and ^{208}Pb	146

LIST OF FIGURES

Figure		Page
1(a)	$\pi^+ p$ total cross section in the energy region 0-2 GeV	6
1(b)	$\pi^- p$ total cross section in the energy region 0-2 GeV	7
2(a)	$\pi^- p$ total cross section in the (3,3) resonance region	12
2(b)	$\pi^+ p$ total cross section in the (3,3) resonance region	13
3	Total cross section for π^+ scattering from light nuclei	15
4	Quasielastic scattering process in the PWIA	21
5	Diagram of quasielastic scattering	21
6	Variation of pion mean-free path as a function of T_π near the (3,3) resonance	24
7	Energy spectrum of (π,π^1) scattering	26
8	Observed ratio of π^- to π^+ cross sections for ^{12}C	32
9	Charge exchange model predictions for π^- to π^+ cross sections for ^{12}C	35
10	Geometry of semiclassical charge-exchange model-single arm measurement	42
11	Semiclassical charge exchange model predictions for the ratio of π^+ to π^- cross sections for $\theta_p = 55°$	56
12	Semiclassical charge exchange model predictions for the ratio of π^+ to π^- cross sections for $\theta_p = 64°$	57
13	Geometry for $(\pi,\pi p)$ calculations	67
14	Predicted ratios of π^+ to π^- cross sections for θ_p, θ_π = 55°, 50°	70
15	Predicted ratios of π^+ to π^- cross sections for θ_p, θ_π = 64°, 37.5°	71

Figure		Page
16	Overview of LAMPF	98
17	Major elements of EPICS channel	100
18	General view of the arrangement of the detector system	102
19	Design of the two-dimensional delay-line readout helical chambers	105
20	π^+ and π^- rates	108
21	Schematic of EVENT fast logic	109
22	π^-p coincidence logic	111
23	Diagram of the electronics setup	112
24	Time signals from TDC's	115
25	Projections of particle trajectories to the target	118
26	$E - \frac{dE}{dx}$ plot for proton arm	120
27	Simplified flow chart of QUASEL	124
28	Particle ID gates	128
29	Measured differential cross sections--singles data	
(a)	^{27}Al; $\theta_p = 45°$	130
(b)	^{27}Al; $\theta_p = 55°$	131
(c)	^{27}Al; $\theta_p = 64°$	132
(d)	^{27}Al; $\theta_p = 90°$	133
(e)	^{208}Pb; $\theta_p = 45°$	134
(f)	^{208}Pb; $\theta_p = 55°$	135
(g)	^{208}Pb; $\theta_p = 64°$	136
30	Typical coincidence spectra	147
31	Observed variation of π^+ to π^- ratio with atomic number A:	
(a)	θ_p, $\theta_\pi = 55°$, 50°	150
(b)	θ_p, $\theta_\pi = 64°$, 37.5°	151

QUASIELASTIC PION SCATTERING NEAR THE (3,3) RESONANCE

by

Philip Varghese

ABSTRACT

The quasielastic pion scattering process $(\pi,\pi p)$, in which an energetic pion scatters off a target nucleus, knocking-out a bound proton, has been studied to determine the role of recoil nucleon charge exchange in the mechanism of the process near the (3,3) free particle pion-nucleon resonance, Calculations, which incorporate the hypothesis of final state charge exchange of the outgoing nucleon, were performend to predict expectations for observing the process. Experimental measurements were made on ^{27}Al and ^{208}Pb, using 255-MeV π^+ and π^- beams. The outgoing protons were observed in a counter telescope in singles and coincidence modes.

Singles spectra were measured at proton angles $\theta_p = 45^\circ$, 55°, 64° and 90° and cross sections were calculated as a function of the energy of the detected proton, for each of the targets. Values of the ratio of π^+ to π^- cross sections were calculated for each of the angles of observation. The results obtained indicate that the singles spectra contain events from processes other than quasielastic scattering and that the quasielastic events cannot be easily disentangled from the large background due to such events. The study has thus established the inadequecy of observing quasielastic pion scattering in a single arm measurement.

Coincidence measurements were made by observing the recoil protons in coincidence with the scattered pions, which were detected in a scintillator counter telescope. The ratio of π^+ to π^- cross sections were obtained for each target for the angular settings, (θ_p, θ_π) = $(55^o, 50^o)$ and $(64^o, 37.5^o)$. The measured values of 7.0 ± 0.7 for ^{27}Al and 4.5 ± 0.5 for ^{208}Pb are substantially below the impulse approximation no-charge-exchange limit of 9. The observed A dependance of this cross section ratio is in agreement with the predictions of the semiclassical charge exchange model, showing the influence of charge exchange by the outgoing nucleon.

CHAPTER I

PION INTERACTIONS

INTRODUCTION

Processes involving the interaction of the pion with nuclear matter have been at the center of attention in nuclear physics, ever since the particle was discovered by Lattes, Muirhead, Occhialini and Powell[1] in 1947. The interest in the study of such processes arises largely from the fact that the pion is the elementary mediator of the strong force, which makes the response of nuclear matter to the field of external pions, a subject of fundamental importance in the study of nuclear phenomena. After a quarter of a century of pioneering and exploratory investigations, which revealed a number of interesting features of pion interactions, pion physics entered a new era in the early 1970's, when the new meson factories became operational. Prior to this, studies of pion interactions were performed with low intensity pion beams from the old generation accelerators and, because of the poor quality of the data obtained, the knowledge of pion interaction mechanisms remained rather nebulous. The new meson facilities have the capability of producing high intensity pion beams with good energy resolution. Thus, it is now possible to study pion physics with considerable precision experimentally. The promise of new and more reliable data from the meson factories has greatly enhanced the prospect of making substantial progress in understanding pion interaction mechanisms in the near future.

Several authors have reviewed the status of pion physics in recent years[2-5]. For the purpose of establishing trends, some of the properties of the pion and some features of its interactions with the nucleon and the nucleus will be discussed in the following sections of this introductory chapter.

PION PROPERTIES

The pion is a pseudoscalar boson, having zero spin and negative intrinsic parity ($J_\pi=0^-$). It is also an isovector particle (T=1) and, therefore, comes in three-charge states, π^+, π^o, and π^-, corresponding to T_z=+1, 0, and -1 respectively. The mass of the charged pion is 139.6 MeV and that of the neutral pion is about 135 MeV.

In view of these properties, the pion enjoys a special status among the nuclear probes. Since the pion is a boson, it can be created or destroyed singly in an interaction process. In this respect, among all other particles which can interact with the nucleus, the photon most resembles the pion. Its isovector aspect gives it the capability to access high-isospin states and nuclear species. The double-charge exchange (DCE) reactions (π^+,π^-) and (π^-,π^+) are totally unique since no equivalent reactions are possible with conventional nuclear projectiles[6]. Such reactions can lead to a span of T values in the residual nuclei, ranging from $T=T_z-2$ to $T=T_z+2$; this is an exotic feature which is not available in any other reaction.

There are several key advantages in using pions as nuclear probes. For example, since the pion mass is about one seventh the mass of the nucleon, the pion is the lightest among the strongly

interacting particles. Thus, recoil corrections are less severe in pion nucleon scattering than they are in the scattering of other strongly interacting particles. Another advantage is that, since the pion spin is zero, scattering of pions by nucleons involves fewer amplitudes than the nucleon-nucleon scattering. Moreover, in pion-nucleus collisions, since the incident pion remains distinguishable from the nucleons that make up the nucleus, antisymmetrization of the wave function with respect to the projectile becomes unnecessary in describing the process.

The hadronic nature of the pion permits the use of the particle in probing the distribution of hadronic matter in parallel to the probing of the electromagnetic charge distribution by electron scattering. A precise determination of the hadronic distribution is closely dependent on how well the elementary interaction of the pion with nucleon is understood. Consequently, the dynamics of the pion nucleon system has been the subject of numerous investigations from the very early stages of pion physics.

THE PION NUCLEON SYSTEM

Since the isospins of the pion and the nucleon are 1 and 1/2 respectively, the isospin of the combined πN system can have values T=3/2 or T=1/2. The possible values of T_z are then: $T_z = \pm 3/2, \pm 1/2$ for T-3/2 and $T_z = \pm 1/2$ for $T = 1/2$. Because the nuclear force is charge independent, the interaction of a pion and a nucleon, of definite angular momentum J and parity, depends only on their combined isospin[7]. Therefore, in the theoretical analysis of the pion-nucleon interaction,

it is convenient to represent the particular pion-nucleon state $|\pi,N\rangle$ in terms of the isospin eigenstates $|T,T_z\rangle$. This representation is given in Table I-1.

Most of the information concerning the πN interaction comes from πN scattering experiments. Following the pioneering works of Fermi and his collaborators[8], numerous experiments have been performed, studying the pion-nucleon scattering process over a wide range of energies. Figures 1(a) and 1(b) summarize the results of total cross section measurements for $\pi^{\pm}p$ scattering in the energy range $0<T_\pi<2$ GeV[9-11]. One immediately notices that there is a large energy variation in the cross section; it shows a number of peaks distinctive of resonances. This is quite unlike the NN cross section, which decreases smoothly with increasing energy. At low energies, the NN cross section is orders of magnitude larger than the πN cross section, but at higher energies, they become comparable. Analysis of the πN total cross section data in terms of the pure isospin states of the πN system indicates that many of the peaks in the cross section are true resonances in one of these states[12-14].

The most striking feature of the πN scattering process is the strong and wide ($\Gamma\simeq100$ MeV) peak in the total cross section occuring at about 175 MeV incident pion (Lab) energy. The present understanding of the origin of this peak is based on the following observations: Analysis of the πp scattering data below 300 MeV indicates that in this energy region, the scattering involves mainly S and P waves.

TABLE I-1

Expansion of $|\pi,N\rangle$ states of the πN system in terms of the isospin eigenstates $|T,T_z\rangle$

$$|\pi^+,p\rangle = |\tfrac{3}{2},\tfrac{3}{2}\rangle$$

$$|\pi^0,p\rangle = \sqrt{2/3}\,|\tfrac{3}{2},\tfrac{1}{2}\rangle - \sqrt{1/3}\,|\tfrac{1}{2},\tfrac{1}{2}\rangle$$

$$|\pi^-,p\rangle = \sqrt{1/3}\,|\tfrac{3}{2},\tfrac{1}{2}\rangle - \sqrt{2/3}\,|\tfrac{1}{2},\tfrac{-1}{2}\rangle$$

$$|\pi^+,n\rangle = \sqrt{1/3}\,|\tfrac{3}{2},\tfrac{1}{2}\rangle + \sqrt{2/3}\,|\tfrac{1}{2},\tfrac{1}{2}\rangle$$

$$|\pi^0,n\rangle = \sqrt{2/3}\,|\tfrac{3}{2},\tfrac{-1}{2}\rangle + \sqrt{1/3}\,|\tfrac{1}{2},\tfrac{-1}{2}\rangle$$

$$|\pi^-,n\rangle = |\tfrac{3}{2},\tfrac{-3}{2}\rangle$$

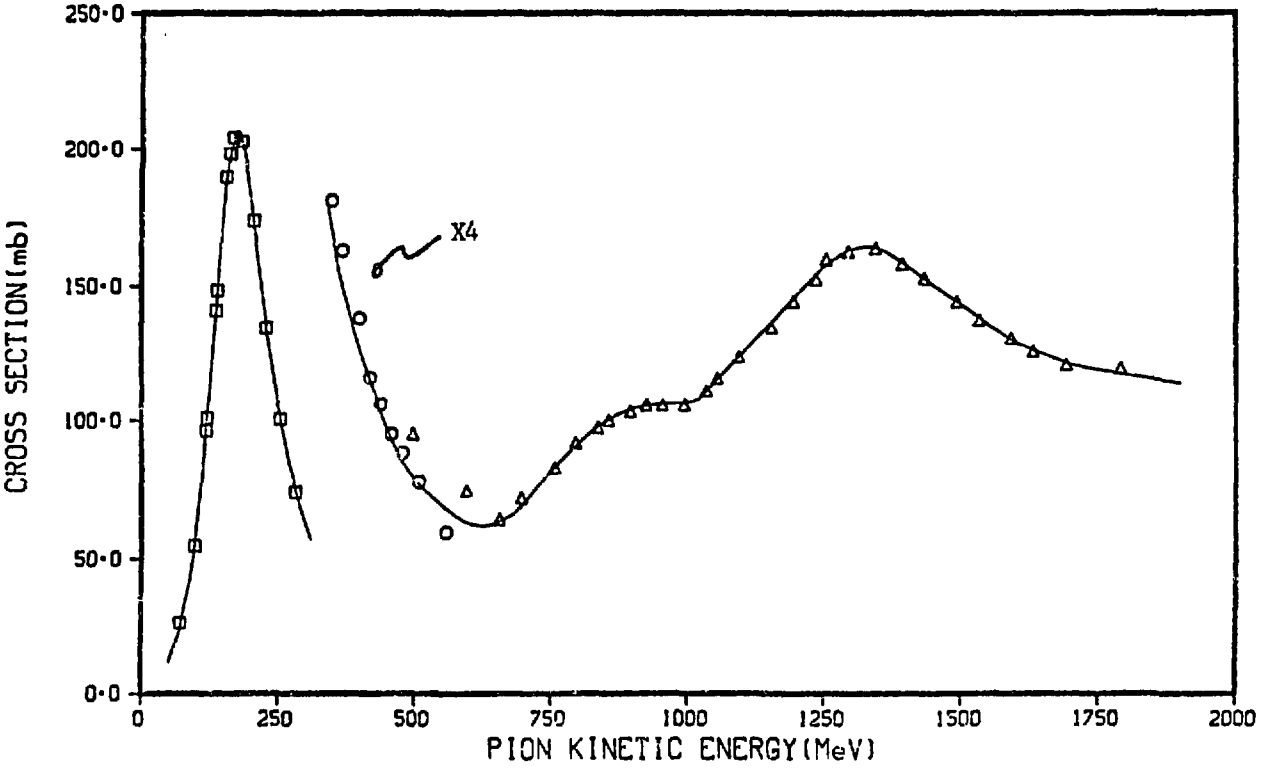

Fig. 1(a). $\pi^+ p$ total cross section in the energy region $0 < T_\pi < 2$ GeV[9-11].

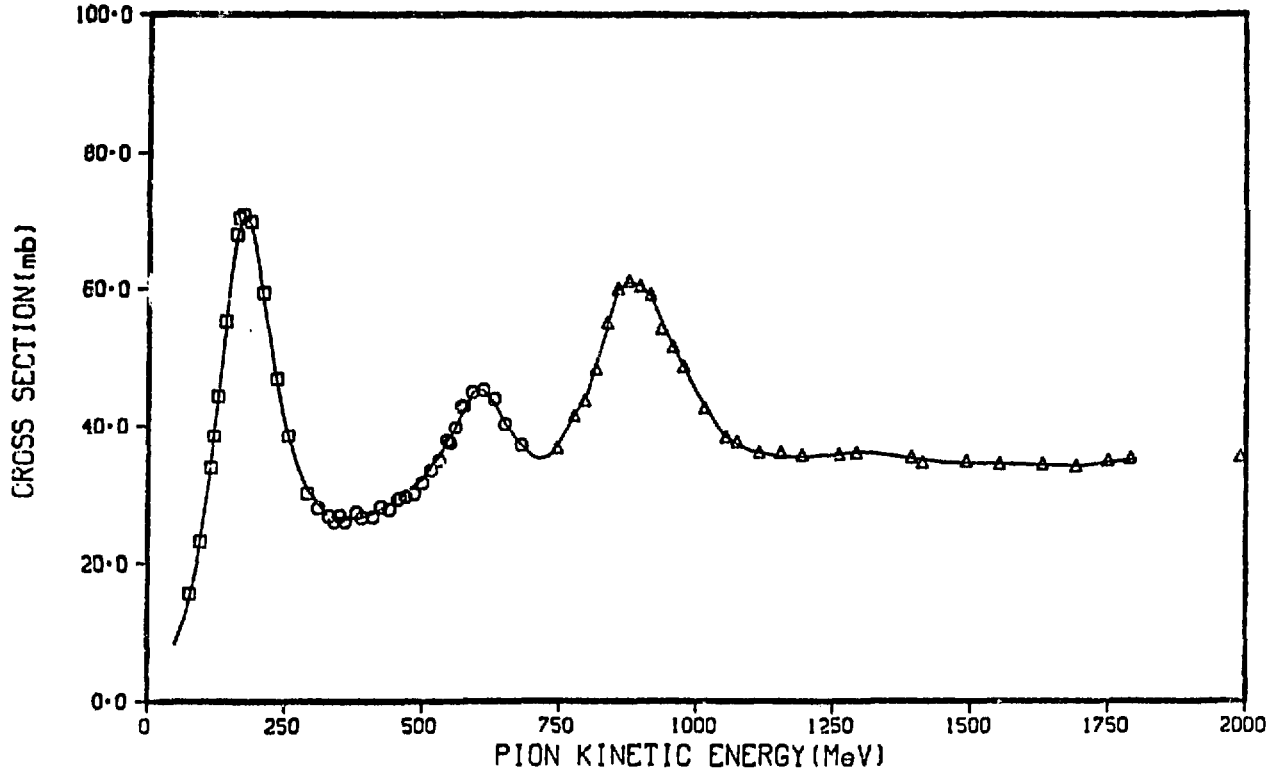

Fig. 1(b). $\pi^- p$ total cross section in the energy region $0 < T_\pi < 2$ GeV[9-11].

Then, for the scattering of positive pions, which involves only the T=3/2 state, the scattering states are: J=1/2, ℓ=0; J=1/2, ℓ=1; and J=3/2, ℓ=1. Hence, the differential cross section for the scattering,

$$\pi^+ + p \longrightarrow \pi^+ + p$$

for the energy region below 300 MeV, may be written as:

$$\frac{d\sigma}{d\Omega} = \lambda\!\!\!^{-2} (A + B \cos\theta + C \cos^2\theta) \ , \qquad (1)$$

where θ is the CM scattering angle and λ is the CM wavelength of the incident pion. For π^+p scattering, the coefficients A, B, and C are functions of the phase shifts δ_3, δ_{31}, and δ_{33}, where the notation for the δ is that of Fermi:

δ_{2T} - S-wave

$\delta_{2T,2J}$ - P-wave

Table I-2 lists the coefficients A, B, and C in terms of these phase shifts[11]. From equation (1), the total cross section is:

$$\sigma_T = 4\pi\lambda\!\!\!^{-2} (A + C/3). \qquad (2)$$

Now, it may be shown (cf, Appendix A) that,

$$3\sigma_T(\pi^-) = \sigma_T(\pi^+) + 2\sigma_T(T=1/2) \ , \qquad (3)$$

where $\sigma_T(\pi^\pm)$ are the total πN cross sections and $\sigma_T(T=1/2)$ is the total cross section for the scattering due to a pure state of isospin 1/2.

TABLE I-2

Representation of A, B, and C in Equation (1) in terms of the phase shifts

$$A = \sin^2\delta_3 + \sin^2(\delta_{33} - \delta_{31})$$

$$B = 2\sin\delta_3\,[2\sin\delta_{33}\cos(\delta_{33} - \delta_3) + \sin\delta_{31}\cos(\delta_{31} - \delta_3)]$$

$$C = 3\sin^2\delta_{33} + 6\sin\delta_{31}\sin\delta_{33}\cos(\delta_{33} - \delta_{31})$$

However, experimental data[8,15] indicate that in the energy region 100 - 300 MeV incident pion energy,

$$\sigma_T(\pi^+) \simeq 3\sigma_T(\pi^-) \ , \tag{4}$$

establishing the fact that there is little contribution from the T=1/2 state to the cross section. Thus, if the peak is due to a resonance in a pure isospin state, it must be in the T=3/2 state. Further analysis of the data indicates that below the peak region, the δ_{33} phase shift is much larger than all other phase shifts. Then, following the argument of de Hoffmann et al.[15], that the phase shifts, which are small and well-behaved in the low energy region, will not suddenly become very large, it would appear that the natural candidate for a resonance is the phase shift δ_{33}. If this is true, then in the resonance region, contributions from all but the δ_{33} phase shift can be ignored in calculating the cross section. In that case, one obtains from equations (1) and (2) and Table I-2,

$$\frac{d\sigma}{d\Omega} = \lambda^2 \sin^2\delta_{33}(1 + 3\cos^2\theta) \ , \tag{5}$$

and,

$$\sigma_T = 8\pi\lambda^2 \sin^2\delta_{33} \ . \tag{6}$$

At the resonance, $\delta_{33} \to 90°$. It is seen from equations (5) and (6) that, if the peak is due to a resonance in the δ_{33} phase shift, then at the resonance, (i) the angular distribution should be symmetrical about θ=90°, and (ii) the total cross section should approach the

unitary value,

$$[\sigma_T]_R = 8\pi\lambda^2 \quad . \tag{7}$$

Both these effects have been observed experimentally[12], thus establishing that the peak at 175 MeV in the $\pi^+ p$ total cross section is due to the p-wave resonance in the J=T=3/2 channel. On similar grounds, the $\pi^- p$ peak at 175 MeV has also been identified as a resonance in the same channel. These peaks are, therefore, referred to as the (3,3) p-wave resonance. Figures 2(a) and 2(b) display the variation of $\pi^{\pm} p$ total cross section in the (3,3) resonance region, obtained by phase shift analysis[16] of the data of Carter et al.[9]

In Appendix A, it is shown that the cross section for πN elastic scattering and charge exchange processes can be expressed in terms of the scattering amplitude $A(\frac{1}{2})$ and $A(\frac{3}{2})$ corresponding to the isospin eigenstates T=1/2 and T=3/2, respectively. In view of the dominance of the T=3/2 state in the (3,3) resonance, contributions from the T=1/2 can be neglected in calculating the cross section at the resonance. By setting $A(\frac{1}{2})=0$ in equations (A.3) to (A.8) of Appendix A, one obtains,

$$\sigma_p^+ \equiv \sigma(\pi^+ + p \to \pi^+ + p) \propto \left|A(\tfrac{3}{2})\right|^2$$

$$\sigma_p^- \equiv \sigma(\pi^- + p \to \pi^- + p) \propto \tfrac{1}{9}\left|A(\tfrac{3}{2})\right|^2$$

$$\sigma_p^0 \equiv \sigma\ \pi^- + p \to \pi^0 + n) \propto \tfrac{2}{9}\left|A(\tfrac{3}{2})\right|^2 \quad .$$

Thus at the (3,3) resonance,

$$\sigma_p^+ : \sigma_p^- : \sigma_p^0 = 9 : 1 : 2 \ , \tag{8}$$

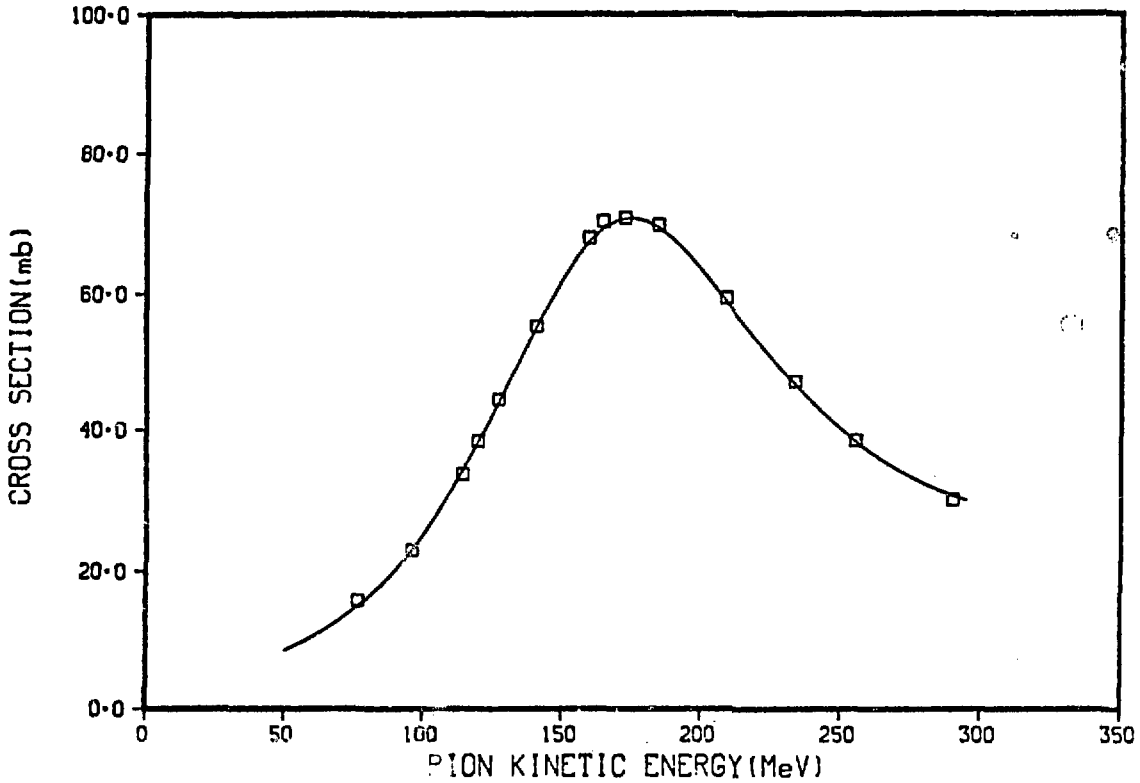

Fig. 2(a). $\pi^- p$ total cross section in the (3,3) resonance region. Data are from Carter et al.[9] and the curve is a fit to the data[16].

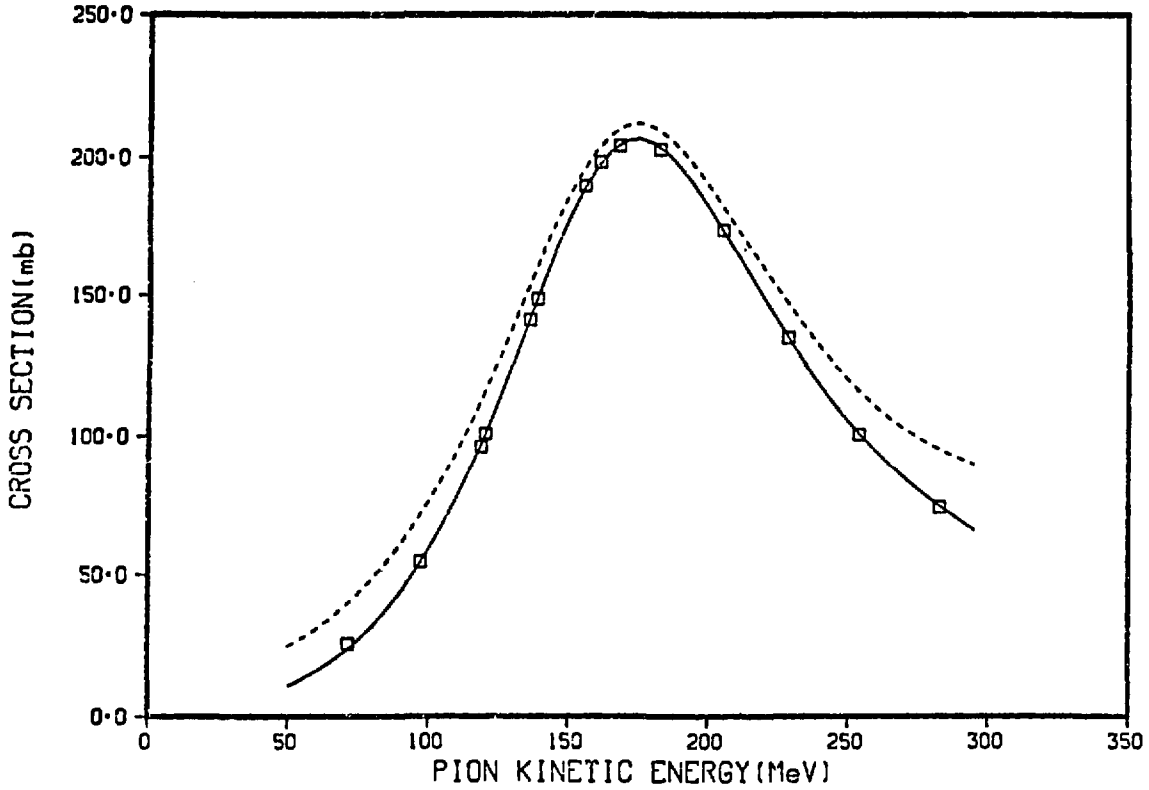

Fig. 2(b). π^+p total cross section in the (3,3) resonance region. Data are from Carter et al.[9] and the solid curve is a fit to the data[16]. The dashed-curve represents $3x\pi^-p$ total cross section, indicating that $\sigma(\pi^+p) \approx 3\sigma(\pi^-p)$ [see text].

and, in a similar way, for $\pi^{\pm}$n scattering,

$$\sigma_n^+ : \sigma_n^- : \sigma_n^0 = 1 : 9 : 2 . \qquad (9)$$

As will be seen later, these results provide a crucial check on theoretical models for pion interactions in which the elementary pion nucleon interaction is very important.

THE PION NUCLEUS SYSTEM

The features special to πN scattering have some interesting consequences in pion nucleus interactions. For example, these interactions often show energy variations which reflect the πN resonances. Figure 3 displays recent experimental data[17] on the total cross section for the scattering of pions by light nuclei. It indicates the profound influence of the free particle resonance on the nuclear scattering cross section.

The interaction of the pion with the nucleus is a many body problem that has no exact and at the same time computable solution. This is a situation quite familiar in nucleon physics, where no complete theory of the nucleon-nucleus interaction exists. The theoretical approach in the analysis of many body problems of this kind generally involves some form of the multiple scattering theory[18], in which the nucleus is treated as an aggregate of nucleons and the interaction of the projectile with the nucleus is obtained by combining the interactions of the projectile with individual nucleons. This approach results in expressing the scattering amplitude as an infinite sum of

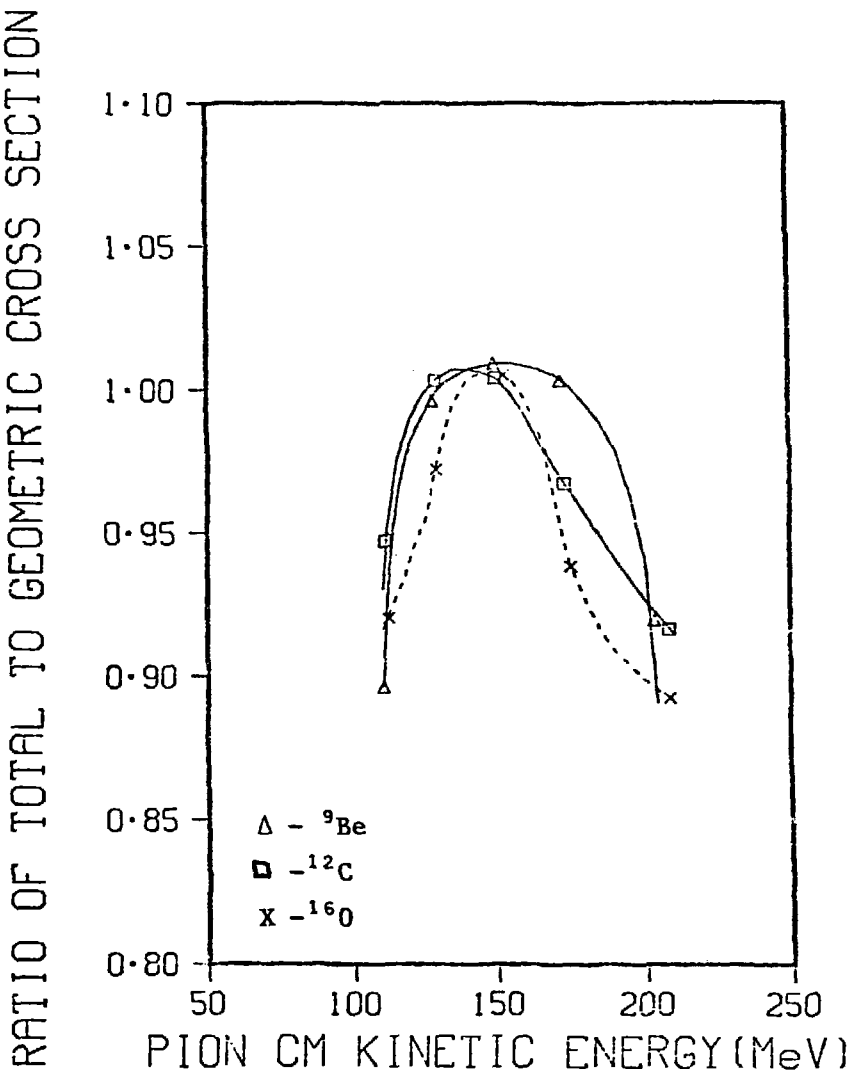

Fig. 3. Total cross section for the scattering of positive pions by light nuclei relative to the unitary limit, $\sigma_T = 2\pi R^2$ (5,17).

individual projectile-nucleon amplitudes, where the first terms corresponds to single scattering, the second to double scattering and so on. In essence, this procedure separates the problem of the elementary projectile nucleon interaction from that of the structure of the nucleus. One then hopes to use the available information on the elementary interaction to gain knowledge on nuclear structure. However, the success of multiple scattering theories depends very much on how fast the scattering series would converge. A crucial parameter in this regard is the ratio of the projectile nucleon scattering amplitude to the average internucleon distance in the nucleus, or roughly equivalently, the product of the amplitude with the nuclear Fermi momentum[3]. At low energies, the pion nucleon scattering amplitude is about 0.1 F, while the nucleon-nucleon amplitude is about two orders of magnitude larger. The average Fermi momentum of a bound nucleon is about 270 MeV/c. Thus the numerical value product $f.p_F$ of the amplitude with the nucleon Fermi momentum for pion scattering is about 0.135, guaranteeing rapid convergence of the multiple scattering series at low energies, where the nucleon-nucleus multiple scattering series poses serious convergence problems. However, near the (3,3) resonance, the pion nucleon amplitude is about 1.0 F and, consequently, the product $f.p_F$ is about ten times larger than at low energies, causing convergence problems in this kinematic region.

A number of other parameters become important in considering the interaction of pions with nuclei. When a pion is absorbed by a nucleus, it brings in to the nucleus a minimum of 140 MeV energy,

which is more than five times the average binding energy of a nuclear nucleon. The mean momentum that would be endowed to a bound nucleon, if a pion were absorbed on it, is roughly given by $\sqrt{2m_\pi m_N} \sim 500$ MeV/c, which is nearly twice as large as the nucleon Fermi momentum p_F. This points to the fact that a single nucleon, by itself, cannot balance momentum and energy in the process of absorbing a pion on it. The preferred mechanism of pion absorption, therefore, involves two nucleons, which split the pion energy between each other and leave the nucleus through the $(\pi,2N)$ reaction.

Near the (3,3) resonance, the momentum of the incident pion is about 300 MeV/c, which is very close to the nucleon Fermi momentum p_F. As a consequence, near or below the resonance, the Fermi averaging of the πN scattering amplitude will significantly change the mean effective amplitude for pion nucleus scattering.

As has been pointed out by Hufner[5], much of the interesting phenomena in pion nucleus interactions occur at energies below 500 MeV. Above this kinematic region, pion nucleus scattering does not differ significantly from the scattering of other strongly interacting particles and, therefore, is not very exciting. Moreover, the energy domain of many of the meson factories is between 0 and 300 MeV; thus many of the discoveries in pion physics in the near future will happen in this energy region.

THESIS PROJECT

This thesis describes a study of the quasielastic pion scattering, performed at the Clinton P. Anderson Meson Physics Facility in

Los Alamos. The study included both theoretical and experimental investigations of the features of $(\pi,\pi N)$ reactions. The background and the motivation for studying these reactions is presented in Chapter II. In Chapter III, a description of a new model for the quasielastic pion scattering is presented together with the predictions of the model. Chapter IV describes the experimental study of the process and the results and conclusions are presented in Chapter V.

CHAPTER II

QUASIELASTIC PION SCATTERING

A. INTRODUCTION

During the past several years, much attention has been given to nuclear processes of the type (x,xN) in which an energetic projectile x scatters off a nucleus quasielastically, causing the removal of a bound nucleon. In particular, it has been possible to evolve a reasonably detailed understanding of the quasielastic or quasifree (p,2p) and (e,e'p) scattering processes in the framework of the impulse approximation[20,21]. However, the analog of these processes for incident pions, the (π,πN) scattering, has remained largely uninvestigated. Even as a mere repetition of the familiar quasielastic processes, the (π,πN) scattering would be of interest, since the pion nucleus interaction is of such a qualitatively different structure compared to the interaction of protons or electrons with the nucleus. Of particular interest would be the effects of the πN resonances on the (π,πN) process. Preliminary studies have indicated that the conditions existing in the process near the (3,3) resonance might be different from those in the quasifree scattering of protons and electrons. A detailed understanding of the process in this important kinematic region of pion nucleon scattering might, therefore, provide insights into the problems involved in the more complex interactions of pions with nuclei.

B. QUALITATIVE ASPECTS OF QUASIELASTIC SCATTERING

When the mean free path of a projectile inside the nucleus becomes of the same order of magnitude as the nuclear radius, it can pass through the nucleus unaffected, or suffering at most only a small number of scatterings. When this happens, the scattering of the projectile from the nucleus can be approximately represented as a sequence of independent collisions of the projectile with individual nucleons. In this 'direct interaction' picture, which was first proposed by Serber[22] to describe the interaction of high energy protons with the nucleus, a quasifree event corresponds to the case in which only one such collision has taken place. If the energy transferred to the nucleon in a quasifree collision is greater than the nucleon removal energy, then the collision can result in the ejection of the nucleon from the nucleus, thus leading to the (x,xN) reaction. Such a reaction is referred to as 'quasielastic scattering', since the process is inelastic in that it causes a rearrangement of the nucleus, but is elastic in the sense that it involves a collision of the projectile with a nucleon inside the nucleus which resembles the scattering of the projectile by free nucleons.

Figure 4 displays one's conception of a quasielastic scattering process in the plane wave impulse approximation (PWIA). Figure 5 is a diagram of the process[23]; here, the initial nucleus is pictured as a bound state (b), consisting of a core (b') and a nucleon (b") weakly bound to the core. The plane wave projectile (a) scatters from the nucleon via a δ-function interaction to give a plane wave scattered projectile (c), and a plane wave ejected nucleon (d).

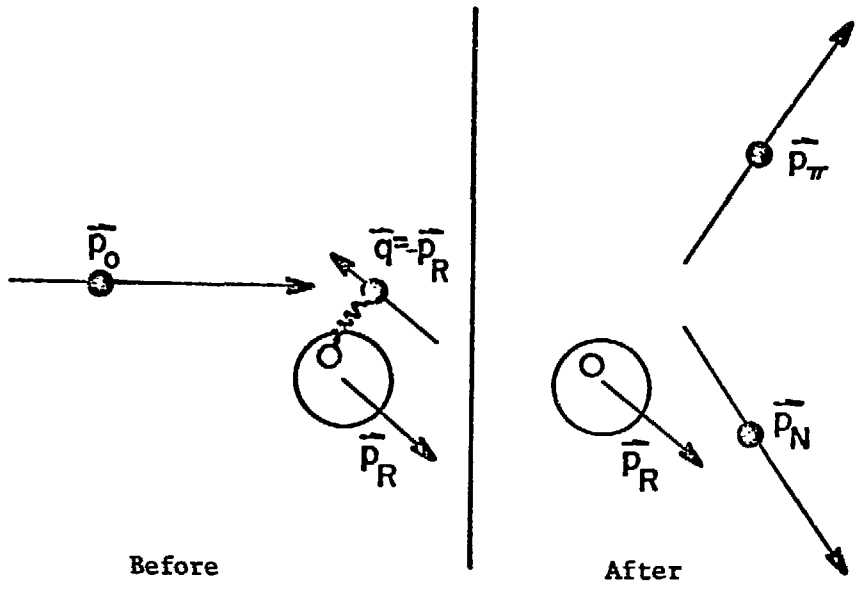

Fig. 4. Quasielastic scattering process in the PWIA.

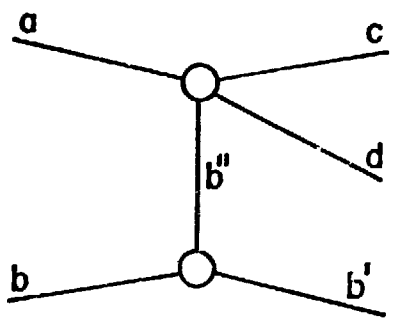

Fig. 5. Diagram of quasielastic scattering.

In the impulse approximation, one further assumes that there are no secondary interactions accompanying the quasielastic process and, therefore, no momentum transfer to the core (b'). Since the original nucleus was at rest, this leads to identifying the final momentum of the core with the negative of the momentum of the struck nucleon, as indicated in Fig. 4. Consequently, the recoil momentum distribution of the residual nucleus in such a picture corresponds to the momentum distribution of the bound nucleons.

The matrix element for the process represented in Fig. 5 is a product of two terms, one arising from each vertex. The lower vertex yeilds a form factor which is the Fourier transform of the wave function for the initial bound state b. The upper vertex yields the free two-body amplitude for the scattering

$$a + b'' \rightarrow c + d$$

One may then show that the differential cross section for the process (x,xN) can be written as[21],

$$\frac{d^3\sigma}{dE_x\, d\Omega_x\, d\Omega_N} = K\, |\phi(\vec{q})|^2\, \left(\frac{d\sigma}{d\Omega}\right)_{xN} \qquad \text{(II.1)}$$

where K is a kinematic function, $\phi(\vec{q})$ is the momentum wave function of the struck nucleon and $\left(\frac{d\sigma}{d\Omega}\right)_{xN}$ is the free xN scattering cross section. Thus, in the plane wave impulse approximation, the (x,xN) reaction cross section is sensitive to the features of the free particle xN cross section.

PWIA calculations have had considerable success in accounting for the features of high-energy (p,2p) and (e,e'p) reactions, indicating that these reactions proceed predominantly by the quasielastic process. On the basis of such a well-characterized reaction mechanism, these reactions have served to explore some of the basic structural features, such as nucleon removal energies and momentum distributions, of complex nuclei.

The basic approach in the study of $(\pi,\pi N)$ scattering does not differ in principle from that used for (p,2p) and (e,e'p) reaction studies[24]. However, it may be pointed out that the validity of the quasielastic description of single-nucleon removal reactions of the form (x,xN) depends very much on the condition that the incoming and the outgoing particles do not suffer inelastic collisions with other nucleons before, during, or after the quasifree collision. If the probability for secondary interactions is large, then the quasifree nature of the process becomes "spoiled" and the quasielastic description becomes less appropriate. An important parameter in this regard is the mean free path λ_x of the projectile x inside the nucleus. Figure 6 displays the variation of the pion mean free path λ_π as a function of incident pion energy in the vicinity of the (3,3) resonance[25]: in contrast with the proton mean free path, which is very small at energies less than 100 MeV, the pion mean free path is a few Fermis even at low energies. However, near the (3,3) resonance, λ_π is about 0.5 F; hence, in this energy region, the pion cannot travel half a Fermi distance inside the nucleus without bumping into a nucleon. The

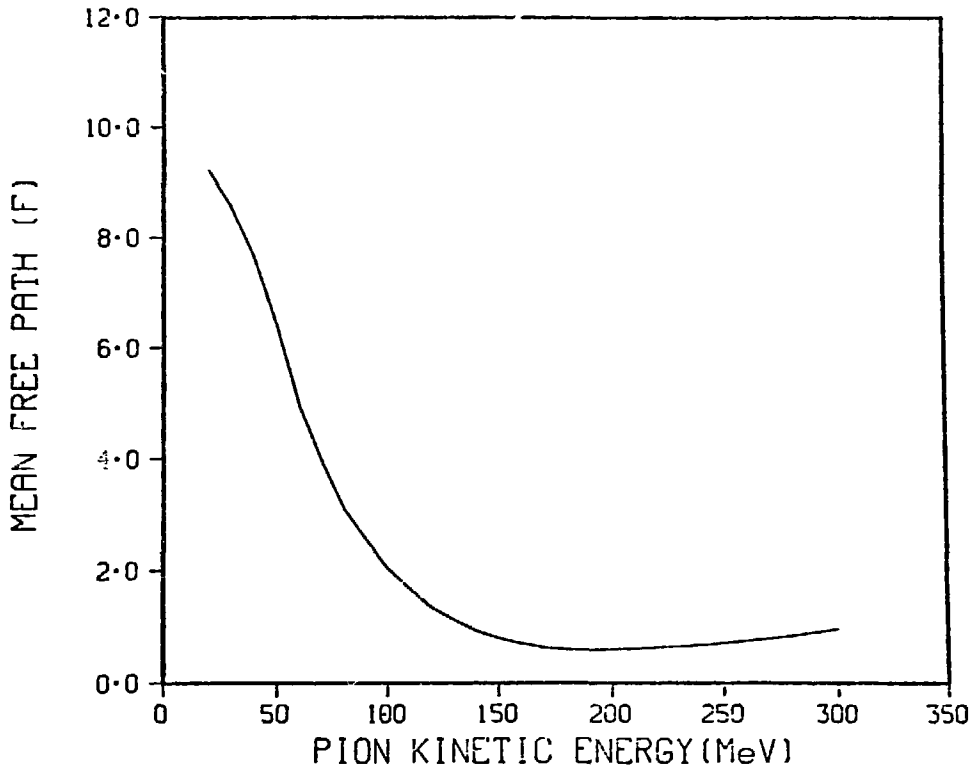

Fig. 6. Variation of the pion mean free path as a function of incident pion energy near the (3,3) resonance region[25].

presence of the (3,3) resonance in the πN cross section, therefore, makes the (π,πN) scattering problem more complex but, at the same time, more interesting and informative.

An important feature of quasielastic scattering is that the kinematics of the process is very nearly the same as that for the free two-body projectile nucleon scattering. Modifications, if any, are those due to the nucleon binding energy and the Fermi momentum of the struck nucleon. If the initial relative energy of the projectile is large compared to the nucleon binding energy, then corrections to the kinematics due to the latter can be neglected. For incident pions of energy T_π, the free particle two-body scattering kinematics is given by,

$$\Delta T_\pi = (q^2/m_N)\ (1 - \cos\theta_{CM}) \qquad \text{(II.2)}$$

where ΔT_π is the energy lost by the incident pion, q and θ_{CM} are the momentum and scattering angle in the pion-nucleon center of mass and m_N is the mass of the nucleon. Hence the kinematic location of quasi-free (π,πN) events is given by,

$$E_{QE} \simeq T_\pi - \Delta T_\pi = T_\pi - (q^2/m_N)\ (1 - \cos\theta_{CM}) \qquad \text{(II.3)}$$

However, the Fermi momentum of the struck nucleon would cause an appreciable broadening of the quasielastic peak. Thus, if one examines the scattering of energetic pions from a medium weight nucleus, in a single counter experiment, the spectrum of scattered pions might look as in Fig. 7[24]; here, A represents the quasielastic peak, the region B contains peaks due to inelastic scattering to particular

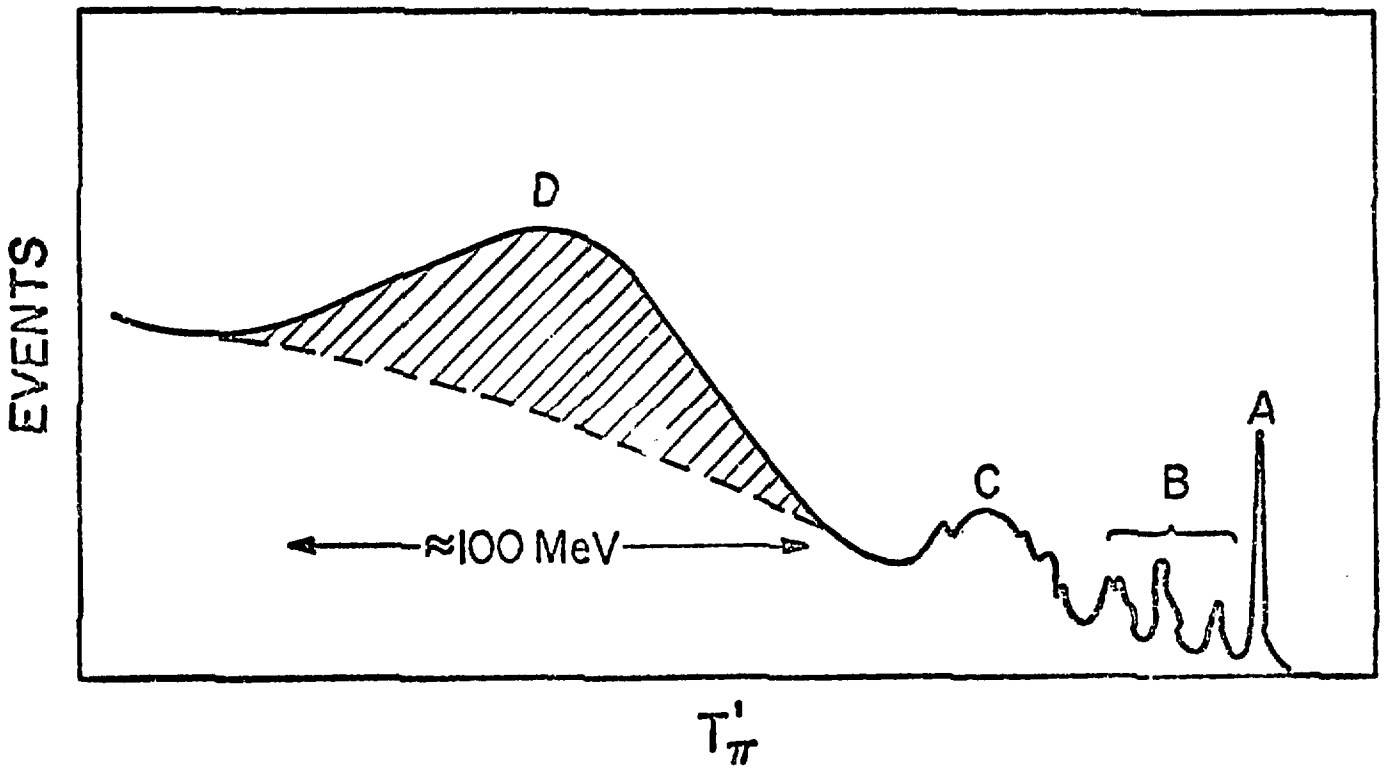

Fig. 7. Spectrum of scattered pions observed in a single counter experiment[24]. A is the elastic peak, B represents peaks due to inelastic scattering, C is the giant resonance and D the quasielastic peak.

excited states and C corresponds to the scattering which excites the broader giant resonance. The quasielastic peak D occurs at an excitation energy which is approximately given by Equation (II.2). Its width is a rough measure of the Fermi momentum of the nucleons. In the figure, it is pictured as sitting on top of a large background arising mainly from multiple scattering processes.

C. GENERAL MOTIVATION FOR $(\pi,\pi N)$ REACTION STUDIES

If the $(\pi,\pi N)$ reaction proceeds predominantly by the quasifree mechanism, then, as in the case of (p,2p) measurements, it should be possible to employ the reaction for determining nucleon removal energies and momentum distributions in nuclei.

Since the quasielastic scattering occurs off the mass shell, the $(\pi,\pi N)$ process might be expected to serve in determining the off-shell pion-nucleon scattering amplitude.

When the $(\pi,\pi N)$ scattering occurs near the (3,3) resonance, the recoil nucleon is in the T=3/2, J=3/2 isobaric state. Thus, the scattering of the isobar from the residual nucleus may provide the opportunity for measuring the scattering length of the Δ_{33} isobar[26].

Obviously, all these prospects are contingent upon the $(\pi,\pi N)$ reaction mechanism being dominated by the quasielastic scattering process. It is, therefore, of interest to determine the exact mechanism of the reaction, before pursuing the above ideas in elaborate experiments.

D. SURVEY OF PREVIOUS $(\pi,\pi N)$ STUDIES

The pioneering effort in the study of $(\pi,\pi N)$ processes was that of Reeder and Markowitz[27], who conducted an investigation of the excitation function for the reaction.

$$^{12}C(\pi^-,\pi^-n)^{11}C \qquad (A)$$

in the energy region 50-400 MeV, employing the activation technique. They scattered a beam of negative pions from a plastic scintillator (CH) target and analyzed the β^+ activity of the residual ^{11}C nucleus in the target. The excitation function so obtained showed a rather wide ($\Gamma\simeq250$ MeV) peak close to the maximum corresponding to the (3,3) resonance in the free particle π^-n scattering. Consequently, it was suggested that the reaction (A) is quasielastic. Later, Poskanzer and Remsberg[28] supplemented the work of Reeder and Markowitz by extending the study of the above reaction to higher energies. They employed the same experimental technique as in the earlier study and found that the energy variation of the excitation function reflected the known higher energy π^-n free particle resonances. They also found that at energies above 0.5 GeV, the ratio of the (π^-,π^-n) to (p,pn) nuclear cross sections was very nearly the same as the ratio of the π^-n to pn free particle cross sections, as expected from the quasifree picture. Similar features were observed by Hower and Kaufman[29] in the $^{40}Ar(\pi^-,\pi^-p)^{39}Cl$ reaction in the energy region 500-1100 MeV. The proton momentum which they obtained from the study of the reaction was in good agreement with that from (p,2p) measurements and this was

ascribed as further evidence for the quasifree nature of the $(\pi,\pi N)$ process. It was also pointed out that the 250 MeV width of the peak in the excitation function for the reaction (A) near the (3,3) resonance favored a quasifree mechanism for the process, since this width corresponded to a value of nearly 180 MeV/c for the average momentum of the struck nucleon, which was consistent with the value 160–170 MeV/c for 1p shell nucleons in light nuclei[27].

Many of the early theoretical efforts in the study of $(\pi,\pi N)$ processes were mainly concerned with reproducing the shape and magnitude of the excitation function for the reaction (A) in the (3,3) resonance region. Reeder and Markowitz[27] attempted a calculation of the reaction in a knock-out model, assuming 'sharp cut-off' nuclear density, and found that, while the general shape of the excitation function could be reproduced, the magnitudes of the calculated cross sections were lower than the observed values by a factor of more than five. Kolybasov[30] carried out a PWIA calculation and obtained qualitative agreement with the absolute value of the cross section except at low energies. Dalkarov[31] modified this calculation by including high order pion rescattering processes. Selleri[32] obtained improved agreement with the experimental data by including momentum-transfer-dependent kinematical factors in the basic knock-out model calculation. Thus, in the early stages of $(\pi,\pi N)$ reaction studies, it appeared as though there were no 'surprises' in the process, the reaction proceeding via the quasielastic knock-out mechanism just as in the familiar (p,2p) and (e,ep) reactions.

In 1969, Chivers et al.[33] conducted a survey of the reactions induced by negative and positive pions in light nuclei near the (3,3) resonance, by employing the radiochemical method of detecting the residual radioactivity. A by-product of this survey was the observation that the ratio of the cross section for the reaction (A) to the summed cross section of the reactions,

$$^{12}C(\pi^+,\pi^+n)^{11}C \qquad (B)$$

and

$$^{12}C(\pi^+,\pi^0p)^{11}C \qquad (C)$$

is equal to 1.0 ± 0.1 at 180 MeV incident pion energy. In the quasi-free picture, the free particle collisions involved in reactions (A), (B), and (C) are:

$$\pi^- + n \rightarrow \pi^- + n$$
$$\pi^+ + n \rightarrow \pi^+ + n$$
$$\pi^+ + n \rightarrow \pi^0 + p,$$

respectively. In Chapter I, it was shown that near the (3,3) resonance, the relative strengths of these processes are in the ratio,

$$\sigma_n^- : \sigma_n^+ : \sigma_n^0 = 9 : 1 : 2.$$

Hence, in the impulse approximation, one had expected,

$$R_n = \frac{\sigma_A}{\sigma_B + \sigma_C} = \frac{\sigma_n^-}{\sigma_n^+ + \sigma_n^0} = 3 \qquad (II.4)$$

Thus, Chiver's result was sharply in conflict with the impulse approximation prediction. This surprising discovery excited considerable interest in the $(\pi,\pi N)$ process. Later investigations have revealed similar discrepancies in a number of other nuclei, ranging from ^{4}He through ^{64}Zn[34-39]. Recently, Dropesky et al.[40] and Batist et al.[41] have independently redetermined the excitation functions for the reactions $^{12}C(\pi^{\pm},\pi n)^{11}C$ over the (3,3) resonance employing again the activation technique. These studies have revealed that the cross section ratios R_n are considerably less than three at every point in this kinematic region. Figure 8 displays the energy dependence of R_n as observed by Batist et al.; it shows that the ratio rises steadily with pion energy from a value of nearly unity at about 50 MeV to about 1.8 at 290 MeV. At 180 MeV, the ratio is about 1.55, which is considerably greater than the value determined by Chivers et al. Figure 8 clearly indicates the fact that the quasifree mechanism cannot account totally for the $(\pi,\pi N)$ reaction mechanism.

Soon after the results of Chivers et al. were published, several mechanisms were proposed to explain the large discrepancy. Many of these proposals considered various final state interactions to be responsible for 'spoiling' the quasifree nature of the reaction. Hewson[42] attempted a theoretical explanation by including an isospin dependent term in the nuclear optical potential which allowed the charge exchange of the outgoing nucleon. Although this calculation did not reproduce Chivers' result of $R_n = 1.0$, Hewson was able to show that by varying the parameters related to the nucleon charge

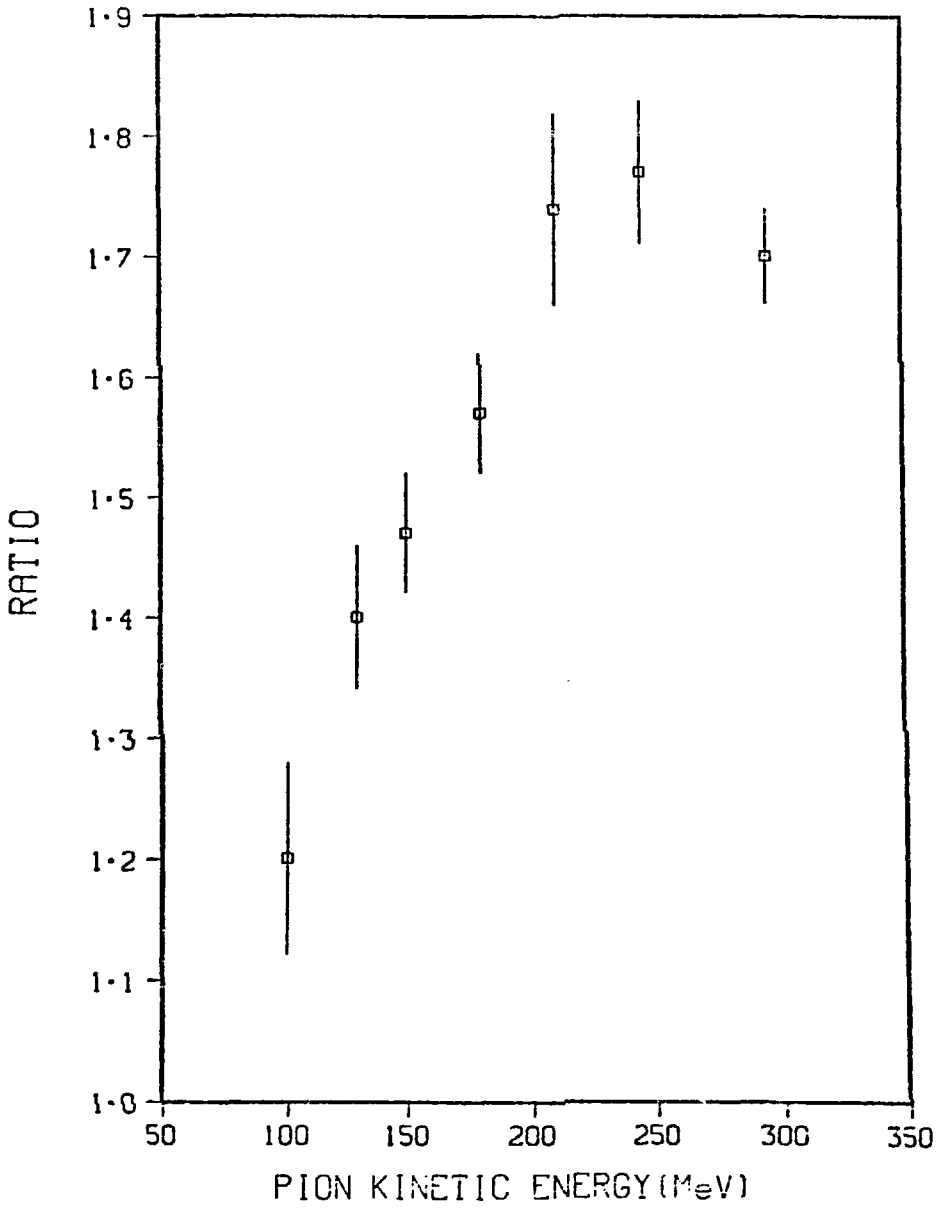

Fig. 8. Energy dependence of the ratio of the cross section for the reaction (A) to the summed cross section of the reactions (B) and (C)[41].

exchange probability, one could obtain a value for R_n anywhere between 1.6 and 1.9 at 180 MeV. Robson[43], employing a PWIA approach, derived an expression for R_n in terms of a parameter χ which described the degree of coherence between residual nuclear states of different isospin. This formulation was successful in explaining Chivers' result; however, its tenet that for a $T_A = 1/2$ nucleus, the cross section ratio should be independent of the parameter χ was shown by Karol et al.[35] to be totally inconsistent with the observed features of the neutron removal reaction on ^{19}F. Wilkinson[44] proposed a mechanism for the $(\pi,\pi N)$ reaction which considered the formation of 'quasi-alpha particles', but as Kolybasov[45] pointed out, the proposal had difficulties in explaining the energy behaviour of the cross section for the reaction (A). Several other mechanisms have been suggested, including the excitation of intermediate states of definite isospin[33,46] and formation of nucleon isobars with particular nuclear interactions, but none of these have in themselves been sufficient to account for all the observed features.

Recently, Sternheim and Silbar[47] proposed an elaboration of the nucleon charge-exchange model due to Hewson[42] in which the variation of R_n with pion energy, as observed by Dropesky et al.[40] was ascribed as due to the energy dependence of the probability for charge exchange of the recoil nucleon as it leaves the nucleus after the quasifree πn collision. Following Sternheim and Silbar, if P is the probability for the recoil nucleon charge exchange, then for neutron knock-out from a nucleus with Z protons and N neutrons, the

inclusion of nucleon charge exchange alters the impulse approximation prediction for R_n as

$$R_n = \frac{\sigma^-}{\sigma^+} = \frac{N\sigma(\pi^-n\to\pi^-n)(1-P) + Z\sigma(\pi^-p\to\pi^-p)P}{N\sigma(\pi^+n\to\pi^+n+\pi^0p)(1-P) + Z\sigma(\pi^+p\to\pi^+p)P} \quad .$$

Hence, employing the results mentioned in Chapter I for the relative strengths of the various free particle πN processes, one obtains for scattering from a Z=N nucleus near the (3,3) resonance,

$$R_n = \frac{9 - 8P}{3 + 6P} \qquad \text{(II.5)}$$

Thus, inclusion of nucleon charge exchange in the (π,πn) process decreases the numerator and increases the denominator. It is seen from (II.5) that when P=0, the ratio is equal to the impulse approximation value of 3. In applying this simple formulation to the case of ^{12}C nucleus, Sternheim and Silbar calculated the probability P in semiclassical transport model, in which the effects of the Pauli exclusion principle were accommodated through normalization to the experimental ratio at 180 MeV. The energy variation of the ratio calculated by them is displayed in Fig. 9 together with the data of Dropesky et al.[40]; the agreement between the model prediction and the experimental ratio is seen to be excellent, at least above about 100 MeV. Subsequently, Jacob and Markowitz[39] found the model to be remarkably successful in predicting the corresponding ratios for ^{14}N, ^{16}O, and ^{19}F. Monahan and Serduke[48] have also reported similar success of the model in accounting for the nucleon removal ratio for

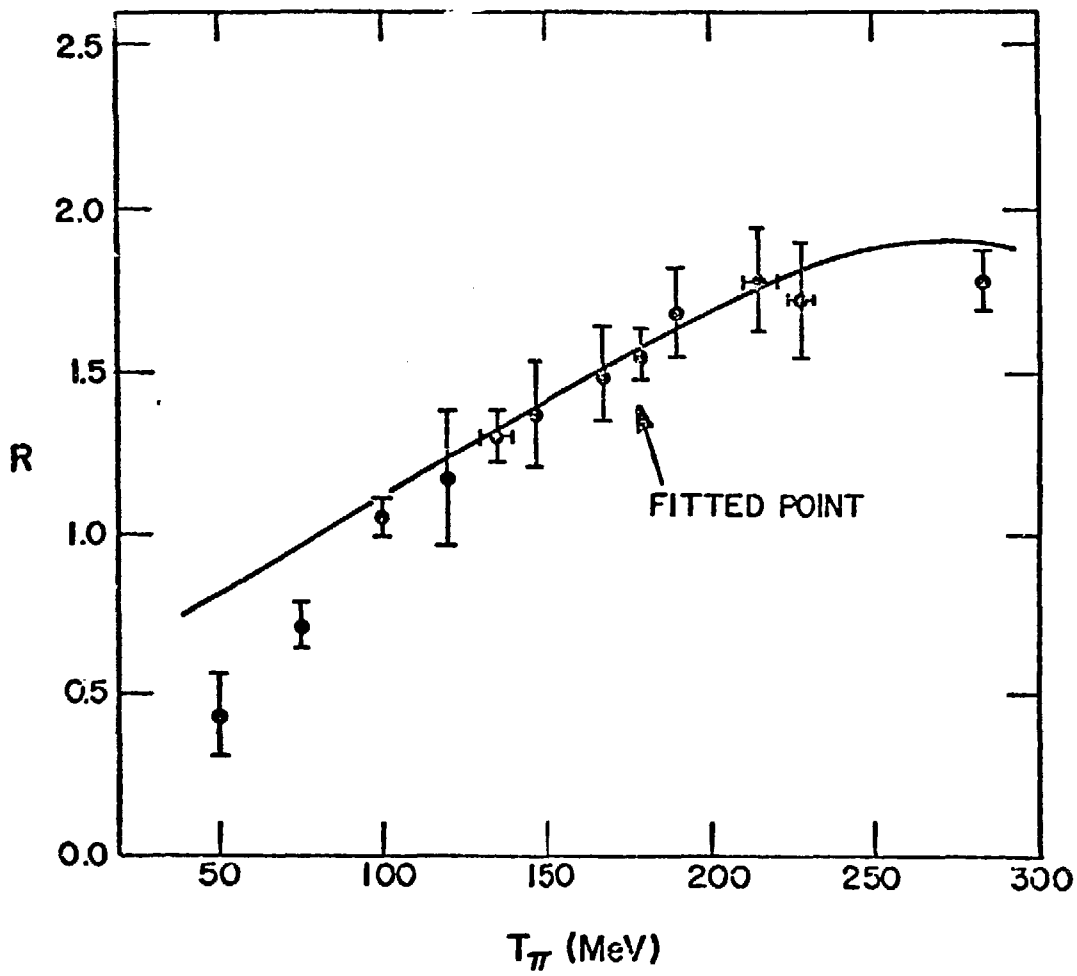

Fig. 9. Energy variation of the ratio R_n calculated by Sternheim and Silbar for ^{12}C[47]. The data shown are those of Dropesky et al.[40].

^{58,60}Ni. Nevertheless, deviations from the simple model have been reported, for example, in neutron removal from ^{64}Zn[49] and in the reaction ^{11}B(π^+,π^0n)^{10}C[50]. These appear to be resolved[51], at least qualitatively, by taking the detailed nuclear structure into account.

E. OBJECTIVES OF THE PRESENT STUDY

The apparent success of the NCE model of Sternheim and Silbar in providing a qualitative interpretation of the observed features of the (π,πN) reaction suggests that the mechanism of the reaction might consist of a combination of knock-out and nucleon charge exchange. It is, however, obvious that this mechanism is far from being completely understood. The situation warrants a more rigorous consideration of the role of the nucleon charge exchange in the reaction mechanism.

Most of the experiments cited in Section D were indirect measurements, involving the observation of β or γ activity of the residual nucleus. Activation measurements of this kind are limited in their scope, since they correspond to cross section measurements for transitions to a particular set of particle-stable nuclear final states only. These measurements do not distinguish between (π^+,π^+n) and (π^+,π^0p) reactions, nor do they determine cross sections to unbound states. Obviously, measurements of this type cannot uniquely identify the mechanism of the (π,πN) reaction. Experiments which completely determine the final state kinematics are required for defining the mechanism of the reaction.

The kinematical variables which enter the reaction (cf. Fig. 5) are the momentum variables $\vec{p}_0$, $\vec{p}_\pi$, $\vec{p}_N$, and $\vec{p}_R$ of the incident pion, the scattered pion, the recoil nucleon and the recoil nucleus, respectively, and their corresponding energies. In the impulse approximation, one identifies the Fermi momentum $\vec{q}$ of the struck nucleon with the negative of $\vec{p}_R$. Then, since the initial nucleus is at rest, conservation of energy and momentum requires that,

$$\vec{p}_0 = \vec{p}_\pi + \vec{p}_N + \vec{p}_R \ ,$$

$$E_0 = E_\pi + E_N + E_R + E_\mu, \qquad \text{(II.6)}$$

where E_μ is the energy missing in the energy balance on account of the nucleon binding energy (E_B) and the excitation energy (E_x) of the residual nucleus. It may be shown that (cf. Appendix B), if $\vec{p}_0$ and E_μ are known and $\vec{p}_N$ (or $\vec{p}_\pi$) and the direction of $\vec{p}_\pi$ (or $\vec{p}_N$) are measured in an experiment, then all the remaining variables can be determined from Equations (II.6). A kinematically complete measurement of the $(\pi,\pi N)$ reaction, therefore, requires a two-arm experiment, one for measuring the energy and momentum of one of the outgoing particles and the second for detecting the other outgoing particle.

It has been pointed out that in lieu of a kinematically complete measurement, the gross features of the $(\pi,\pi N)$ process may be investigated by observing either the scattered pion[24], or, in the case of the $(\pi,\pi p)$ reaction, the recoil proton[52], in single counter experiments. Both these methods should be preferable to the activation measurements. Nevertheless, the first method, viz., the observation of the scattered pion, requires that the quasielastic events be

separated from the inelastic and giant resonance peaks (cf. Fig. 7). This restricts the range of the angle of observation to large values. Even then, because of the large distortion effects present, it may not be possible to disentangle the $(\pi,\pi N)$ events from the huge background arising from the pion multiple scattering. On the other hand, observation of the recoil-proton singles spectrum has the advantage that, because of the differing energy dependences of the πN and NN total cross sections, it might be possible to choose a kinematical situation in which the distortion effects are much less than those in the comparable (π,π') case. However, the method might still be suffering from the flaw that the spectra are contaminated by events in which the incident pion was absorbed.

The present study pertains to the $(\pi,\pi p)$ reaction. It was motivated by the desire to provide a valuable starting point for a kinematically complete measurement of the reaction near the (3,3) resonance. The study intended to cover three points of major interest:

(i) Feasibility of doing $(\pi,\pi p)$ coincidence measurements;

(ii) Desirability of studying the reaction by observing the recoil proton spectrum in a single-arm experiment, as suggested by Silbar and Stupin[52]; and

(iii) Relative importance of recoil nucleon charge exchange in the reaction mechanism.

To this end, recoil proton spectra were measured, in singles and coincidence modes, on selected targets with both π^+ and π^- beams. A semiclassical transport model which incorporated the hypothesis of

recoil nucleon charge exchange was developed to determine the effects of recoil nucleon charge exchange on the reaction mechanism. Details of these investigations are presented in the following chapters.

CHAPTER III

THEORETICAL CONSIDERATIONS

A. INTRODUCTION

A feature of the quasielastic $(\pi,\pi N)$ scattering process is that it involves contributions from many final nuclear states. A semi-classical approach which assumes incoherence is, therefore, likely to be valid in the description of the process. Such an approach postulates that, (i) the reaction takes place inside the nucleus as a one-step process and (ii) the incoming pion and the outgoing pion and nucleon suffer attenuations due to interactions with nuclear matter. The first of these postulates allows one to write the probability for the reaction to be proportional to the free πN collision cross sections, while the second one involves the solution of coupled differential equations which determine the transport of the pion and the nucleon fluxes through nuclear matter.

The model presented here envisages two experimental situations, namely, one in which the recoil nucleon alone is observed, in a single counter experiment, and the other in which both the scattered pion and the ejected nucleon are observed in coincidence. Consequently, the model is formulated in two parts. The first part considers the former situation and predictions are given for observing recoil protons from the $(\pi,\pi p)$ reaction on selected targets for both π^+ and π^-

incident beams. The second part provides an extension of the above formulation to the case of a coincidence measurement.

Silbar and Stupin[52] have reported a similar formalism for observing the $(\pi,\pi p)$ reaction by detecting the recoil proton singles spectrum. The present model differs from this earlier formulation in that the present on assumes a finite probability for the final-state charge exchange of the recoil nucleon. Thus, in the present formulation, the transport equations for the recoil nucleons contain additional terms involving the mean free paths for nucleon charge exchange. For this reason, the present model will hereafter be referred to as the nucleon charge exchange model. Its format is, in many ways, similar to the one used by Sternheim and Silbar[53] in considering pion production from nuclei by proton scattering.

For the purposes of clarity and compactness, only the basic ideas of the model are discussed here; details are given in Appendices C and D.

B. FORMULATION FOR SINGLE-ARM MEASUREMENT

The geometry of the semiclassical charge exchange model for the observation of recoil nucleons is shown in Fig. 10. The incident pion of laboratory energy T_π travels a straight-line distance d_π in nuclear matter to the point $\vec{r}$ (b,z,ϕ), where the quasifree πN collision takes place. As a result of the interaction, the nucleon leaves the nucleus at a laboratory angle π_N with kinetic energy T_N, after traversing a straight-line distance d_N in nuclear matter. The scattered pion also presumably leaves the nucleus at the same time, but its energy

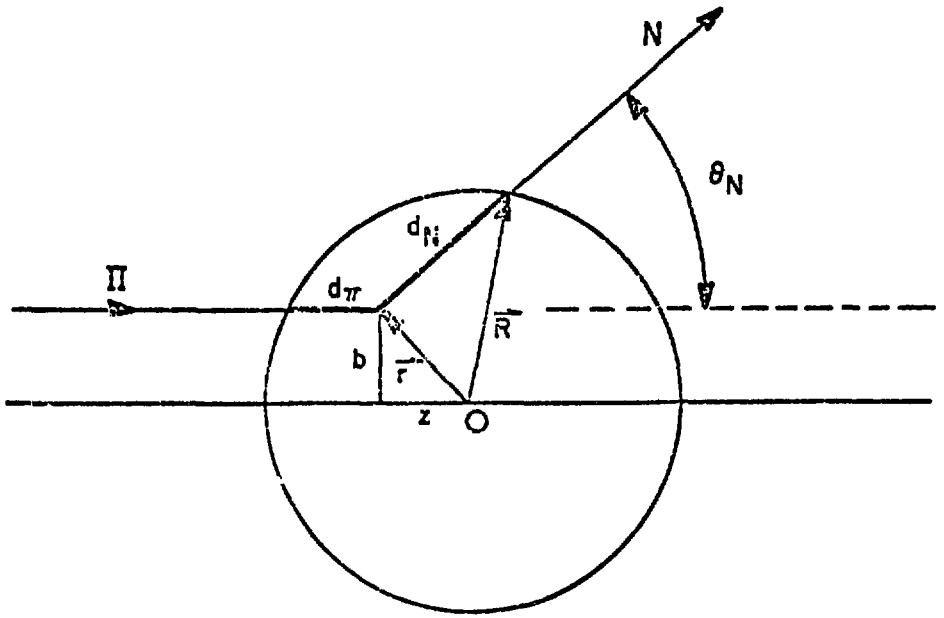

Fig. 10. Geometry of the semiclassical model for the observation of recoil nucleons in a single-arm measurement.

and direction are not observed in the experiment. In this picture, the differential cross section for the $(\pi,\pi N)$ reaction is a sum of terms:

$$\frac{d^2\sigma^{(j,k)}_{QE}}{dp_N\, d\Omega_N} = \Sigma \int d\vec{r}\ \rho(\vec{r})\ \frac{d^2\bar{\sigma}^{(j,k)}_{free}}{dp_k\, d\Omega_k}\ D_i(\vec{r}) \ . \qquad \text{(III.1)}$$

Here, the indices j and k denote the charge states of the incident pion and the <u>detected</u> nucleon respectively:

$$j = 1 \longrightarrow \pi^+$$

$$j = 2 \longrightarrow \pi^- ;$$

$$k = 1 \longrightarrow p$$

$$k = 2 \longrightarrow n \ . \qquad \text{(III.2)}$$

The summation in Equation (III.1) is over all possible reaction mechanisms which leave the detected nucleon in the charge state k and the integration is over the volume of the nucleus.

Each of the terms on the right-hand side of Equation (III.1) involves two factors. The first,

$$\bar{\sigma}^{(j,k)} \equiv \rho(\vec{r})\ \frac{d^2\bar{\sigma}^{(j,k)}_{free}}{dp_k\, d\Omega_k} \ , \qquad \text{(III.3)}$$

which is the product of the nuclear density and the relevent πN differential cross section averaged over the Fermi momentum of the struck nucleon, represents the probability for the $(\pi,\pi N)$ reaction to occur at the point $\vec{r}$ inside the nucleus. In the present formulation, $\rho(\vec{r})$ is

assumed to be of the non-uniform Woods-Saxon form, normalized to unity:

$$\rho(\vec{r}) = \rho_o / \left[1 + \exp\left(\frac{r - r_o}{a}\right)\right] ,$$

$$\int d\vec{r}\ \rho(\vec{r}) = 1 . \qquad \text{(III.4)}$$

The second factor, $D_i(\vec{r})$ accounts for the attenuations of the incident pion and the outgoing nucleon fluxes as well as the nucleon charge exchange. This factor is calculated in the next section.

C. THE ATTENUATION FACTOR $D_i(\vec{r})$

(1) Pion Flux Attenuation

The attenuation of the incident pion flux is mainly due to the πN scattering and the pion absorption processes. The mean free paths for these are:

$$\lambda_{\pi N}(T_\pi) = A\ \rho(\vec{r})\ \bar{\sigma}_{\pi N}(T_\pi) ,$$

$$\lambda_{\pi,abs}(T_\pi) = A\ \rho(\vec{r})\ \sigma_{\pi,abs}(T_\pi) , \qquad \text{(III.5)}$$

respectively. Here,

$$\bar{\sigma}_{\pi N} \equiv (Z\ \sigma_{\pi p} + N\ \sigma_{\pi n})/A \qquad \text{(III.6)}$$

is the total πN cross section per nucleon averaged over protons and neutrons, and $\sigma_{\pi,abs}$ is the total cross section per nucleon for pion

absorption. The number of pions arriving at the interaction point $\vec{r}$ is proportional to

$$P_\pi(\vec{r}) = \exp\left[-d_\pi \left(\lambda_{\pi N}^{-1} + \lambda_{\pi,abs}^{-1}\right)\right], \qquad \text{(III.7)}$$

where d_π is the path length shown in Fig. 10. Since the inverse mean free paths in the above equation depend on the nonuniform nuclear density [cf. Equation (III.5)], they are functions of $\vec{r}$. To avoid calculational difficulties, this density dependence is avoided in the present model by writing the mean free paths in terms of the central density ρ_0 and replacing the geometric path length d_π in the above equation by the effective path-length $\bar{d}_\pi$, defined as,

$$\bar{d}_\pi = \rho_0^{-1} \int_{-\infty}^{0} \rho(\vec{r} + \hat{k}s)\, ds \ , \qquad \text{(III.8)}$$

where $\hat{k}$ is a unit vector along the pion beam direction. However, since the pion absorption is presumed to be mainly a two-nucleon process, the effective path length for this process is defined in terms of the square of the density:

$$\bar{a}_\pi \equiv \bar{d}_{\pi,abs} = \rho_0^{-2} \int_{-\infty}^{0} \rho^2(\vec{r} + \hat{k}s)\, ds \ . \qquad \text{(III.9)}$$

Under these transformations, Equation (III.7) becomes,

$$P_\pi(\vec{r}) = \exp\left[-\bar{d}_\pi/\bar{\lambda}_{\pi N} - \bar{a}_\pi/\bar{\lambda}_{\pi,abs} \right] \qquad \text{(III.10)}$$

where the $\bar{\lambda}$'s are now constant parameters and are given by,

$$\bar{\lambda}_{\pi N}(T_\pi) = [A\ \rho_0\ \bar{\sigma}_{\pi N}(T_\pi)]^{-1}$$

$$\bar{\lambda}_{\pi,abs}(T_\pi) = [A\ \rho_0\ \bar{\sigma}_{\pi,abs}(T_\pi)]^{-1} \quad . \qquad \text{(III.11)}$$

(2) Attenuation and Charge Exchange of Recoil Nucleons

The attenuation of the recoil-nucleon flux is largely due to absorption in nuclear matter. Assuming that the total cross section for nucleon absorption, $\sigma_{N,abs}$ is the same for both protons and neutrons, the inverse mean free path for this process can be written as

$$\lambda_{abs}^{-1} \equiv \rho\lambda_a^{-1} = A\rho\,\sigma_{N,abs} \qquad \text{(III.12,a)}$$

The relative populations of the outgoing protons and neutrons are affected, in addition, by charge-exchange reactions. The inverse mean free paths for the charge-exchange processes pn → np and np → pn can be written in terms of the nucleon charge exchange cross section, $\sigma_{N,ex}$ as:

$$\lambda_{x,p}^{-1} \equiv \rho\lambda_p^{-1} = Z\ \rho\sigma_{N,ex}\ ,$$

$$\lambda_{x,n}^{-1} \equiv \rho\lambda_n^{-1} = N\ \rho\sigma_{N,ex}\ . \qquad \text{(III.12,b)}$$

Let $N_1(0)$ and $N_2(0)$ be respectively the number of protons and neutrons ejected from the point r by the $(\pi,\pi N)$ interaction. Then, at a distance x from r, their populations $N_1(s)$ and $N_2(s)$ are

determined by the coupled first order differential equations,

$$N_1' = -\lambda_{abs}^{-1} N_1 - \lambda_{x,n}^{-1} N_1 + \lambda_{x,p}^{-1} N_2$$

$$N_2' = -\lambda_{abs}^{-1} N_2 - \lambda_{x,p}^{-1} N_2 + \lambda_{x,n}^{-1} N_1 \qquad \text{(III.13)}$$

Introducing the matrix B, given by

$$B = \begin{pmatrix} -(\lambda_a^{-1} + \lambda_n^{-1}) & \lambda_p^{-1} \\ \lambda_n^{-1} & -(\lambda_a^{-1} + \lambda_p^{-1}) \end{pmatrix} \qquad \text{(III.14)}$$

the transport Equations (III.13) can be written in the matrix form,

$$\begin{pmatrix} N_1' \\ N_2' \end{pmatrix} = \rho B \begin{pmatrix} N_1 \\ N_2 \end{pmatrix} \qquad \text{(III.15)}$$

The solution of this equation obtained by standard methods (cf. Appendix C) is,

$$N_i(x) = \sum_j M_{ij}(x)\, N_j(o);\ i, j=1,2\ . \qquad \text{(III.16)}$$

Then, far outside the nucleus, the populations of recoil protons and neutrons are given by

$$N_i(\infty) = \sum_j M_{ij}(\infty)\, N_j(o);\ i, j=1,2\ . \qquad \text{(III.17)}$$

In Equations (III.16) and (III.17), the M_{ij}'s are functions of the mean free path parameters, λ_a, λ_p, and λ_n and the effective nucleon path length R(r) given by

$$R(\vec{r}) = \frac{1}{\rho_o} \int_o^\infty \rho(\vec{r} + \hat{k}' s)\, ds \qquad \text{(III.18)}$$

where $\hat{k}'$ is a unit vector in the nucleon direction and the integral is from the interaction point $\vec{r}$ to ∞. They represent the probability of detecting the outgoing nucleon in the charge state j, when the struck nucleon is in the charge state i. To understand this point, consider that the struck nucleon at $\vec{r}$ is a proton. Then

$$N_1(o) = 1$$

$$N_2(o) = 0 \quad .$$

From Equation (17), then, for every proton ejected from $\vec{r}$, one observes N_1 protons and N_2 neutrons in the detector, given by

$$N_1(\infty) = M_{11}(\infty)$$

$$N_2(\infty) = M_{21}(\infty)$$

Thus M_{11} and M_{21} are the probabilities for detecting a proton or a neutron when the struck nucleon at r is a proton. In a similar way, it can be shown that M_{22} and M_{12} are the probabilities for observing a neutron or a proton as the outgoing particle, when the struck at r is a neutron. These observations are summarized in Table III-1, together with the representations of the M_{ij}'s in terms of the relevant cross sections.

TABLE III-1

Representation of the matrix elements M_{ij} in terms of σ's.

Struck Nucleon	Detected Nucleon	Matrix Element	Representation
p	p	M_{11}	$\frac{e^{-\alpha R}}{A}(Z + N\, e^{-\beta R})$
p	n	M_{21}	$\frac{e^{-\alpha R}}{A}(N - N\, e^{-\beta R})$
n	n	M_{22}	$\frac{e^{-\alpha R}}{A}(N + Z\, e^{-\beta R})$
n	p	M_{12}	$\frac{e^{-\alpha R}}{A}(Z - Z\, e^{-\beta R})$

$\alpha = A\, \sigma_{N,abs}$

$\beta = A\, \sigma_{N,ex}$

The above considerations permit one to write the factor $D_i^{(j,k)}(\vec{r})$

$$D_i^{(j,k)} = P_\pi(\vec{r})\ M_{ki}(\vec{r}) \qquad \text{(III.19)}$$

Hence, the differential cross section, Equation (III.1) can be written as

$$\frac{d^2\sigma_{QE}^{(j,k)}}{dp_N\ d\Omega_N} = \sum_i N_i \frac{d^2\bar{\sigma}_{free}^{(j,i)}}{dp_N\ d\Omega_N} \int d\vec{r}\rho(\vec{r})\ P_\pi(\vec{r})\ M_{ki}(\vec{r}) \qquad \text{(III.20)}$$

This general equation gives the differential cross section for observing a nucleon in the charge state k by scattering a pion in the charge state j. The summation is over all the different processes which result in the detection of the nucleon in the charge state k.

D. EXPECTATION FOR QUASIELASTIC (π,p) SCATTERING

The spectrum of recoil protons from the quasielastic scattering of positive pions, when observed in a single counter, would involve contributions from the following three processes:

(1) $\pi^+ p \rightarrow \pi^+ p$

(2) $\pi^+ n \rightarrow \pi^o p$

(3) $\pi^+ n \rightarrow \pi^+ n \xrightarrow{CEX} \pi^+ p$

Process (3) involves the charge exchange of the recoil neutron. From Table III.1, the matrix elements M_{ij} corresponding to these processes

are M_{11}, M_{11}, and M_{12}, respectively. Writing

$$Q = \int dr\ \rho(\vec{r})\ P_{\pi}(\vec{r})\ M_{11}(\vec{r}) ,$$

$$P = \int dr\ \rho(\vec{r})\ P_{\pi}(r)\ M_{12}(\vec{r}) , \qquad \text{(III.21)}$$

one obtains from Equation (III.20), the differential cross section for the quasielastic (π,p) scattering,

$$\sigma^{(\pi^+,p)} \equiv \frac{d^2\sigma^{(\pi^+,p)}_{QE}}{dP_p\ d\Omega_p} = Z\ \bar{\sigma}_1^{+}\ Q^{+} + N\ \bar{\sigma}_2\ Q^{+} + N\ \bar{\sigma}_3\ P^{+} , \qquad \text{(III.22)}$$

where the superscript + on Q and P denotes that the probability $P_{\pi}(\vec{r})$ in Equations (III.21) are calculated for incident π^+ beam. The spectrum factors $\bar{\sigma}_1^{+}$, $\bar{\sigma}_2^{+}$, and $\bar{\sigma}_3^{+}$ are the Fermi-averaged free π^+N cross sections for processes (1), (2), and (3), respectively; they are functions of the kinematical variables T, P_p and θ_p.

The differential cross section for quasielastic (π^-,p) scattering, which involves the processes:

$$\pi^- p \rightarrow \pi^- p ,$$

$$\pi^- p \rightarrow \pi^o n \xrightarrow{CEX} \pi^o p ,$$

$$\pi^- n \rightarrow \pi^- n \xrightarrow{CEX} \pi^- p ,$$

is obtained, in a similar way, as

$$\sigma^{(\pi^-,p)} \quad \frac{d^2\sigma^{(\pi^-,p)}_{QE}}{dP_p\ d\Omega_p} = Z\ \bar{\sigma}_1^{-}\ Q^{-} + Z\ \bar{\sigma}_2^{-}\ P^{-} + N\ \bar{\sigma}_3^{-}\ P^{-} , \quad \text{(III.23)}$$

where Q^- and P^- correspond to π^- beam and $\bar{\sigma}_1^-$, $\bar{\sigma}_2^-$, and $\bar{\sigma}_3^-$ are the Fermi-averaged π-N cross sections for the above three processes. For the non-charge-exchange limit, which corresponds to P=0, one obtains,

$$R_{3,3}^{Z=N} = 11 \ .$$

In Equations (III.22) and (III.23), the spectrum factors $\bar{\sigma}_2^+$, which represent the smearing due to the Fermi motion of the nucleon, are, unfortunately, ambiguous quantities[54]. However, near the (3,3) resonance, they tend to follow the free πN cross section ratios presented in Chapter I. (cf. Equations (1.8) and (1.9). Thus, in the resonance region,

$$\sigma_{3,3}^{(\pi^+,p)} \simeq \frac{1}{9}\,\bar{\sigma}\,(3,3)\,[(9Z + 2N)Q^+ + NP^+]$$

$$\sigma_{3,3}^{(\pi^-,p)} \simeq \frac{1}{9}\,\bar{\sigma}\,(3,3)\,[ZQ^- + (9N + 2Z)P^-] \qquad \text{(III.24)}$$

The ambiguities in the $\bar{\sigma}$'s can be avoided if one forms the ratio

$$R_{3,3} = \frac{\sigma_{3,3}^{(\pi^+,p)}}{\sigma_{3,3}^{(\pi^-,p)}} = \frac{(9Z + 2N)Q^+ + NP^+}{ZQ^- + (9N + 2Z)P^-} \ . \qquad \text{(III.25)}$$

One observes that, in this equation, the coefficient of the charge exchange probability term P^- for incident π^- beam is large compared to that of the direct term Q^-; it is also larger than the coefficient beam.

For a Z=N nucleus, such as ^{12}C, the terms $P^{\pm}$ and $Q^{\pm}$ are such that

$$P^{+} = P^{-} = P \ ,$$
$$Q^{+} = Q^{-} = Q \ ; \qquad \text{(III.26)}$$

Equation (III.25) then reduces to

$$R_{3,3}^{Z=N} = \frac{11Q + P}{Q + 11P} \ . \qquad \text{(III.27)}$$

E. CALCULATION OF P AND Q

The factors P and Q, as defined in Equation (III.21), involve three-dimensional integrations over the volume of the nucleus, the integration variables being b, z and ϕ. To perform these calculations, a computer code QUASEX[55] was developed. This program, written in Fortran IV, runs on the CDC 6600 or CDC 7600 computer at the Central Computing Facility of the Los Alamos Scientific Laboratory. A listing of the program is given in Appendix E.

The input parameters to the program are listed in Table III.2. In order to calculate the average πN total cross section defined in Equation (III.b), one needs to know both πp and πn cross sections; however, in the present calculation, assuming charge symmetry, the cross sections $\sigma_{\pi^{\pm}n}$ were replaced by $\sigma_{\pi^{\pm}p}$, i.e.,

$$\bar{\sigma}_{\pi^{+}p} = (Z\sigma_{\pi^{+}p} + N\sigma_{\pi^{-}p})/A$$

$$\bar{\sigma}_{\pi^{-}p} = (Z\sigma_{\pi^{-}p} + N\sigma_{\pi^{+}p})/A$$

TABLE III-2

Input parameters to QUASE X program

Card#	Variable(s)	Details
1	TPI	- Incident pion KE (MeV-lab).
	SIGPIP, SIGPIM	- $\pi^+\rho$ and $\pi^-\rho$ total cross sections (mb) at TPI.
2	THETA, THPI	- θ_ρ, θ_π in degress.
3	ANUM, ZNUM	- A- and Z- numbers of target nucleus.
	XI, RHLF, THK	- Nuclear density parameters
4	NBPTS, NZPTS, NPHI, NSPTS	- Mesh size for integration.
5	NEWLIM	- Number of proton momentum data points.
6 to NEWLIM+5	PPR	- Proton momemtum (MeV/c).
	SIGPP, SIGPN	- $\rho\rho$ and ρn cross sections (mb).
	TPISC	- Scattered pion KE(MeV)
	SPIPL, SPIMI	- $\pi^+\rho$ and $\pi^-\rho$ total cross sections (mb) at TPISC

The pion absorption cross section $\sigma_{\pi,abs}$ is a poorly known parameter. Estimates[24] have shown that this cross section is in the range 20–40 mb. Consequently, P's and Q's were calculated for $\sigma_{\pi,abs}$ = 10, 20, 30 and 40 mb. However, it was found that the P's and Q's are not very sensitive to this cross section in the range 10–40 mb.

Another parameter which is not very well known is the nucleon charge-exchange cross section $\sigma_{N,ex}$. Therefore, this cross section was taken from the estimate by Sternheim and Silbar[47] who parameterized it as

$$\sigma_{N,ex} = \beta T_N^{-1.9}$$

Here T_N is the recoil nucleon energy and β is a parameter which was obtained by a fitting procedure described in Ref. (47).

In the present calculations, a range of values for the momentum of the outgoing protons were considered. This is because, the $(\pi^{\pm},p)$ quasielastic experiment in which only the outgoing proton is observed is not a kinematically complete experiment. The Fermi motion of the struck proton inside the nucleus allows a wide range of energy with which the observed proton can leave the nucleus at a given angle θ_p.

Tables III.3(a) - 3(h) present the values of $P^{\pm}$ and $Q^{\pm}$ and of the corresponding ratios of π^+ to π^- cross sections for ^{12}C, ^{27}Al, ^{63}Cu and ^{208}Pb targets for θ_p = 55° and 64° when the incident pion energy is 255 MeV. The ratios are plotted in Figs. 11 and 12. The values quoted here were calculated with $\sigma_{N,abs}$ = 0; thus, they

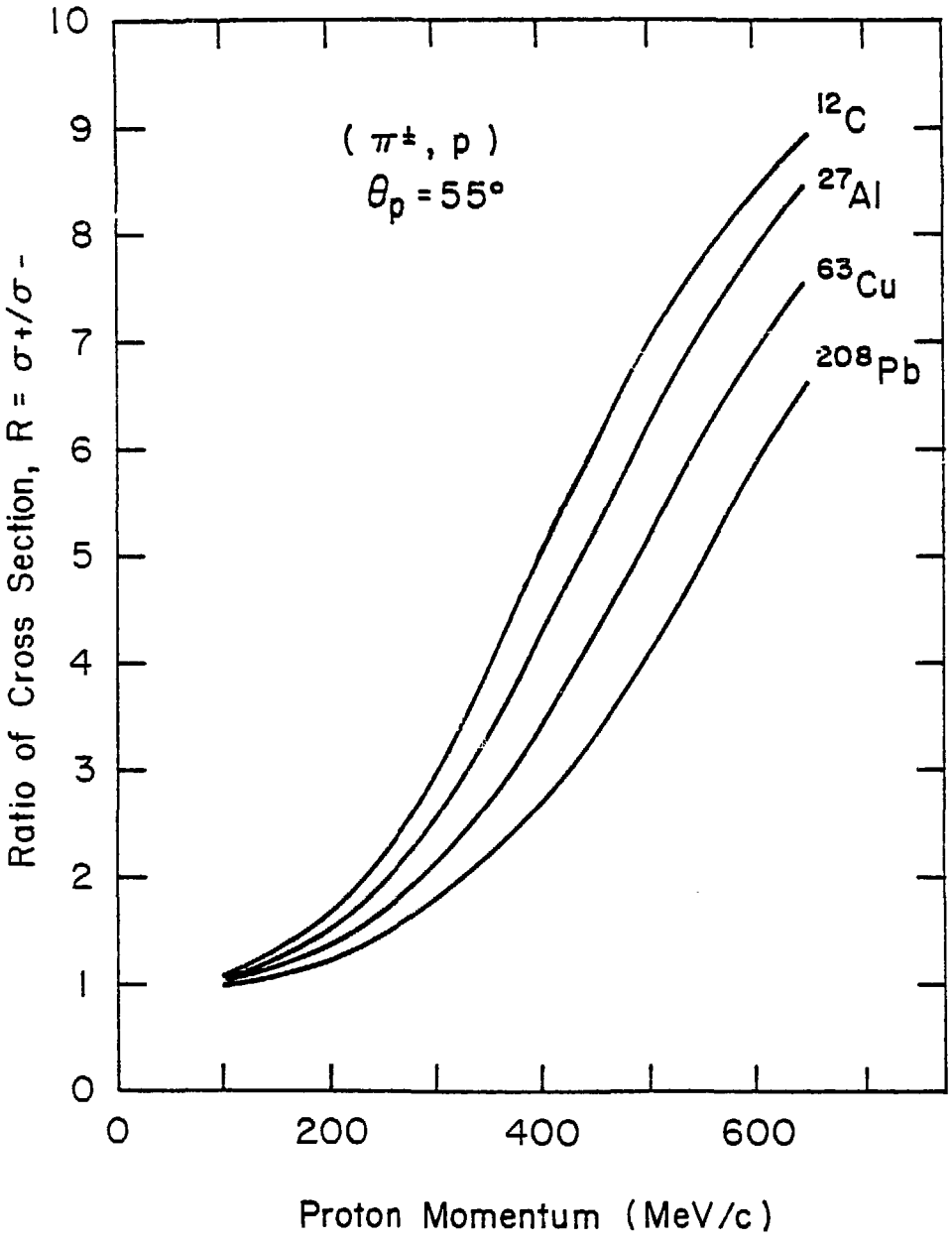

Fig. 11. Predicted ratios of π^+ to π^- cross sections as functions of detected proton momentum for $\theta_p = 55°$ in a single-arm measurement.

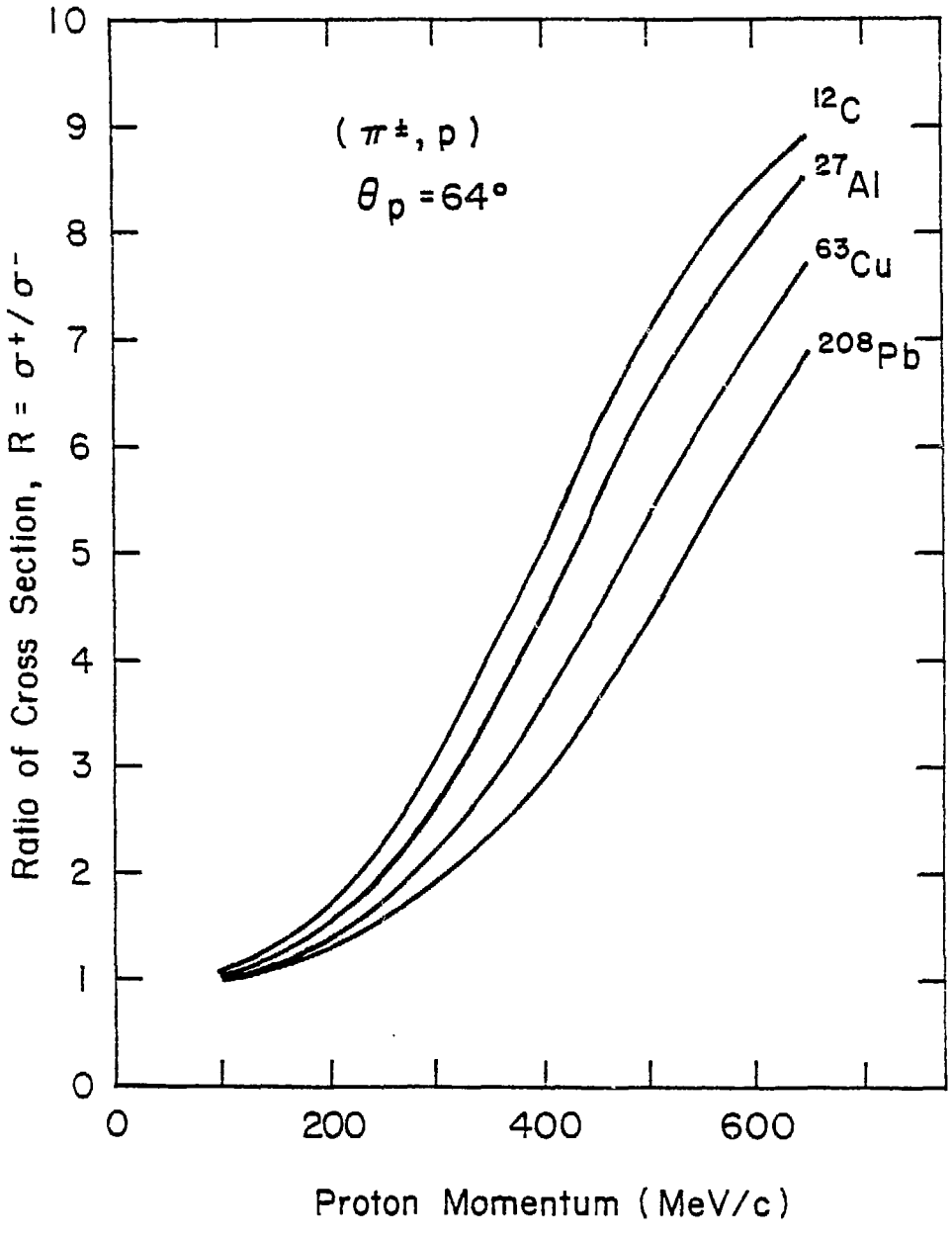

Fig. 12. Predicted ratios of π^+ to π^- cross sections as functions of detected proton momentum for $\theta_p = 64°$ in a single-arm measurement.

TABLE III-3(a)

P's and Q's and the corresponding ratio of π^+ to π^- cross section for the (π,p) measurement on ^{12}C for $T_\pi \approx 255$ MeV, for $\theta_p = 55°$. $\sigma_{N,abs} = 0.$

P_p(MeV/c)	Q^+	P^+	Q^-	P^-	Ratio
100.0	0.2269	0.2066	0.2269	0.2066	1.081
150.0	0.2493	0.1843	0.2493	0.1843	1.285
200.0	0.2792	0.1544	0.2792	0.1544	1.631
250.0	0.3121	0.1214	0.3121	0.1214	2.158
300.0	0.3439	0.0896	0.3439	0.0896	2.914
350.0	0.3703	0.0633	0.3703	0.0633	3.880
400.0	0.3894	0.0441	0.3894	0.0441	4.947
450.0	0.4024	0.0311	0.4024	0.0311	5.988
500.0	0.4112	0.0223	0.4112	0.0223	6.921
550.0	0.4171	0.0164	0.4171	0.0164	7.706
600.0	0.4212	0.0123	0.4212	0.0123	8.344
650.0	0.4241	0.0095	0.4241	0.0095	8.851

TABLE III-3(b)

P's and Q's and the corresponding ratio of π^+ to π^- cross section for the (π,p) measurement on ^{27}Al for T_π = 255 MeV, for θ_p = 55°. $\sigma_{N,abs}$ = 0.

P_p (MeV/c)	Q^+	P^+	Q^-	Q^-	Ratio
100.0	0.1742	0.1610	0.1713	0.1582	1.047
150.0	0.1900	0.1463	0.1870	0.1436	1.220
200.0	0.2115	0.1263	0.2082	0.1239	1.506
250.0	0.2355	0.1041	0.2319	0.1020	1.923
300.0	0.2597	0.0815	0.2556	0.0799	2.509
350.0	0.2819	0.0609	0.2773	0.0597	3.291
400.0	0.2998	0.0443	0.2948	0.0435	4.224
450.0	0.3129	0.0321	0.3077	0.0315	5.214
500.0	0.3222	0.0235	0.3168	0.0231	6.171
550.0	0.3287	0.0175	0.3132	0.0172	7.036
600.0	0.3333	0.0133	0.3276	0.0130	7.779
650.0	0.3365	0.0102	0.3308	0.0100	8.398

TABLE III-3(c)

P's and Q's and the corresponding ratio of π^+ to π^- cross section for the (π,p) measurement on ^{63}Cu for T_π = 255 MeV, for θ_p = 55°. $\sigma_{N,abs}$ = 0.

P_p(MeV/c)	Q^+	P^+	Q^-	P^-	Ratio
100.0	0.1198	0.1090	0.1115	0.1045	1.015
150.0	0.1253	0.1012	0.1205	0.0968	1.153
200.0	0.1381	0.0902	0.1329	0.0862	1.377
250.0	0.1526	0.0779	0.1469	0.0743	1.688
300.0	0.1675	0.0651	0.1612	0.0621	2.103
350.0	0.1824	0.0524	0.1755	0.0499	2.657
400.0	0.1962	0.0407	0.1885	0.0388	3.368
450.0	0.2076	0.0310	0.1994	0.0295	4.199
500.0	0.2164	0.0235	0.2078	0.0223	5.086
550.0	0.2229	0.0179	0.2140	0.0170	5.964
600.0	0.2278	0.0138	0.2186	0.0131	6.785
650.0	0.2313	0.0108	0.2220	0.0102	7.521

TABLE III-3(d)

P's and Q's and the corresponding ratio of π^+ to π^- cross section for the (π,p) measurement on ^{208}Pb for T_π = 255 MeV, for θ_p = 55°.

$\sigma_{N,abs}$ = 0.

P_p (MeV/c)	Q^+	P^+	Q^-	P^-	Ratio
100.0	0.0630	0.0597	0.0559	0.0527	0.957
150.0	0.0678	0.0566	0.6604	0.0497	1.069
200.0	0.0748	0.0521	0.0669	0.0455	1.248
250.0	0.0828	0.0468	0.0741	0.0408	1.488
300.0	0.0912	0.0414	0.0816	0.0360	1.789
350.0	0.0998	0.0358	0.0891	0.0311	2.169
400.0	0.1086	0.0301	0.0968	0.0261	2.666
450.0	0.1172	0.0245	0.1042	0.0212	3.297
500.0	0.1247	0.0196	0.1108	0.0170	4.048
550.0	0.1310	0.0155	0.1162	0.0135	4.876
600.0	0.1359	0.0123	0.1205	0.0107	5.736
650.0	0.1397	0.0098	0.1238	0.0085	6.584

TABLE III-3(e)

P's and Q's and the corresponding ratio of π^+ to π^- cross section for the (π,p) measurement on ^{12}C for T_π = 255 MeV, for θ_p = 64°.

$\sigma_{N,abs}$ = 0.

P_p (MeV/c)	Q^+	P^+	Q^-	P^-	Ratio
100.0	0.2273	0.2062	0.2273	0.2062	1.085
150.0	0.2505	0.1830	0.2505	0.1830	1.299
200.0	0.2814	0.1521	0.2814	0.1521	1.661
250.0	0.3147	0.1188	0.3147	0.1188	2.208
300.0	0.3464	0.0872	0.3464	0.0872	2.986
350.0	0.3722	0.0614	0.3722	0.0614	3.968
400.0	0.3908	0.0427	0.3908	0.0427	5.042
450.0	0.4034	0.0301	0.4034	0.0301	6.085
500.0	0.4119	0.0216	0.4119	0.0216	7.011
550.0	0.4177	0.0159	0.4177	0.0159	7.787
600.0	0.4216	0.0119	0.4216	0.0119	8.414
650.0	0.4244	0.0091	0.4244	0.0091	8.911

TABLE III-3(f)

P's and Q's and the corresponding ratio of π^+ to π^- cross section for the (π,p) measurement on $^{27}A\ell$ for T_π = 255 MeV, for θ_p - 64°.

P_p(MeV/c)	Q^+	P^+	Q^-	P^-	Ratio
100.0	0.1746	0.1606	0.1717	0.1578	1.051
150.0	0.1911	0.1452	0.1881	0.1426	1.234
200.0	0.2136	0.1244	0.2103	0.1220	1.538
250.0	0.2382	0.1016	0.2345	0.0995	1.979
300.0	0.2625	0.0790	0.2583	0.0774	2.591
350.0	0.2842	0.0587	0.2797	0.0575	3.396
400.0	0.3016	0.0426	0.2967	0.0418	4.345
450.0	0.3143	0.0309	0.3091	0.0302	5.343
500.0	0.3232	0.0226	0.3178	0.0221	6.300
550.0	0.3295	0.0168	0.3239	0.0164	7.157
600.0	0.3339	0.0127	0.3282	0.0124	7.889
650.0	0.3370	0.0098	0.3313	0.0096	8.497

TABLE III-3(g)

P's and Q's and the corresponding ratio of π^+ to π^- cross section for the (π,p) measurement on ^{63}Cu for T = 255 MeV, for $\theta_p = 64°$.

$\sigma_{N,abs} = 0.$

P_p(MeV/c)	Q^+	P^+	Q^-	P^-	Ratio
100.0	0.1164	0.1088	0.1118	0.1043	1.019
150.0	0.1262	0.1004	0.1214	0.0960	1.168
200.0	0.1398	0.0888	0.1346	0.0848	1.410
250.0	0.1549	0.0759	0.1492	0.0723	1.748
300.0	0.1703	0.0628	0.1639	0.0598	2.194
350.0	0.1851	0.0501	0.1781	0.0477	2.781
400.0	0.1985	0.0387	0.1908	0.0368	3.520
450.0	0.2095	0.0293	0.2013	0.0279	4.372
500.0	0.2179	0.0222	0.2093	0.0211	5.270
550.0	0.2241	0.0169	0.2152	0.0160	6.151
600.0	0.2287	0.0130	0.2195	0.0124	6.967
650.0	0.2320	0.0101	0.2227	0.0096	7.692

TABLE III-3(h)

P's and Q's and the corresponding ratio of π^+ to π^- cross section for the (π,p) measurement on ^{208}Pb for T_π = 255 MeV, for θ_p = 64°.

$\sigma_{N,abs}$ = 0.

P_p (MeV/c)	Q^+	P^+	Q^-	P^-	Ratio
100.0	0.0632	0.0596	0.0561	0.0526	0.962
150.0	0.0685	0.0561	0.0611	0.0493	1.086
200.0	0.0761	0.0512	0.0681	0.0447	1.286
250.0	0.0848	0.0456	0.0760	0.0396	1.555
300.0	0.0936	0.0398	0.0839	0.0345	1.892
350.0	0.1025	0.0341	0.0916	0.0295	2.312
400.0	0.1113	0.0283	0.0992	0.0225	2.849
450.0	0.1195	0.0230	0.1064	0.0198	3.518
500.0	0.1267	0.0183	0.1126	0.0158	4.300
550.0	0.1326	0.0144	0.1177	0.0125	5.151
600.0	0.1372	0.0114	0.1217	0.0099	6.024
650.0	0.1408	0.0091	0.1248	0.0079	6.876

correspond to the case in which the attenuation of the nucleon fluxes due to quasielastic NN scatterings is neglected. The reason for this choice is that, for any given nucleon momentum, NN scatterings cause a loss of nucleon flux to lower energies together with a gain from scatterings of initially higher energy nucleons: To some extent, the loss and the gain balance.[54]

The results presented here indicated a strong dependence of the ratio on the momentum P_p of the observed recoil nucleon.

F. EXTENSION TO $(\pi,\pi p)$ MEASUREMENTS

The geometry of the model for $(\pi,\pi p)$ coincidence measurements is shown in Fig. 13. Here, d_π, is the path-length corresponding to the scattered pion. In the coincidence formulation, the integrals P and Q, defined by Equations (III.21), are modified to include the attenuation of the outgoing pion flux. Thus, P and Q are now defined to be

$$P = \int d\vec{r}\ \rho(\vec{r})\ P_\pi(\vec{r})\ P'_\pi(\vec{r})\ M_{11}(\vec{r})\ ,$$

$$Q = \int d\vec{r}\ \rho(\vec{r})\ P_\pi(\vec{r})\ P'_\pi(\vec{r})\ M_{12}(\vec{r})\ , \qquad \text{(III.28)}$$

where $P'_\pi(\vec{r})$ is the attenuation factor for the scattered pion flux. In the present calculations, $P'_\pi(\vec{r})$ is estimated in a way similar to the calculation of $P_\pi(\vec{r})$ in Section C(a):

$$P'_\pi(\vec{r}) = \exp(-\bar{d}'_\pi/\bar{\lambda}'_{\pi N} - \bar{\alpha}'_\pi/\bar{\lambda}'_{\pi,abs})\ ; \qquad \text{(III.29)}$$

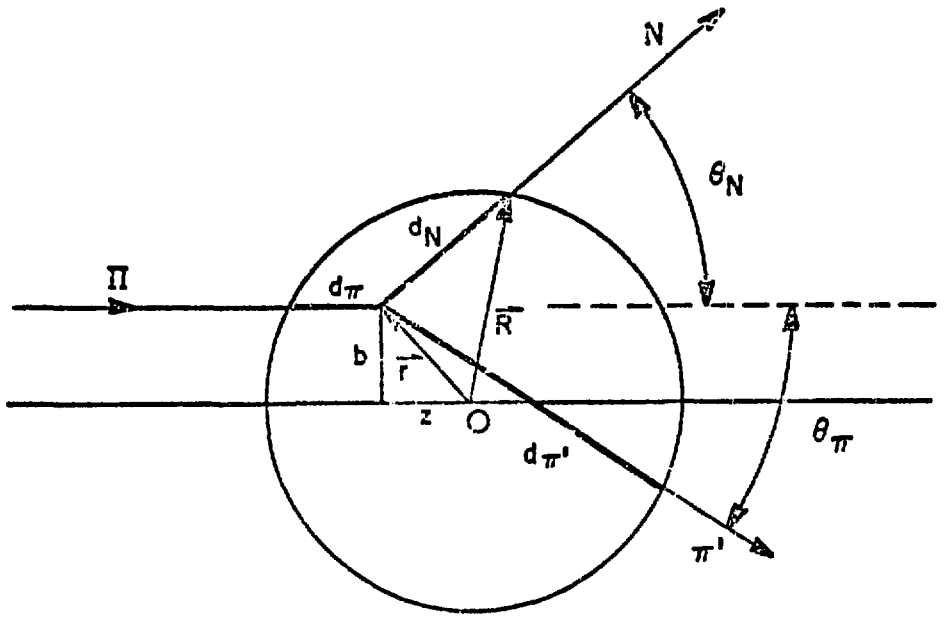

Fig. 13. Geometry of the semiclassical model for (π,πp) coincidence measurements.

here, the parameters in the exponent are defined analogous to those in $P_\pi(\vec{r})$ [cf. Equation (III.10)], but correspond to the scattered pion.

Since the scattered pion is also detected in the measurement, the pion charge exchange processes, $\pi^- p \to \pi^o n$ and $\pi^+ n \to \pi^o p$ do not contribute to the cross sections. Thus, the $(\pi,\pi p)$ cross sections near the (3,3) resonance are given by

$$\sigma_{3,3}^{(\pi^+,\pi^+ p)} \simeq \frac{1}{9}\,\bar{\sigma}(3,3)\;[9ZQ^+ + NP^+]$$

$$\sigma_{3,3}^{(\pi^-,\pi^- p)} \simeq \frac{1}{9}\,\bar{\sigma}(3,3)\;[ZQ^- + 9NP^-] \qquad \text{(III.30)}$$

The π^+ to π^- cross section ratio, near the (3,3) resonance, is

$$R_{3,3} \equiv \frac{\sigma_{3,3}^{(\pi^+,\pi^+ p)}}{\sigma_{3,3}^{(\pi^-,\pi^- p)}} = \frac{9ZQ^+ + NP^+}{ZQ^- + 9NP^-} \qquad \text{(III.31)}$$

For a Z=N nucleus,

$$R_{3,3}^{Z=N} = \frac{9Q + P}{Q + 9P}.$$

This has the non-charge-exchange limit of 9.

The mean free paths $\bar{\lambda}'_{\pi N}$ and $\bar{\lambda}'_{\pi,abs}$ in Equation (III.29) are functions of the scattered pion energy. Consequently, in order to determine these parameters, the energy T'_π of the scattered pion must be determined for a given momentum of the recoil nucleon. The kinematics of quasielastic $(\pi,\pi p)$ scattering is given in Appendix B.

As is established there, to each value of the recoil proton momentum, there are two values of T'_π; however, one of these corresponds to too large a value for the Fermi momentum of the struck nucleon to be acceptable. Once an acceptable value for the energy T'_π is determined, the $T_\pi p$ cross sections can be calculated from their known energy variations[16]. Tables III.4(a) - 4(h) present the values of the scattered pion energy T'_π and the corresponding $\pi^{\pm}p$ cross sections for a range of values of the recoil proton momentum, for 255 MeV incident pions, for $(\theta_p, \theta_\pi) = (55°, 50°)$ and $(64°, 37.5°)$. The $\pi^{\pm}p$ cross sections then determine $\bar{\lambda}'_{\pi N}$ [cf. Equation (III.11)].

As in the case of (π,p) calculations, the values of P and Q were determined for $\sigma_{\pi,abs} = 10$, 20, 30 and 40 mb, for a range of values of recoil proton momentum. Tables III.5(a) - 5(h) present the results for 255 MeV pions, for $(\theta_p, \theta_\pi) = (55°, 50°)$ and $(64°, 37.5°)$, when $\sigma_{\pi,abs} = 20$ mb and $\sigma_{N,abs} = 0$. The resulting π^+ to π^- ratios are plotted in Figs. 14 and 15.

In calculating $(\pi,\pi p)$ cross sections, it may be necessary to include the effect of quasielastic NN scatterings on the nucleon flux attenuation, since the arguments presented earlier in Section E for setting $\sigma_{N,abs} = 0$ in the (π,p) case, may not apply to the present one. Consequently, P's and Q's were also calculated for $\sigma_{N,abs} \neq 0$. These results are presented in Tables III.6(a) - 6(h).

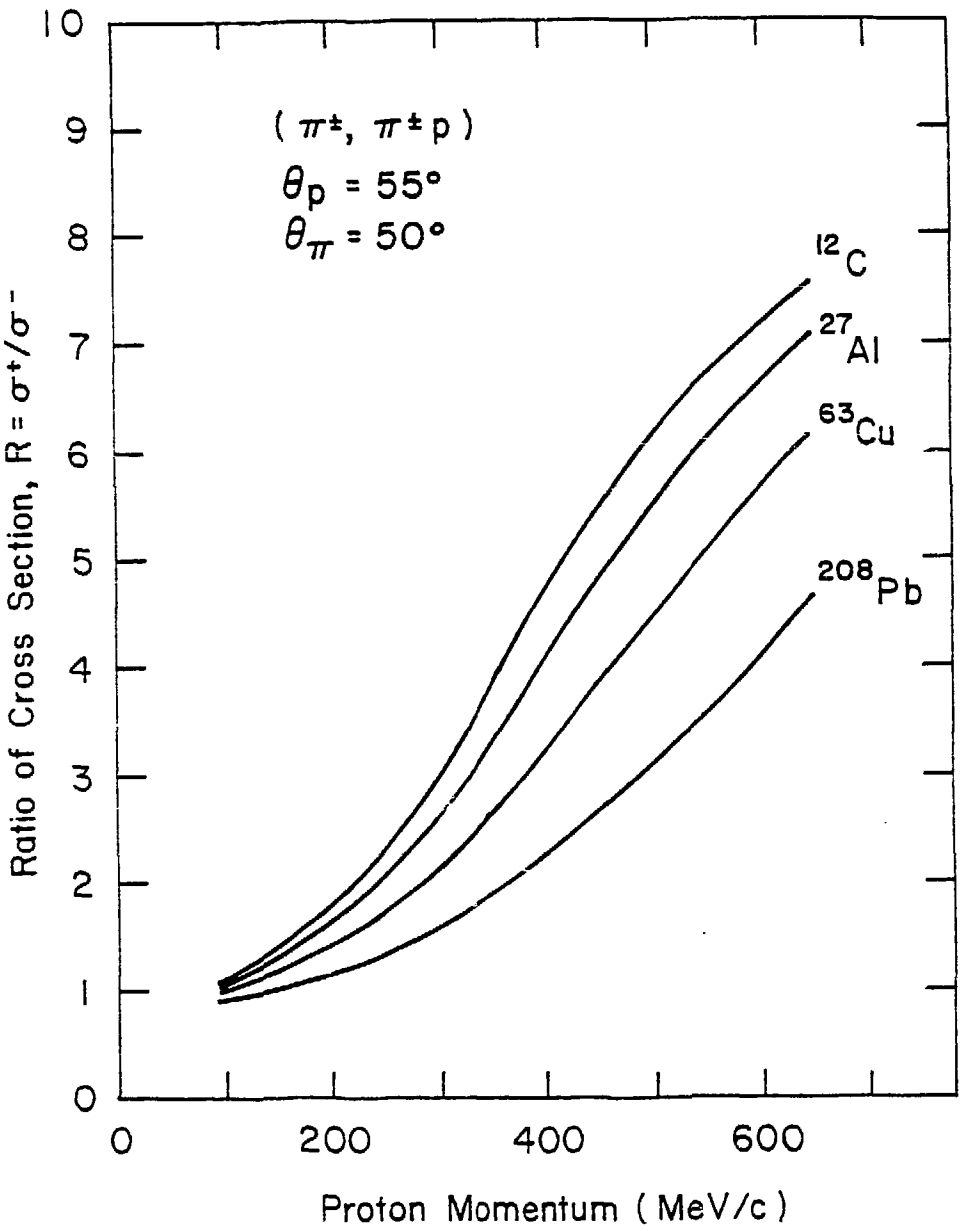

Fig. 14. Predicted ratios of π^+ to π^- cross sections as functions of detected proton momentum for $(\theta_p,\theta_\pi) = (55°,50°)$ in a coincidence measurement.

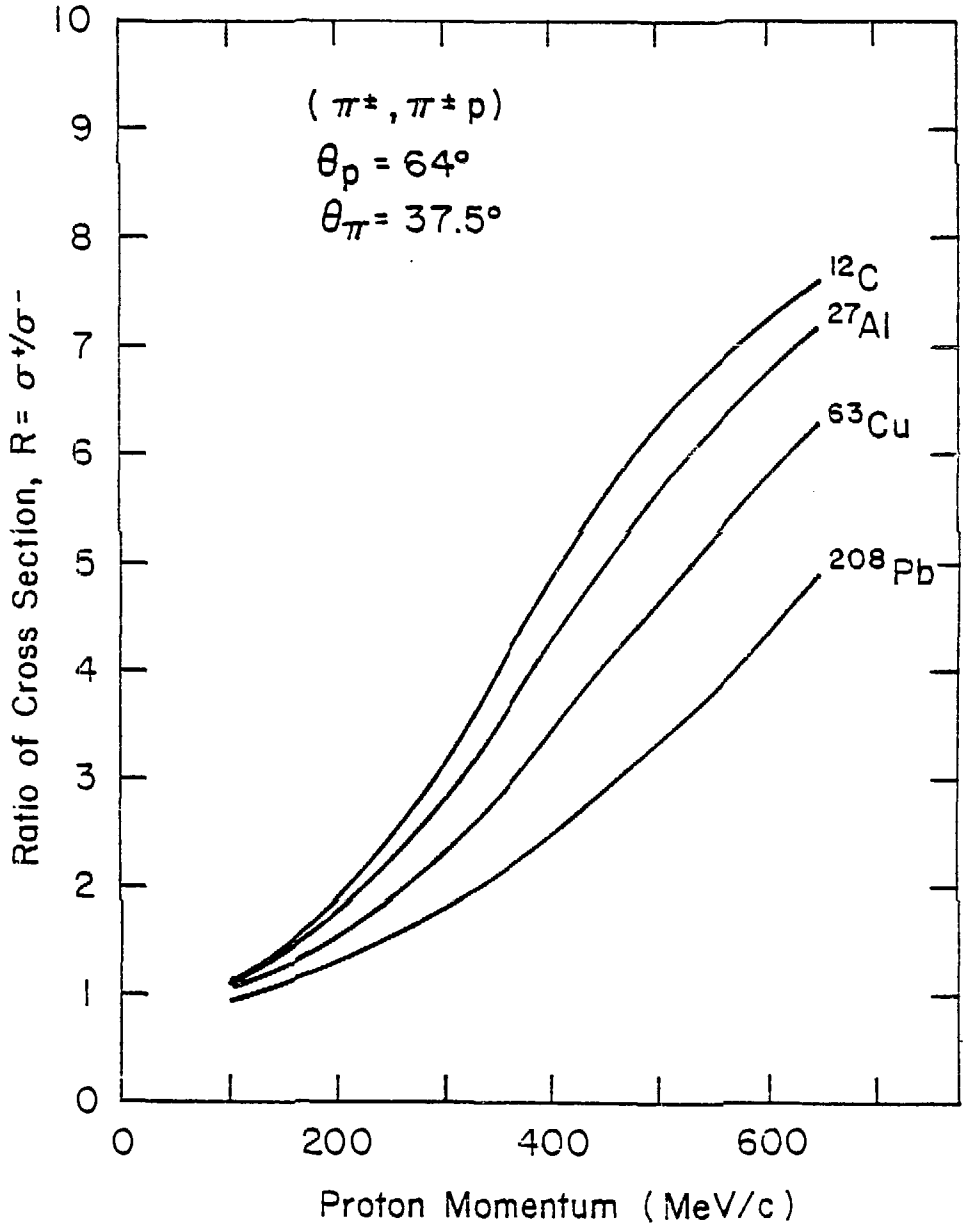

Fig. 15. Predicted ratios of π^+ to π^- cross sections as functions of detected proton momentum for $(\theta_p,\theta_\pi) = (64°,37.5°)$ in a coincidence measurement.

TABLE III-4(a)

Parameters entering the $(\pi,\pi p)$ calculation on ^{12}C for T_π = 255 MeV. (θ_p,θ_π) = (55°,50°) P_p is the recoil proton momentum, P_F the Fermi momentum, T_π' the scattered pion energy and $\sigma^\pm$ are the corresponding $\pi^\pm p$ total cross sections.

P_p(MeV/c)	P_F(MeV/c)	T_π'	σ^+	σ^-
100	202.995	231.748	129.951	47.389
150	151.097	226.044	138.697	50.071
200	97.955	217.524	152.571	54.343
250	43.715	206.243	171.678	60.218
300	15.505	192.265	193.348	66.794
350	71.425	175.666	206.700	70.719
400	130.683	156.530	190.741	65.938
450	191.953	134.940	138.841	50.458
500	255.410	110.977	79.392	31.992
550	321.543	84.706	37.262	17.991
600	391.517	56.153	14.049	9.578
650	469.242	25.177	3.568	5.579

TABLE III-4(b)

Parameters entering the $(\pi,\pi p)$ calculation on $^{27}A\ell$ for T_π = 255 MeV. (θ_p,θ_π) = (55°,50°). P_p is the recoil proton momentum, P_F the Fermi momentum, T_π' the scattered pion energy and $\sigma^\pm$ are the corresponding $\pi^\pm p$ total cross sections.

P_p(MeV/c)	P_F(MeV/c)	T_π'	σ^+	σ^-
100	206.964	240.558	117.469	43.601
150	154.985	234.346	126.138	46.226
200	101.749	225.463	139.614	50.353
250	47.183	213.975	158.553	56.186
300	8.846	199.960	182.005	63.369
350	66.257	183.509	202.891	69.627
400	125.261	164.724	202.135	69.319
450	185.936	143.708	162.206	57.474
500	248.461	120.567	101.205	38.896
550	313.164	95.406	51.451	22.835
600	380.741	68.315	21.800	12.478
650	453.049	39.354	7.052	6.864

TABLE III-4(c)

Parameters entering the $(\pi,\pi p)$ calculation on ^{63}Cu for T = 255 MeV. $(\theta_p,\theta_\pi) = (55°,50°)$. P_p is the recoil proton momentum, P_F the Fermi momentum, T_π' the scattered pion energy and $\sigma^{\pm}$ are the corresponding $\pi^{\pm}p$ total cross sections.

P_p(MeV/c)	P_F(MeV/c)	T_π'	σ^+	σ^-
100	208.229	243.218	113.955	42.547
150	156.202	236.781	122.662	45.170
200	102.939	227.736	136.051	49.258
250	48.377	216.151	154.875	55.053
300	7.654	202.112	178.538	62.314
350	64.945	185.715	200.936	69.052
400	123.801	167.066	204.156	69.924
450	184.251	146.279	168.675	59.400
500	246.446	123.467	108.426	41.145
550	310.664	98.746	56.676	24.581
600	377.682	72.226	24.903	13.610
650	448.361	44.003	8.632	7.481

TABLE III-4(d)

Parameters entering the $(\pi,\pi p)$ calculation on ^{208}Pb for $T_\pi = 255$ MeV. $(\theta_p,\theta_\pi) = (55°, 50°)$. P_p is the recoil proton momentum, P_F the Fermi momentum, T_π' the scattered pion energy and $\sigma^\pm$ are the corresponding $\pi^\pm p$ total cross sections.

P_p(MeV/c)	P_F(MeV/c)	T_π'	σ^+	σ^-
100	207.443	241.572	116.115	43.194
150	155.318	235.020	125.165	45.930
200	101.970	225.891	138.937	50.145
250	47.332	214.256	158.077	56.039
300	8.688	200.202	181.619	63.251
350	66.062	183.830	202.629	69.550
400	124.930	165.249	202.638	69.469
450	185.364	144.574	164.415	58.132
500	247.513	121.925	104.553	39.941
550	311.650	97.421	54.555	23.875
600	378.345	71.180	24.040	13.297
650	449.042	43.313	8.382	7.383

TABLE III-4(e)

Parameters entering the $(\pi,\pi p)$ calculation on ^{12}C for T_π = 255 MeV. (θ_p,θ_π) = (64°, 37.5°). P_p is the recoil proton momentum, P_F the Fermi momentum, T_π' the scattered pion energy and $\sigma^\pm$ are the corresponding $\pi^\pm p$ total cross sections.

P_p(MeV/c)	P_F(MeV/c)	T_π'	σ^+	σ^-
100	130.824	232.923	128.212	46.859
150	79.344	226.850	137.431	49.682
200	28.912	217.951	151.857	54.123
250	33.139	206.282	171.611	60.197
300	86.599	191.911	193.816	66.934
350	143.228	174.915	206.775	70.737
400	201.711	155.379	188.643	65.318
450	262.036	133.389	134.633	49.183
500	324.427	109.026	75.379	30.702
550	389.393	82.355	34.618	17.069
600	458.153	53.394	12.638	9.037
650	535.074	21.957	3.012	5.422

TABLE III-4(f)

Parameters entering the $(\pi,\pi p)$ calculation on $^{27}A\ell$ for T_π = 255 MeV. (θ_p,θ_π) = (64°, 37.5°). P_p is the recoil proton momentum, P_F the Fermi momentum, T_π' the scattered pion energy and $\sigma^\pm$ are the corresponding $\pi^\pm p$ total cross sections.

P_p(MeV/c)	P_F(MeV/c)	T_π'	σ^+	σ^-
100	133.285	241.076	116.776	43.393
150	81.490	234.705	125.619	46.068
200	29.104	225.660	139.303	50.257
250	26.979	214.006	158.501	56.170
300	81.677	199.823	182.221	63.434
350	138.238	183.205	203.133	69.697
400	196.283	164.252	201.660	69.177
450	255.881	143.069	160.561	56.983
500	317.202	119.764	99.252	38.285
550	380.566	94.440	50.014	22.352
600	446.658	67.188	20.965	12.172
650	517.325	38.065	6.656	6.710

TABLE III-4(g)

Parameters entering the $(\pi,\pi p)$ calculation on ^{63}Cu for T_π = 255 MeV. (θ_p,θ_π) = (64°, 37.5°). P_p is the recoil proton momentum, P_F the Fermi momentum, T_π' the scattered pion energy and $\sigma^\pm$ are the corresponding $\pi^\pm p$ total cross sections.

P_p(MeV/c)	P_F(MeV/c)	T_π'	σ^+	σ^-
100	134.095	243.438	113.670	42.462
150	82.246	236.934	122.447	45.105
200	29.582	227.820	135.920	49.218
250	25.492	216.166	154.850	55.046
300	80.408	202.056	178.628	62.341
350	136.890	185.589	201.057	69.088
400	194.759	166.870	204.008	69.880
450	254.091	146.013	168.020	59.205
500	315.033	123.133	107.582	40.883
550	377.855	98.345	56.027	24.365
600	443.113	71.759	24.515	13.470
650	512.211	43.471	8.439	7.406

TABLE III-4(h)

Parameters entering the $(\pi,\pi p)$ calculation on ^{208}Pb for T_π = 255 MeV. (θ_p,θ_π) = (64°, 37.5°). P_p is the recoil proton momentum, P_F the Fermi momentum, T_π' the scattered pion energy and $\sigma^\pm$ are the corresponding $\pi^\pm p$ total cross sections.

P_p (MeV/c)	P_F (MeV/c)	T_π'	σ^+	σ^-
100	133.474	241.638	116.028	43.168
150	81.608	235.066	125.100	45.910
200	29.151	225.916	138.898	50.133
250	26.797	214.260	158.070	56.037
300	81.468	200.185	181.646	63.260
350	137.902	183.792	202.660	69.259
400	195.733	165.190	202.583	69.453
450	255.010	144.494	164.213	58.072
500	315.869	121.825	104.305	39.863
550	378.573	97.301	54.367	23.812
600	443.662	71.041	23.927	13.256
650	512.502	43.155	8.325	7.361

TABLE III-5(a)

P's and Q's and the corresponding ratio of π^+ to π^- cross section for the $(\pi,\pi p)$ measurement on ^{12}C for T_π = 255 MeV, for $\theta p, \theta_\pi$ = 55°, 50°. $\sigma_{N,abs}$ = 0.

P_p (MeV/c)	Q^+	P^+	Q^-	P^-	Ratio
100.0	0.1009	0.0866	0.1009	0.0866	1.130
150.0	0.1103	0.0722	0.1103	0.0722	1.401
200.0	0.1185	0.0566	0.1185	0.0566	1.789
250.0	0.1243	0.0419	0.1243	0.0419	2.315
300.0	0.1281	0.0293	0.1281	0.0293	3.0169
350.0	0.1324	0.0202	0.1324	0.0202	3.861
400.0	0.1436	0.0149	0.1436	0.0149	4.713
450.0	0.1698	0.0125	0.1698	0.0125	5.464
500.0	0.2142	0.0115	0.2142	0.0115	6.105
550.0	0.2690	0.0107	0.2690	0.0107	6.6662
600.0	0.3179	0.0094	0.3179	0.0094	7.130
650.0	0.3351	0.0076	0.3351	0.0076	7.499

TABLE III-5(b)

P's and Q's and the corresponding ratio of π^+ to π^- cross section for the $(\pi,\pi p)$ measurement on ^{27}Al for T_π = 255 MeV, for θ_p,θ_π = 55°, 50°. $\sigma_{N,abs}$ = 0.

P_p(MeV/c)	Q^+	P^+	Q^-	P^-	Ratio
100.0	0.0699	0.0610	0.0680	0.0593	1.080
150.0	0.0758	0.0518	0.0738	0.0504	1.313
200.0	0.0809	0.0419	0.0788	0.0407	1.634
250.0	0.0842	0.0324	0.0819	0.0314	2.051
300.0	0.0861	0.0239	0.0837	0.0232	2.598
350.0	0.0878	0.0171	0.0853	0.0165	3.297
400.0	0.0929	0.0126	0.0902	0.0122	4.075
450.0	0.1066	0.0104	0.1036	0.0101	4.816
500.0	0.1334	0.0097	0.1299	0.0094	5.469
550.0	0.1717	0.0094	0.1678	0.0092	6.056
600.0	0.2135	0.0088	0.2096	0.0086	6.580
650.0	0.2415	0.0076	0.2377	0.0075	7.033

TABLE III-5(c)

P's and Q's and the corresponding ratio of π^+ to π^- cross section for the $(\pi,\pi p)$ measurement on ^{63}Cu for T_π = 255 MeV, for θ_p,θ_π = 55°, 50°. $\sigma_{N,abs}$ = 0.

P_p (MeV/c)	Q^+	P^+	Q^-	P^-	Ratio
100.0	0.0383	0.0341	0.0361	0.0321	1.028
150.0	0.0410	0.0298	0.0387	0.0279	1.212
200.0	0.0432	0.0250	0.0407	0.0234	1.453
250.0	0.0445	0.0204	0.0419	0.0191	1.747
300.0	0.0451	0.0161	0.0424	0.0150	2.117
350.0	0.0461	0.0124	0.0431	0.0115	2.597
400.0	0.0486	0.0097	0.0456	0.0090	3.184
450.0	0.0560	0.0084	0.0525	0.0078	3.806
500.0	0.0704	0.0080	0.0664	0.0075	4.408
550.0	0.0922	0.0081	0.0874	0.0076	4.994
600.0	0.1181	0.0079	0.1131	0.0075	5.566
650.0	0.1403	0.0072	0.1354	0.0069	6.104

TABLE III-5(d)

P's and Q's and the corresponding ratio of π^+ to π^- cross section for the $(\pi,\pi p)$ measurement on ^{208}Pb for T_π = 255 MeV, for θ_p,θ_π = 55°, 50°. $\sigma_{N,abs}$ = 0.

P_p (MeV/c)	Q^+	P^+	Q^-	P^-	Ratio
100.0	0.0160	0.0144	0.0136	0.0122	0.912
150.0	0.0170	0.0130	0.0144	0.0109	0.043
200.0	0.0178	0.0114	0.0151	0.0095	1.211
250.0	0.0182	0.0098	0.0154	0.0081	1.401
300.0	0.0184	0.0083	0.0155	0.0069	1.620
350.0	0.0188	0.0070	0.0158	0.0057	1.894
400.0	0.0203	0.0060	0.0170	0.0050	2.243
450.0	0.0240	0.0056	0.0202	0.0047	2.652
500.0	0.0310	0.0057	0.0263	0.0048	3.095
550.0	0.415	0.0060	0.0358	0.0052	3.572
600.0	0.0541	0.0060	0.0480	0.0053	4.080
650.0	0.0654	0.0056	0.0593	0.0051	4.621

TABLE III-5(e)

P's and Q's and the corresponding ratio of π^+ to π^- cross section for the $(\pi,\pi p)$ measurement on ^{12}C for T_π = 255 MeV, for θ_p,θ_π = 64°, 37.5°. $\sigma_{N,abs}$ = 0.

P_p(MeV/c)	Q^+	P^+	Q^-	P^-	Ratio
100.0	0.0992	0.0838	0.0992	0.0838	1.144
150.0	0.1090	0.0686	0.1090	0.0686	1.445
200.0	0.1172	0.0528	0.1172	0.0528	1.869
250.0	0.1222	0.0386	0.1222	0.0386	2.423
300.0	0.1250	0.0268	0.1250	0.0268	3.143
350.0	0.1288	0.0185	0.1288	0.0185	3.994
400.0	0.1402	0.0137	0.1402	0.0137	4.840
450.0	0.1674	0.0117	0.1674	0.0117	5.576
500.0	0.2133	0.0109	0.2133	0.0109	6.201
550.0	0.2694	0.0102	0.2694	0.0102	6.741
600.0	0.3183	0.0090	0.3183	0.0090	7.193
650.0	0.3326	0.0072	0.3326	0.0072	7.552

TABLE III-5(f)

P's and Q's and the corresponding ratio of π^+ to π^- cross section for the $(\pi,\pi p)$ measurement on $^{27}A\ell$ for T_π = 255 MeV, for θ_p,θ_π = 64°, 37.5. $\sigma_{N,abs}$ = 0.

P_p (MeV/c)	Q^+	P^+	Q^-	P^-	Ratio
100.0	0.0678	0.0581	0.0660	0.0564	1.098
150.0	0.0742	0.0484	0.0722	0.0469	1.365
200.0	0.0793	0.0384	0.0772	0.0372	1.726
250.0	0.0823	0.0293	0.0800	0.0284	2.174
300.0	0.0835	0.0215	0.0811	0.0208	2.743
350.0	0.0847	0.0153	0.0822	0.0148	3.452
400.0	0.0893	0.0113	0.0867	0.0110	4.233
450.0	0.1030	0.0094	0.0100	0.0091	4.968
500.0	0.1297	0.0089	0.1262	0.0086	5.611
550.0	0.1683	0.0087	0.1644	0.0085	6.182
600.0	0.2106	0.0082	0.2068	0.0081	6.685
650.0	0.2380	0.0071	0.2342	0.0070	7.122

TABLE III-5(g)

P's and Q's and the corresponding ratio of π^+ to π^- cross section for the $(\pi,\pi p)$ measurement on ^{63}Cu for T_π = 255 MeV, for θ_p,θ_π = 64°, 37.5°. $\sigma_{N,abs}$ = 0.

P_p (MeV/c)	Q^+	P^+	Q^-	P^-	Ratio
100.0	0.0364	0.0316	0.0343	0.0296	1.051
150.0	0.0395	0.0270	0.0372	0.0252	1.275
200.0	0.0418	0.0223	0.0393	0.0208	1.556
250.0	0.0429	0.0179	0.0403	0.0167	1.882
300.0	0.0432	0.0140	0.0405	0.0130	2.276
350.0	0.0437	0.0108	0.0409	0.0100	2.770
400.0	0.0460	0.0085	0.0430	0.0079	3.363
450.0	0.0529	0.0073	0.0496	0.0068	3.991
500.0	0.0668	0.0071	0.0629	0.0066	4.596
550.0	0.0881	0.0072	0.0835	0.0068	5.179
600.0	0.1139	0.0071	0.1090	0.0067	5.738
650.0	0.1359	0.0065	0.1311	0.0062	6.258

TABLE III-5(h)

P's and Q's and the corresponding ratio of π^+ to π^- cross section for the $(\pi,\pi p)$ measurement on ^{208}Pb for T_π = 255 MeV, for θ_p, θ_π = 64°, 37.5°. $\sigma_{N,abs}$ = 0.

P_p (MeV/c)	Q^+	P^+	Q^-	P^-	Ratio
100.0	0.0147	0.0128	0.0124	0.0107	0.946
150.0	0.0159	0.0113	0.0135	0.0094	1.122
200.0	0.0168	0.0097	0.0142	0.0080	1.325
250.0	0.0172	0.0083	0.0144	0.0068	1.537
300.0	0.0172	0.0069	0.0144	0.0057	1.778
350.0	0.0175	0.0058	0.0146	0.0048	2.073
400.0	0.0187	0.0050	0.0156	0.0041	2.438
450.0	0.0221	0.0047	0.0185	0.0039	2.874
500.0	0.0286	0.0048	0.0242	0.0040	3.318
550.0	0.0384	0.0051	0.0331	0.0043	3.807
600.0	0.0506	0.0052	0.0447	0.0045	4.315
650.0	0.0615	0.0049	0.0557	0.0044	4.847

TABLE III-6(a)

P's and Q's and the corresponding ratio of π^+ to π^- cross sections for the $(\pi,\pi p)$ measurement on ^{12}C for T_π = 255 MeV, for θ_p,θ_π = 55°, 50°. $\sigma_{N,abs} \neq 0$.

P_p(MeV/c)	Q^+	P^+	Q^-	P^-	Ratio
100.0	0.0178	0.0072	0.0178	0.0072	2.015
150.0	0.0336	0.0072	0.0336	0.0072	3.161
200.0	0.0475	0.0061	0.0475	0.0061	4.234
250.0	0.0585	0.0050	0.0585	0.0050	5.129
300.0	0.0676	0.0042	0.0676	0.0042	5.791
350.0	0.0754	0.0036	0.0754	0.0036	6.325
400.0	0.0869	0.0034	0.0869	0.0034	6.704
450.0	0.1062	0.0034	0.1062	0.0034	7.023
500.0	0.1372	0.0036	0.1372	0.0036	7.289
550.0	0.1756	0.0038	0.1756	0.0038	7.557
600.0	0.2107	0.0036	0.2107	0.0036	7.817
650.0	0.2255	0.0030	0.2255	0.0030	8.040

TABLE III-6(b)

P's and Q's and the corresponding ratio of π^+ to π^- cross sections for the $(\pi,\pi p)$ measurement on $^{27}A\ell$ for T_π = 255 MeV, for θ_p,θ_π = 55°, 50°. $\sigma_{N,abs} \neq 0$.

P_p (MeV/c)	Q^+	P^+	Q^-	P^-	Ratio
100.0	0.0108	0.0044	0.0106	0.0043	1.955
150.0	0.0207	0.0043	0.0204	0.0042	3.142
200.0	0.0295	0.0036	0.0289	0.0036	4.257
250.0	0.0363	0.0030	0.0355	0.0029	5.188
300.0	0.0418	0.0025	0.0407	0.0024	5.877
350.0	0.0460	0.0021	0.0448	0.0021	6.436
400.0	0.0516	0.0019	0.0502	0.0019	6.831
450.0	0.0609	0.0019	0.0594	0.0018	7.149
500.0	0.0773	0.0020	0.0755	0.0020	7.379
550.0	0.1003	0.0022	0.0982	0.0022	7.591
600.0	0.1258	0.0023	0.1237	0.0022	7.801
650.0	0.1443	0.0021	0.1422	0.0021	8.008

TABLE III-6(c)

P's and Q's and the corresponding ratio of π^+ to π^- cross sections for the $(\pi,\pi p)$ measurement on ^{63}Cu for T_π = 255 MeV, for θ_p,θ_π = 55°, 50°. $\sigma_{N,abs} \neq 0$.

P_p(MeV/c)	Q^+	P^+	Q^-	P^-	Ratio
100.0	0.0050	0.0019	0.0048	0.0018	1.939
150.0	0.0096	0.0019	0.0092	0.0018	3.173
200.0	0.0136	0.0016	0.0130	0.0015	4.318
250.0	0.0167	0.0013	0.0159	0.0012	5.284
300.0	0.0192	0.0011	0.0182	0.0010	6.006
350.0	0.0211	0.0009	0.0200	0.0009	6.581
400.0	0.0236	0.0008	0.0222	0.0008	6.985
450.0	0.0276	0.0008	0.0260	0.0008	7.309
500.0	0.0347	0.0009	0.0329	0.0008	7.527
550.0	0.0450	0.0010	0.0429	0.0009	7.711
600.0	0.0575	0.0011	0.0553	0.0010	7.872
650.0	0.0688	0.0011	0.0667	0.0010	8.022

TABLE III-6(d)

P's and Q's and the corresponding ratio of π^+ to π^- cross sections for the $(\pi,\pi p)$ measurement on ^{208}Pb for T_π = 255 MeV, for θ_p,θ_π = 55°, 50°. $\sigma_{N,abs} \neq 0$.

P_p(MeV/c)	Q^+	P^+	Q^-	P^-	Ratio
100.0	0.0017	0.0005	0.0015	0.0005	1.951
150.0	0.0032	0.0005	0.0028	0.0005	3.285
200.0	0.0046	0.0005	0.0040	0.0004	4.477
250.0	0.0057	0.0004	0.0050	0.0003	5.580
300.0	0.0066	0.0003	0.0057	0.0003	6.466
350.0	0.0073	0.0003	0.0062	0.0002	7.176
400.0	0.0081	0.0002	0.0070	0.0002	7.649
450.0	0.0096	0.0002	0.0082	0.0002	7.992
500.0	0.0121	0.0003	0.0105	0.0002	8.191
550.0	0.0156	0.0003	0.0137	0.0002	8.317
600.0	0.0199	0.0003	0.0178	0.0003	8.368
650.0	0.0238	0.0003	0.0218	0.0003	8.393

TABLE III-6(e)

P's and Q's and the corresponding ratio of π^+ and π^- cross sections for the $(\pi,\pi p)$ measurement on ^{12}C for T_π = 255 MeV, for θ_p,θ_π = 64°, 37.5°. $\sigma_{N,abs} \neq 0$.

P_p(MeV/c)	Q^+	P^+	Q^-	P^-	Ratio
100.0	0.0191	0.0077	0.0191	0.0077	2.027
150.0	0.0357	0.0075	0.0357	0.0075	3.202
200.0	0.0500	0.0062	0.0500	0.0062	4.320
250.0	0.0607	0.0049	0.0607	0.0049	5.255
300.0	0.0691	0.0040	0.0691	0.0040	5.939
350.0	0.0764	0.0034	0.0764	0.0034	6.473
400.0	0.0878	0.0031	0.0878	0.0031	6.836
450.0	0.1077	0.0032	0.1077	0.0032	7.132
500.0	0.1401	0.0035	0.1401	0.0035	7.373
550.0	0.1796	0.0037	0.1796	0.0037	7.623
600.0	0.2150	0.0035	0.2150	0.0035	7.866
650.0	0.2278	0.0029	0.2278	0.0029	8.081

TABLE III-6(f)

P's and Q's and the corresponding ratio of π^+ to π^- cross section for the $(\pi,\pi p)$ measurement on $^{27}A\ell$ for T_π = 255 MeV, for θ_p,θ_π = 64°, 37.5°. $\sigma_{N,abs} \neq 0$.

P_p (MeV/c)	Q^+	P^+	Q^-	P^-	Ratio
100.0	0.0118	0.0047	0.0116	0.0046	1.969
150.0	0.0224	0.0045	0.0220	0.0044	3.1951
200.0	0.0314	0.0037	0.0308	0.0036	4.3648
250.0	0.0381	0.0029	0.0372	0.0028	5.344
300.0	0.0432	0.0024	0.0421	0.0023	6.061
350.0	0.0469	0.0020	0.0457	0.0019	6.625
400.0	0.0522	0.0018	0.0508	0.0017	7.013
450.0	0.0615	0.0017	0.0599	0.0016	7.310
500.0	0.0784	0.0019	0.0764	0.0018	7.514
550.0	0.1021	0.0020	0.0999	0.0020	7.698
600.0	0.1284	0.0022	0.1263	0.0021	7.881
650.0	0.1467	0.0020	0.1446	0.0020	8.0734

TABLE III-6(g)

P's and Q's and the corresponding ratio of π^+ to π^- cross section for the $(\pi,\pi p)$ measurement on ^{63}Cu for T_π = 255 MeV, for θ_p,θ_π = 64°, 37.5°. $\sigma_{N,abs} \neq 0$.

P_p (MeV/c)	Q^+	P^+	Q^-	P^-	Ratio
100.0	0.0056	0.0022	0.0054	0.0021	1.954
150.0	0.0107	0.0020	0.0103	0.0019	3.257
200.0	0.0149	0.0016	0.0142	0.0015	4.495
250.0	0.0180	0.0013	0.0171	0.0011	5.520
300.0	0.0202	0.0010	0.0191	0.0010	6.257
350.0	0.0219	0.0009	0.0206	0.0008	6.825
400.0	0.0241	0.0008	0.0227	0.0007	7.220
450.0	0.0280	0.0007	0.0264	0.0007	7.530
500.0	0.0354	0.0008	0.0335	0.0007	7.728
550.0	0.0461	0.0009	0.0439	0.0009	7.880
600.0	0.0592	0.0010	0.0569	0.0009	8.004
650.0	0.0709	0.0010	0.0687	0.0009	8.126

TABLE III-6(h)

P's and Q's and the corresponding ratio of π^+ to π^- cross section for the $(\pi,\pi p)$ measurement on ^{208}Pb for T = 255 MeV, for $\theta_p, \theta_{\bar{\pi}}$ = 64°, 37.5°. $\sigma_{N,abs} \neq 0$.

P_p (MeV/c)	Q^+	P^+	Q^-	P^-	Ratio
100.0	0.0020	0.0007	0.0018	0.0006	1.975
150.0	0.0038	0.0006	0.0034	0.0005	3.460
200.0	0.0053	0.0005	0.0046	0.0004	4.853
250.0	0.0064	0.0004	0.0055	0.0003	6.065
300.0	0.0071	0.0003	0.0061	0.0002	6.955
350.0	0.0077	0.0002	0.0065	0.0002	7.601
400.0	0.0084	0.0002	0.0072	0.0002	8.009
450.0	0.0099	0.0002	0.0084	0.0002	8.315
500.0	0.0125	0.0002	0.0108	0.0002	8.493
550.0	0.0164	0.0003	0.0143	0.0002	8.588
600.0	0.0210	0.0003	0.0188	0.0002	8.587
650.0	0.0252	0.0003	0.0231	0.0003	8.565

G. REMARKS

The calculations presented here are based on a semiclassical model that does not consider nuclear structure effects. The major purpose of these calculations is to make a qualitative prediction of the effects of recoil nucleon charge exchange on the cross sections.

One of the nuclear structure effects that might be important is that nucleon charge exchange strongly favors transitions between isobaric analog states. Thus the availability of such analog states may have a large effect on the size of P. For example, in a nucleus with a large neutron excess, such as ^{208}Pb, the (p,n) probability might be quite a bit larger than the (n,p) probability. In the formulas above, no distinction between these different charge exchange probabilities was made. In the case of experiments which observe the residual A-1 nucleus, such distinctions would seem to be necessary (see Ref. 51).

To summarize, it is seen that a measurement of the ratio of π^+ to π^- cross sections could provide a sensitive test of the rate of nucleon charge exchange in pion-induced nucleon knock-out processes.

CHAPTER IV

EXPERIMENTAL DETAILS

A. INTRODUCTION

This experiment was performed at the Clinton P. Anderson Meson Physics Facility (LAMPF) of the Los Alamos Scientific Laboratory in Los Alamos. The central part of LAMPF is an 800-MeV proton linear accelerator, which can accelerate H^+ and H^- ions simultaneously, with design average intensities of 1 mA and 100 μA respectively. Figure 16 gives an overview of LAMPF. Here, the area marked 'Beam Area A' is the main pion experimental area.

B. PION BEAM

The beam for the experiment was obtained in the EPICS channel of LAMPF, located in Beam Area A. EPICS, which stands for Energetic Pion Channel and Spectrometer, is the high resolution facility for pion spectroscopy at LAMPF. It consists of a pion channel that provides π^+ or π^- beam and a magnetic spectrometer for analyzing the reaction products. The range of the channel is 50 - 300 MeV and thus covers the region of the (3,3) πN resonance. At the time this study was performed, the spectrometer was still under construction; therefore, it was not used for the experiment.

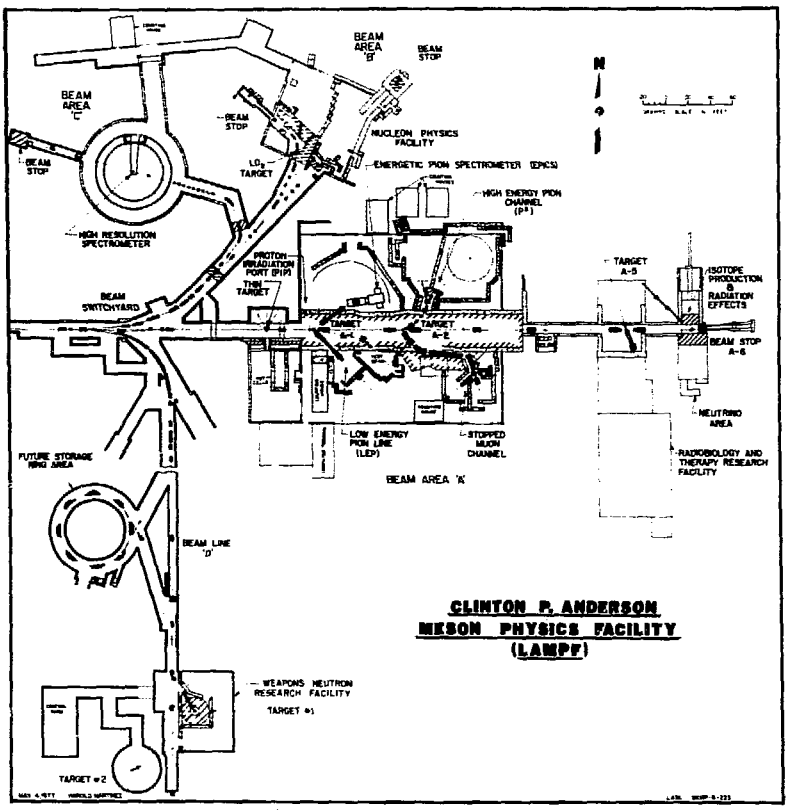

Fig. 16. Overview of LAMPF. Beam Area 'A' is the main pion experimental area.

The EPICS channel is 12.5 meters long and it views a carbon pion production target at 35°. Figure 17 displays the major elements of the channel, which include four dipole magnets (BM01-04), a DC crossed field separator (SEPARATOR), a steering magnet (SM01), three multipole trim magnets (FM01-03) and four collimators (FJ01-04). The dipole magnets bend the beam in a vertical plane and the multipole magnets provide focusing of the beam. The collimator FJ01, which is located at the entrance of the channel, consists of a fixed slit and a movable vertical slit. These two slits together define the acceptance of the channel. Each of the remaining three collimators contains two pairs of movable jaws, one horizontal and the other vertical. The optical mode of the channel, which is indicated in Fig. 17, is point to point (FJ02) to point (FJ04) to point at the target location (FP) in the vertical plane and point to parallel (SEPARATOR) to point (FJ04) to parallel (FP) in the horizontal plane. Thus, the momentum acceptance of the channel is determined by the vertical jaws of FJ04.

The contamination of the beam in the channel is mainly due to protons, electrons and muons. When the polarity of the channel is set for π^+ beam, the proton contamination of the beam becomes very large. The DC crossed-field separator in the channel is designed to reduce this problem. The separator deflects the unwanted particles from the beam and then the horizontal jaws of FJ04 remove them from the beam.

The channel has a 3.4 msr solid angle and a ± 1% momentum bite and can deliver a 20 cm by 7 cm vertically dispersed beam with 100 mr by 10 mr divergence and a momentum resolution of 2×10^{-4} at FWHM.

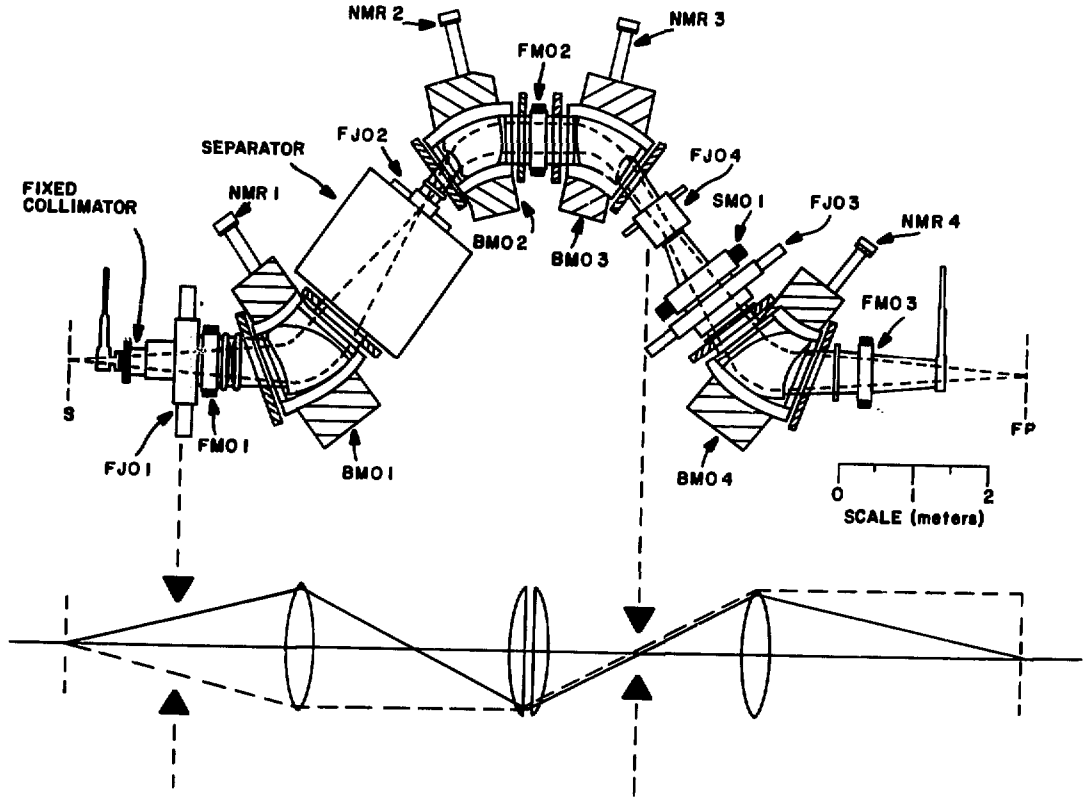

Fig. 17. Major elements of the EPICS channel. The optical mode of the channel is also indicated.

Further details regarding the development and performance of EPICS channel can be found in Ref. 26.

C. EXPERIMENTAL ARRANGEMENT

The experimental setup was designed to permit the observation of recoil protons from the $(\pi,\pi p)$ reaction in singles as well as coincidence modes. A general view of the arrangement of the detector system is given in Fig. 18. The system consisted of a pair of counter telescopes, one for observing the knocked-out protons and the other for detecting the scattered pions.

(i) Proton Detector

The proton detector telescope consisted of two 2-dimensional delay-line readout multiwire proportional chambers (MWPC's), HC1 and HC2, two thin dE/dx counters, ΔE1 and ΔE2, a thick E counter, E and a veto counter, VETO, placed behind the E counter. The MWPC's served to determine particle trajectories in the proton arm of the detector system, while the dE/dx and the E counters together formed the particle identification system.

The counters were made of plastic scintillators. Details of various counters are listed in Table IV-1. The light from each scintillator was collected by lucite light pipes which illuminated one or two phototubes. Pulse-height signals from the phototubes were then digitized in 256-channel ADC's. The E counter was thick enough to stop

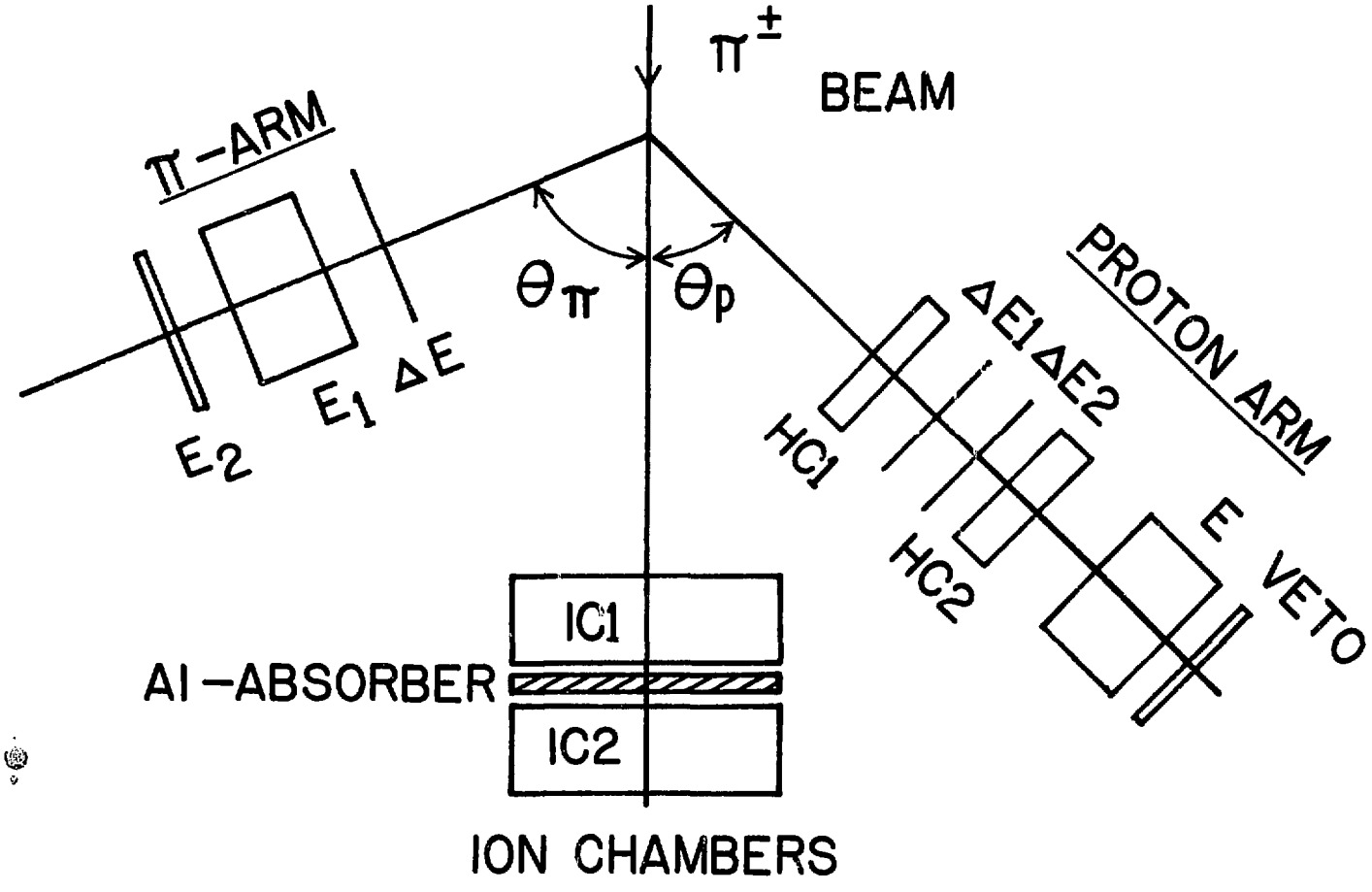

Fig. 18. General view of the arrangement of the detector system.

TABLE IV-1

DETECTION EQUIPMENT DETAILS

A: Proton Arm

HC1-2	Identical two-dimensional delay line read out multiwire proportional chambers with helical cathodes V x H x T = 26 x 16 x 8 cm
ΔE1-2	Plastic scintillation counter; two phototubes V x H x T = 30 x 20 x 12 cm
VETO	Plastic scintillation counter, one phototube V x H x T = 30 x 20 x 0.6 cm

B: Pion Arm

ΔE	Plastic scintillation counter; one phototube V x H x T = 24 x 20 x 0.15 cm
E1	Plastic scintillation counter; one phototube V x H x T = 24 x 14.5 x 14.5 cm
E2	Plastic scintillation counter, one phototube V x H x T = 24 x 20 x 2.4 cm

protons of energy less than 140 MeV. Protons having energies in excess of 140 MeV as well as all energetic pions were eliminated as real events by the VETO counter.

The MWPC's, HC1 and HC2, were identical[56]. They were similar in construction to the two-dimensional delay line readout helical chambers developed by Lee et al.[57] at LAMPF. The design of the chambers is sketched in Fig. 19. Each chamber contained a helical cathode and an anode plane on the midplane of the cathode helix. The cathode helix was wound from 0.04 mm diameter copper-clad aluminum wire with a pitch of 1 mm, the windings running in the horizontal (x-) direction. The anode plane consisted of equally spaced, discrete vertical (y-axis) wires of 0.02 mm diameter gold-plated tungsten. These wires were soldered directly to an external anode delay line, which was in the form of a cylindrical helix[57], at regular intervals of 2 mm. The total delay times of the cathode and the anode were 400 ns and 100 ns, respectively. The anode-to-cathode spacing was about 4.8 mm and the anode was operated at ground potential while the cathode was maintained at about -3300 volts. Each chamber had an active area of 26 x 16 cm (HxV). A gas handling system maintained a steady flow of a gas mixture, containing nearly 70% argon, 30% isobutane and a trace of freon, through the chambers.

In each chamber the anode signals were taken directly from the two ends of the anode delay line. Since the cathode had high-voltage applied to it, the cathode signals were taken from the ends of the

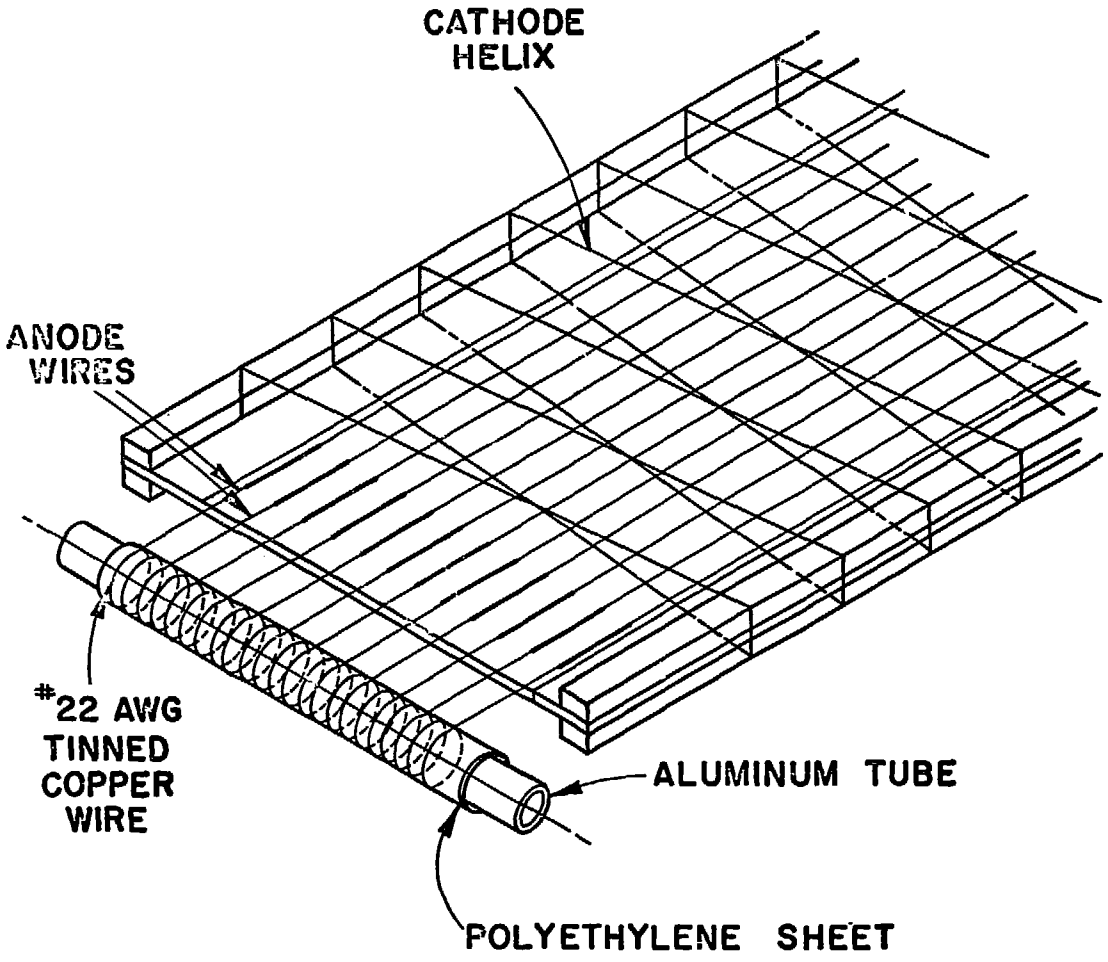

Fig. 19. Design of the two-dimensional delay line readout helical chambers.[57]

cathode helix through coupling capacitors which differentiated the signals from the high-voltage. The time difference between the anode signals corresponded to the active anode wire position (y-coordinate), while that between the cathode signals corresponded to the x-coordinate of the origin of the pulses. The sum of the delay times of the signals in either one of the delay lines was a measure of the electrical length of that delay line. To determine these parameters, the anode and cathode signals from each chamber were first standarized with fast discriminators and then digitized in 2048-channel TDC's. The time bases of the anode and cathode TDC's were 1 μsec and 250 nsec, respectively.

(ii) Pion Detector

The pion detector telescope consisted of a thin dE/dx counter, ΔE, a thick E counter, E1, and a thin counter, E2, placed behind E1. Details of these counters are listed in Table IV-1. The E2 counter was used either in a 3-fold coincidence with the ΔE and E1 counters to detect pions or in a veto mode to reject events from the (p,2p) reaction.

(iii) Beam Monitoring System

The beam monitoring system consisted of a pair of identical ion chambers, IC1 and IC2, placed at zero degrees to the incident pion beam and connected to current integrators. A 3.18 cm thick aluminum absorber placed between the ion chambers stopped any residual

protons that traversed the front chamber, IC1. Thus, IC1 gave information about all particles in the beam, viz., π, μ, e, and p, while the back chamber, IC2, monitored only the (π,μ,e) component of the beam. The π^+ and π^- rates per charge collected in the ion chambers were known from a previous experiment[58] and are displayed in Fig. 20 as a function of the incident pion energy.

D. ELECTRONICS

The electronics setup for the experiment was compatible with the data acquisition system which involved a CAMAC unit. Details of the data acquisition system are presented in Section E of this chapter.

In designing the electronics, the philosophy was to log all proton singles events occuring in the proton arm as valid events, at the same time tagging those which were accompanied by a coincident pion event in the pion arm. Consequently, the electronics involved two fast logic systems, one which established a proton event (hereafter referred to as EVENT) in the proton arm and the other which provided the tag signal for establishing π-p coincidence.

A schematic of EVENT fast-logic is given in Fig. 21. The signature of a valid event (EVENT) was defined to be the proton-arm coincidence:

$$\Delta E1 \cdot \Delta E2 \cdot E_t \cdot E_b \cdot HC1 \cdot HC2 \cdot \overline{VETO} \ ,$$

where E_t and E_b refer to pulse-height signals from the top and bottom ends of the thick E counter in the proton arm. The above coincidence

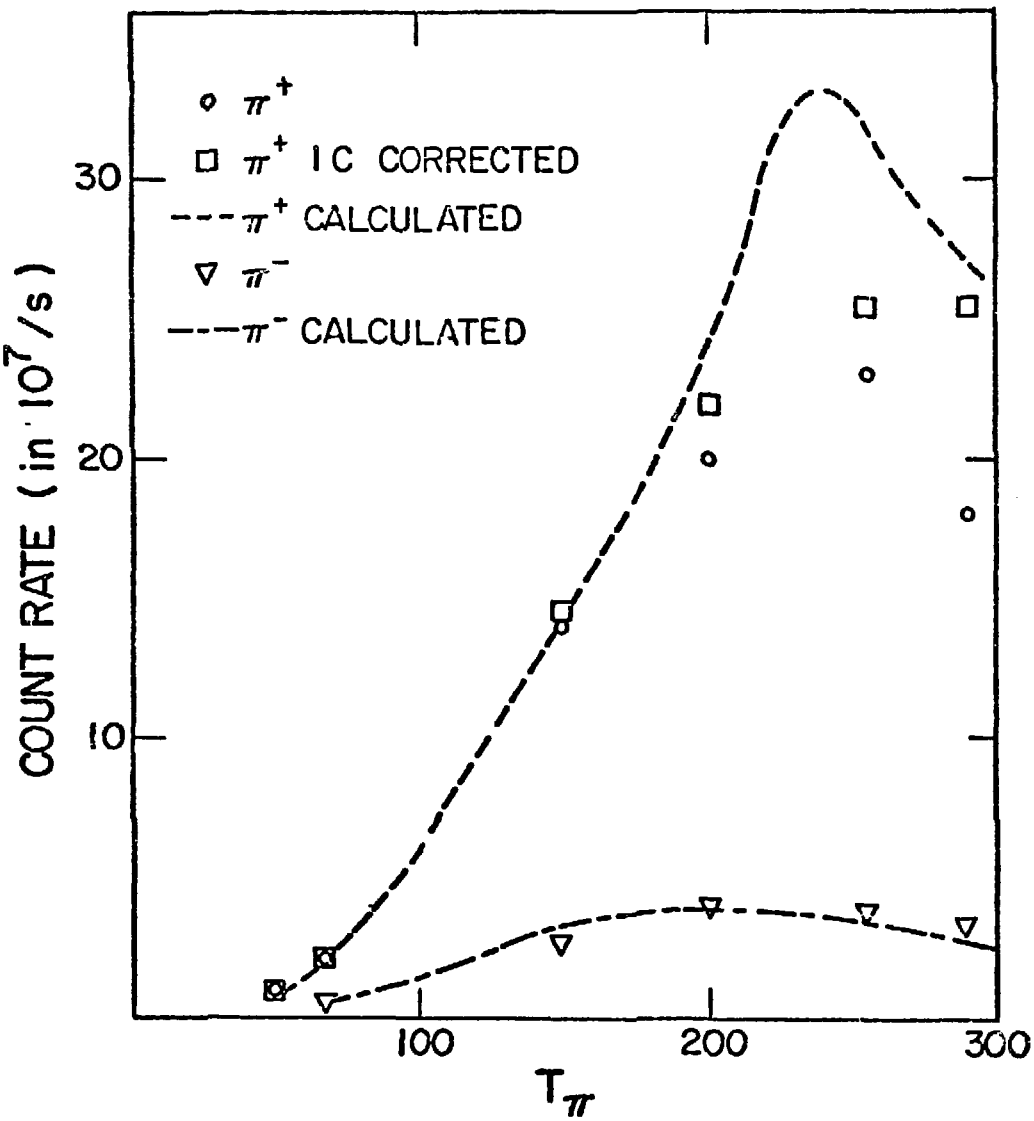

Fig. 20. π^+ and π^- rates per charge collected in the ion chamber as functions of the incident pion energy T_π [58].

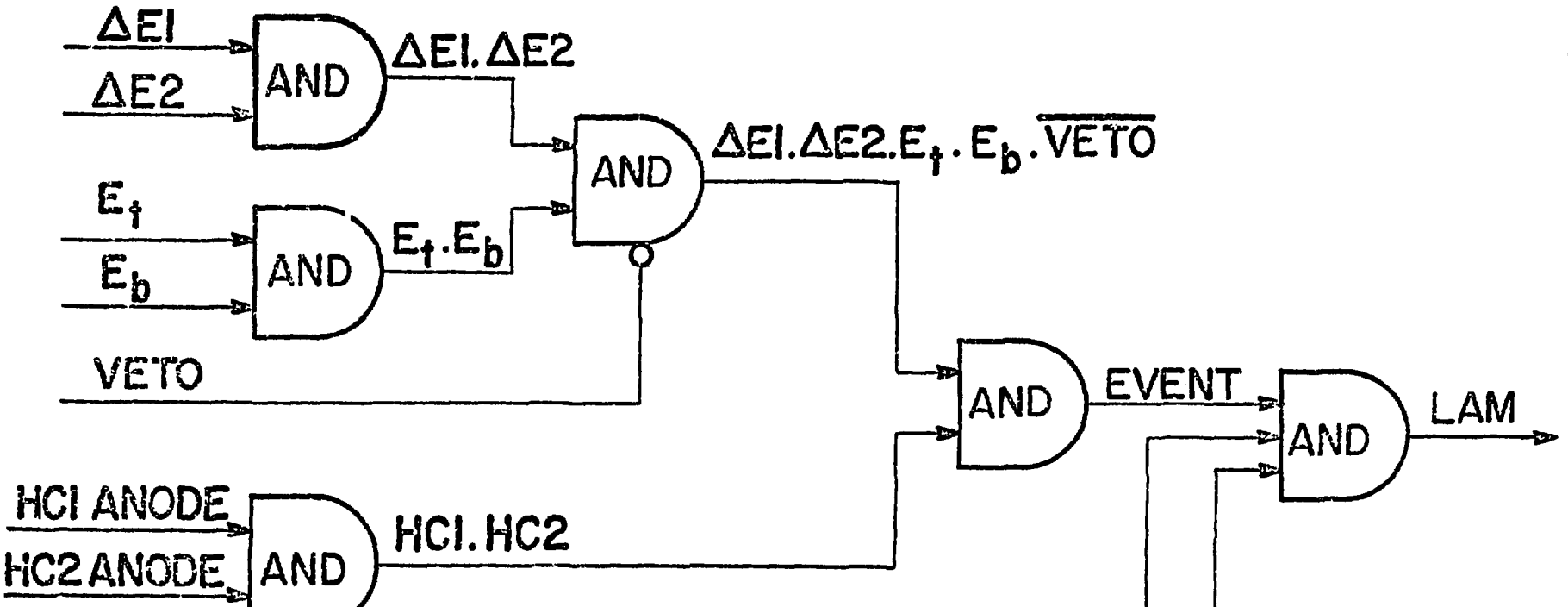

Fig. 21. Schematic of the EVENT fast logic.

triggered an event which corresponded to a particle that traversed ΔE1, ΔE2, E, HC1, and HC2, but not the VETO counter, i.e., a particle other than an energetic pion. The LAM signal to the CAMAC controller was obtained from the coincidence, EVENT•BEAM GATE•$\overline{\text{BUSY}}$, where the BUSY signal corresponded to the dead-time of the electronics as well as of the computer and the BEAM GATE was IN, whenever the incident pion beam was ON.

The fast-logic system for tagging (π-p) coincidence events is shown in Fig. 22. It was assumed that a pion event in the pion arm triggered ΔE, E1, and E2 counters. Thus, a coincidence among these counters, ΔE•E1•E2, provided the π-EVENT signal. A coincidence between this and the EVENT signal, therefore, defined a (π-p) coincidence, which in Fig. 22 is indicated as a π-p EVENT. A π-p EVENT set a particular bit (#0) of a Coincidence Register (C212) and thus tagged the (π-p) coincidences.

A special feature of the electronics arrangement was that the start signals for the MWPC TDC's were derived from the EVENT•BEAM GATE•$\overline{\text{BUSY}}$ signal. This necessitated delaying the TDC stop signals appropriately; however, this choice of the start signal reduced the number of random triggers considerably.

Eight scalers counted various signals. The scaled parameters are indicated in Fig. 23, which provides a diagram of the electronics setup.

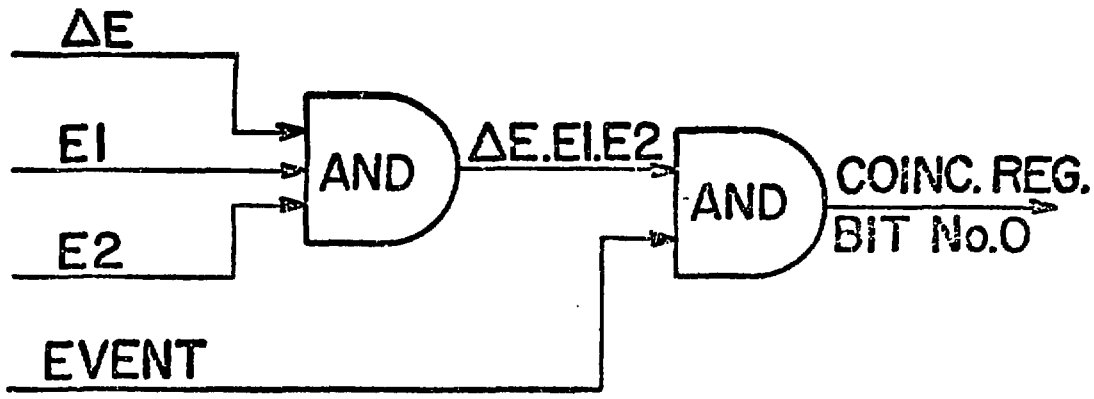

Fig. 22. π-p coincidence logic.

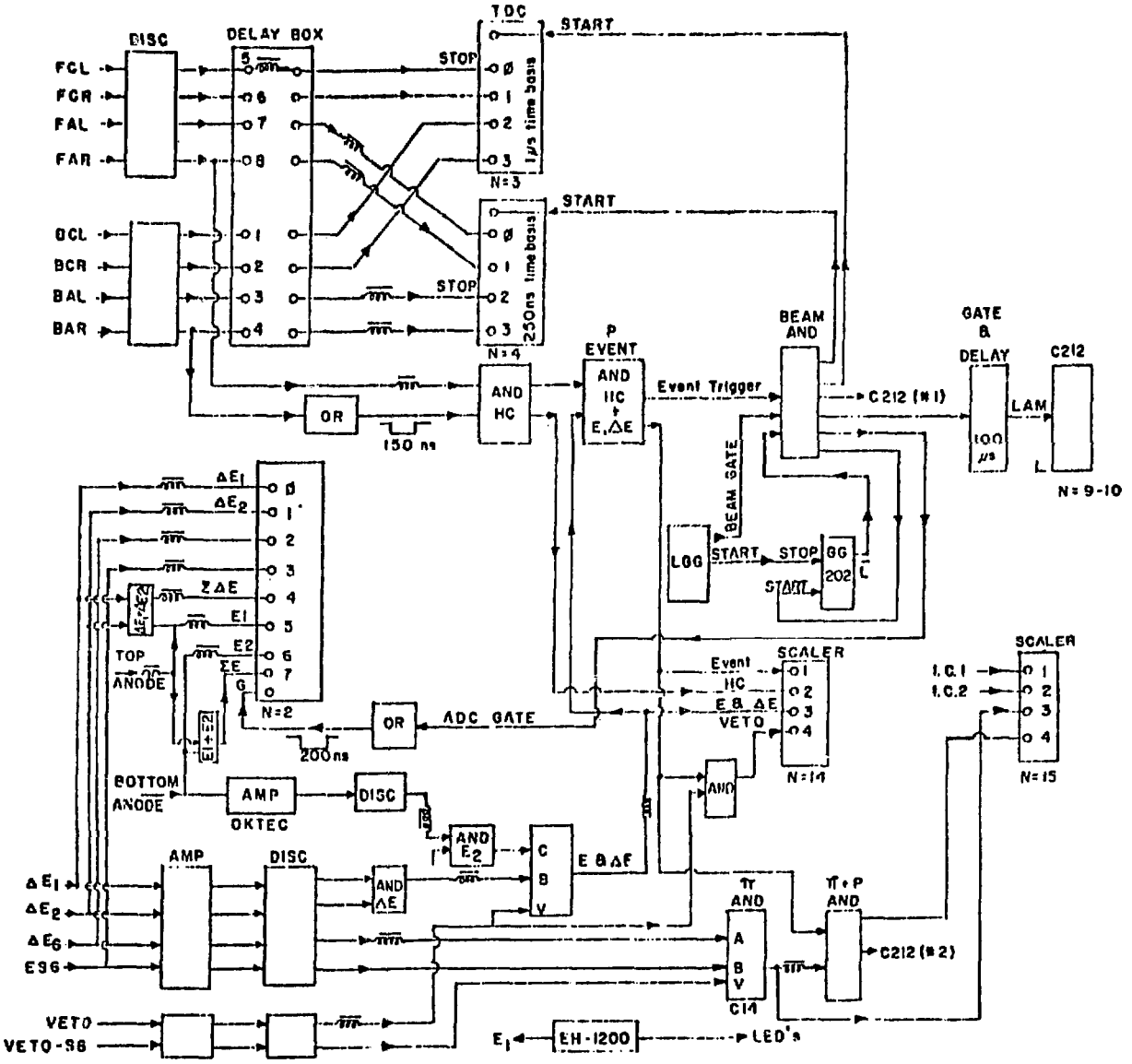

Fig. 23. Diagram of the electronics setup.

E. DATA ACQUISITION SYSTEM

The data acquisition system was centered around a PDP11/10 computer which was coupled to a CAMAC data control unit. The computer had 28 K word memory and had a 300,000 word disk unit, a 9-track magnetic tape unit and a Tektronix 4010 terminal as peripherals. The computer was run under the RT-11 operating system which permitted the system operation in the Foreground and Background modes. A MACRO code, CAREAD[59], written specifically for this experiment ran in the Foreground (FG), controlling transfer from the CAMAC unit. A flow-chart of CAREAD is given in APPENDIX F. A command from the computer, via CAREAD, prompted the CAMAC controller to read out the ADC's, TDC's, Scalers and the Coincidence Register. Altogether, there were 21 words in an event buffer, the format of which is given in APPENDIX G. CAREAD provided for a buffer size of 256 words and, therefore, accommodated 11 events per buffer. When 11 events were read out by the CAMAC unit, CAREAD transferred the data to the computer for processing and, whenever taping was enabled, recorded the data on the magnetic tape.

A FORTRAN program[60], which ran in the Background (BG), provided the communication link between the FG program CAREAD and the experimenter. In addition, this BG program served to perform on-line analysis of the data.

F. DETECTOR PERFORMANCE

(i) Multiwire Proportional Chambers

The chambers were calibrated, using a collimated ^{55}Fe X-ray line-source. This source was positioned at known distances from the center of the chamber in both X and Y directions and the time signals were read out in TDC's. The position information obtained from the TDC outputs (in channel numbers) was fitted to the known distance of the source from the center of the chamber to yield a position calibration of the chamber in mm/TDC channel. Figure 24 shows samples of data for the difference between positive and negative time signals for the cathode and anode planes in HC1, for three different locations of the source. Table IV-2 summarizes the results of the calibration measurements on the MWPC's.

From the position information obtained from the chambers, the trajectory of the particle traversing the proton arm was determined as follows: if (x_1,y_1) and (x_2,y_2) are the positions in the chambers HC1 and HC2, respectively, then the X and Y slopes of the trajectory are given by

$$b_x = \frac{x_2 - x_1}{D} \quad , \quad b_y = \frac{y_2 - y_1}{D}$$

where, D is the distance between the planes. Once the slope was known, the trajectory of the particle could be projected to the target as well as to the various counters in the proton arm. By establishing cuts

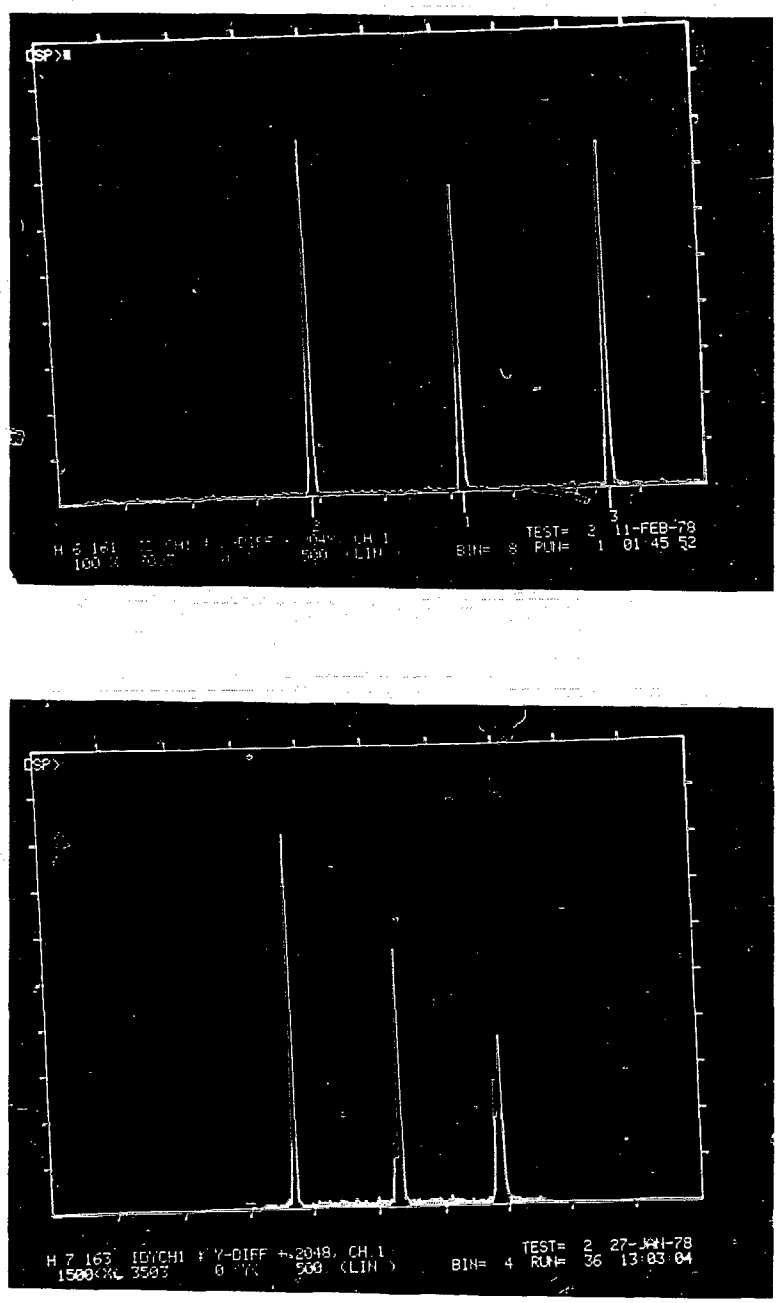

Fig. 24. Difference between positive and negative time signals for (a) the cathode and (b) the anode signal planes in HCl as a function of TDC channel number.

TABLE IV-2

MWPC CALIBRATION PARAMETERS

Plane	Source Location*	Peak location in channel no.s**	Calibration Coefficients*** A(mm)	B(mm/ch)
HC1 - Anode	-2"	359.0		
	center	517.0	-164.66	0.32
	2"	678.0		
HC1 -Cathode	-2"	432.0		
	center	519.0	-304.8	0.59
	2"	605.0		
HC2 - Anode	-2"	351.5		
	center	510.5	-162.34	0.32
	2"	671.0		
HC2 -Cathode	-2"	428.0		
	center	515.0	-304.2	0.59
	2"	600.0		

* Relative to the center of the chamber
** Average of 3 measurements
*** Linear fit: $y = A + Bx$

on the projections to the target, it was possible to determine whether the particle originated in the target. Figures 25(a) and 25(b) show the results of such projections to the target: (a) includes all events, while (b) shows events that originate in the target.

(ii) Scintillation Counters

The energy calibration of the counters was obtained by placing the detector system in direct monoenergetic proton beams obtained in the EPICS channel. This procedure resulted in a linear calibration of the counters in MeV per ADC channel. Thus, by knowing the pulse-height in a given counter (in terms of ADC channels), the corresponding energy could be determined. Results of the energy calibration of various counters are summarized in Table IV-3.

Since the VETO counter vetoed only those events which corresponded to particles reaching it, the EVENT fast logic permitted triggering of EVENTS by particles other than protons which were stopped in the E counter. Consequently, the proton-arm particle spectrum contained these particles as well. In order to identify protons in this spectrum, in the present study, the E-dE/dx method was employed. Figure 26 shows a sample E-dE/dx plot obtained for the proton arm. It is seen that the loci of protons are well separated from those of low energy pions and other particles. By establishing cuts on the E-dE/dx plots it was possible to separate protons from other particles.

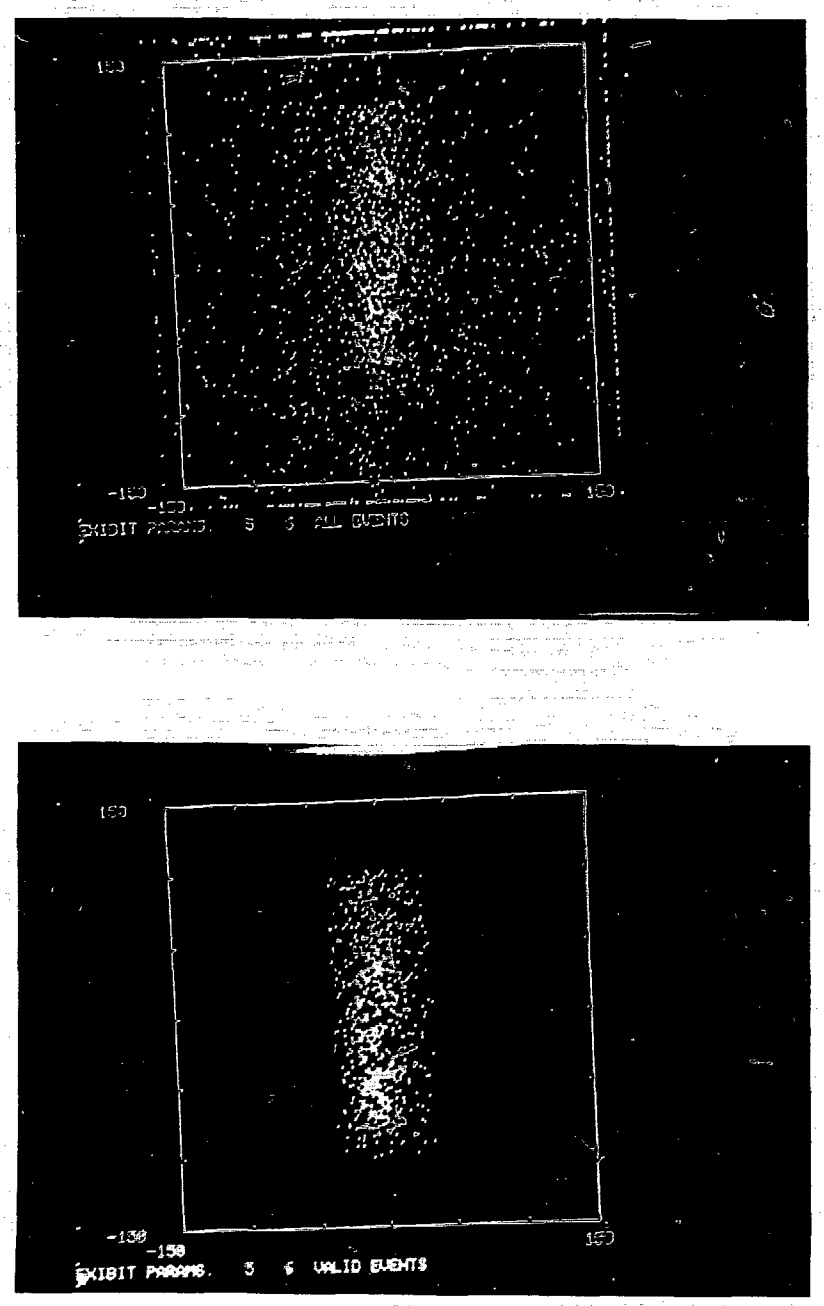

Fig. 25. Two-dimensional plot of the projections of particle trajectories to the target: (a) with no cuts on data; (b) with cuts.

TABLE IV-3

CALIBRATION PARAMETERS FOR COUNTERS

Counter	Calibration Coefficients A (MeV)	B (MeV/ch)
ΔE1	-0.4	0.041
ΔE2	-0.47	0.063
E_t	10.80	0.487
E_p	7.60	0.581
ΔE	-2.33	0.067
E_1	-3.64	0.606

* Linear fit to data: $y = A + Bx$, where y is the energy and x is the channel number.

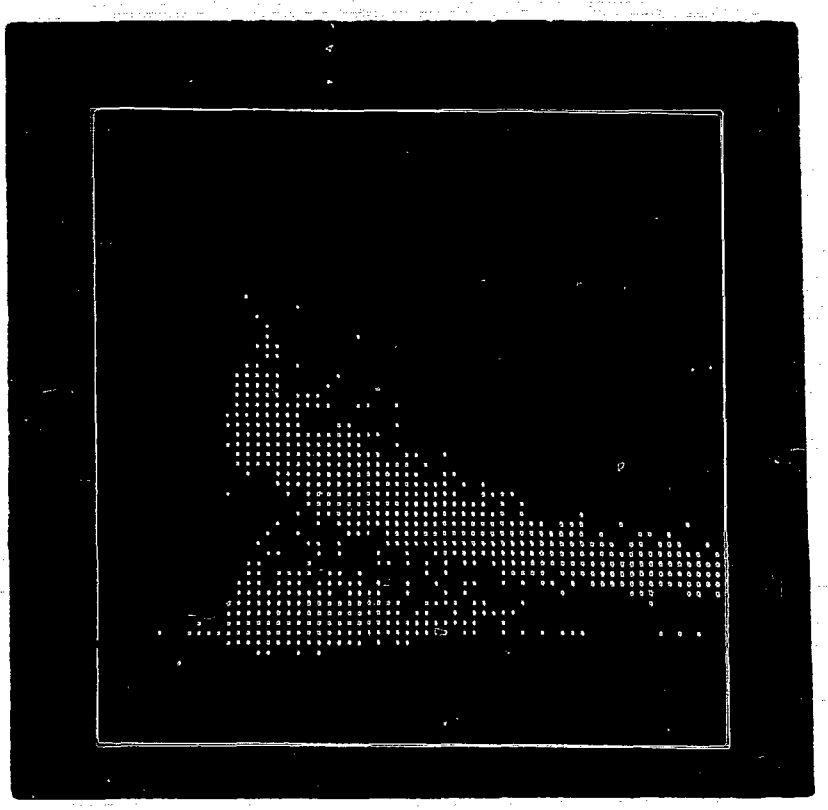

Fig. 26. $E - \frac{dE}{dx}$ plot obtained for the proton arm.

G. TARGETS

Within the limited running time which the LAMPF Scheduling Committee allotted to the experiment, only two targets could be studied. These were ^{27}Al and ^{208}Pb.

The targets were 8 x 20 cm rectangular sheets and were mounted on aluminum frames. These targets were large enough to cover the spot-size of the EPICS pion beam. The ^{208}Pb target was fabricated from ∿99% isotopically pure lead and had 250 mg/cm^2 thickness. Two ^{27}Al targets were employed, one having 100 mg/cm^2 and the other 350 mg/cm^2. Both were fabricated from natural aluminum. The thicker one was used mainly with π^- beam, whose intensity was nearly 7 times smaller than that of the π^+ beam.

H. DATA ACQUISITION

The experiment was run at T_π = 255 MeV, using both π^+ and π^- beams. Data were taken at four angular settings, θ_p, θ_π = 45°, 67°; 55°, 50°; 64°, 37.5°; and 90°, 50°. This range was enough to scan most of the region of interest and show that no striking changes with angle were present. To estimate background contributions, data were taken with a blank target.

For π^+ runs, the crossed-field separator was used for removing most of the protons from the beam. The ratio of IC1 to IC2 counts indicated that the proton contamination of the beam was only 1-2%.

Typical proton EVENT rates for the π^+ beam incident on the $^{27}A\ell$ and ^{208}Pb targets for $\theta_p = 55°$ were 48.5 and 16.0 counts/sec for proton singles data and 0.28 and 0.07 counts/sec for the coincidence data, respectively. Corresponding rates for the π^- beam were 3.5 and 1.92 counts/sec for the singles data and 3.4×10^{-3} and 1.4×10^{-3} counts/sec for the coincidence measurements. These rates were obtained with incident beam intensities of $(15.3 \pm 2.2) \times 10^7$ particles/sec for π^+ beam and $(2.3 \pm 0.2) \times 10^7$ particles/sec for π^- beam.

CHAPTER V

DATA ANALYSIS AND RESULTS

A. INTRODUCTION

During the operation of the experiment, some analysis of the experimental data had been done, but this was done primarily as a check to see how well the experiment was operating. A more detailed analysis had to be done before meaningful conclusions could be arrived at.

B. OFFLINE DATA ANALYSIS

The offline analysis of the data was performed on the PDP 11/10 computer using a Fortran code QUASEL, written specifically for this experiment. This code, which ran under the SINGLE JOB (S/J) monitor of the RT-11 operating system, consisted of six segments which were arranged in five overlays. These segments were stored on the disk. The main calling routine was short and resided in the central memory. The parameters for initializing an analysis run and the histograms were kept in a common block in the main routine.

A simplified flow chart of QUASEL is shown in Fig. 27. Segment 1 served to initialize the program. In this segment, an analysis run was defined, a disk file containing the constants needed for the calculation of various parameters, the gates for particle

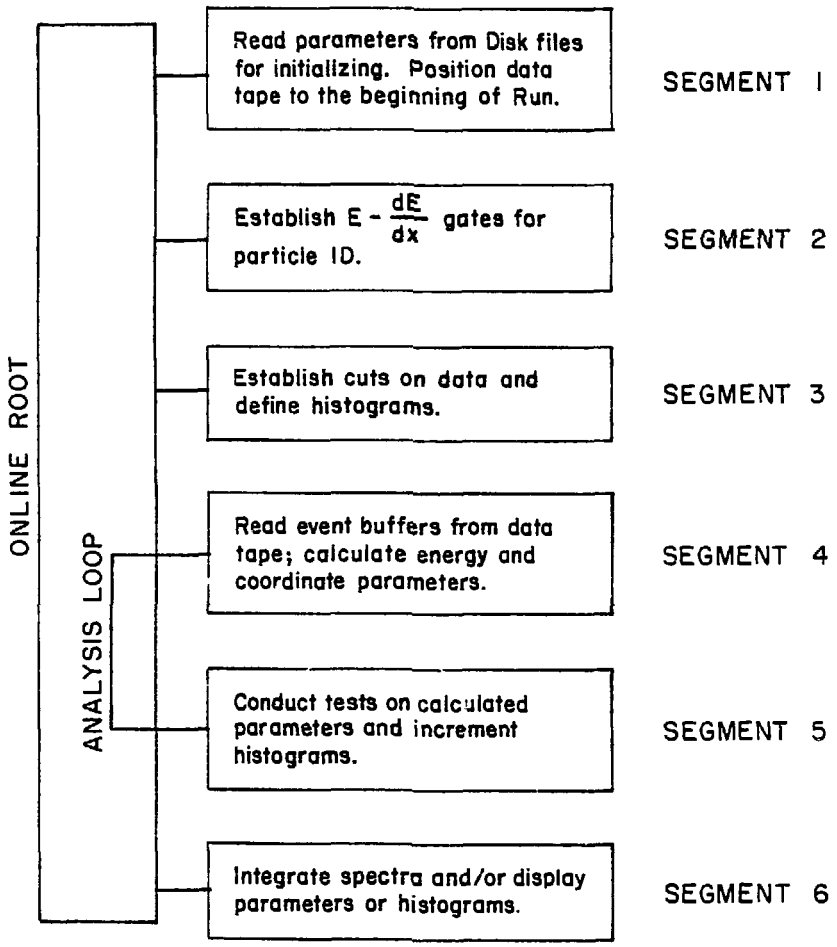

Fig. 27. Simplified flow chart of QUASEL.

ID's and the tests on the parameters was read in and the magnetic tape was positioned to read the event buffer corresponding to a desired experimental run. In Segment 2, one could read in a desired number of data blocks from the magnetic tape and display two-dimensional E-dE/dx plots for either observing the existing gates for particle ID's or drawing these gates anew. There was also a provision for printing out the two-dimensional plot. At the end of the operation of Segment 2, the tape would rewind to the beginning of the data block. Also, if new gates were established, these were recorded on the disk in the file for initializing runs. Segment 3 provided for establishing various tests on the parameters calculated and defined various histograms. Once these tests were established, a summary of the tests could be printed out. The tests were also stored on the disk file. Thus, once a set of gates for particle ID's was established in Segment 2 and a set of tests was defined in Segment 3, the functions of these segments could be by-passed in later runs; at the time of initialization of a run in Segment 1, these data were read in from the disk file.

Segments 4 and 5 constituted the analysis loop. In these segments, event buffers were read in from the magnetic tape, various parameters corresponding to each event were calculated, the tests defined in Segment 3 were performed on these parameters and the histograms were incremented. Segment 6 provided for the display of the histograms and the integration of the spectra and their print out

and storage of the histograms in disk files. Once in the analysis loop (Segments 4 and 5), the only functions that were allowed were display of histograms, integration of the spectra, or termination of the analysis run. On completion of the analysis loop, the run was ended through a command, upon which the scaler information contained in the trailer block on the data tape were read in and stored in a common block.

Altogether, 25 parameters were calculated for each event. Of these, 13 corresponded to wire chamber information, i.e., trajectories in various elements of the proton-arm and the remaining 12 were energy parameters. Table V-1 gives a list of these 25 parameters and their limiting values.

As was mentioned in Chapter IV, particle identification in each of the detector arms was accomplished by the E-$\frac{dE}{dx}$ technique. The clear separation of protons from other particles in the proton arm, obtained by this technique was illustrated in Fig. 26. In order to establish the identity of a particle observed in a given arm, particle identification (ID) gates were established on the E-$\frac{dE}{dx}$ plot for various particles in each arm. Figure 28 illustrates the proton and deuteron gates for the proton arm. The analysis program, QUASEL, after calculating E and $\frac{dE}{dx}$ values corresponding to each particle trajectory, determined the E-$\frac{dE}{dx}$ gate within which these values were located and thus identified the particle

Results of the analysis of singles and coincidence data are presented in the next two sections.

TABLE V-1

No.	Parameter	Limits
01	xl, x-position, HCl	- 80.0 mm to + 80.0 mm
02	yl, y-position, HCl	- 130.0 mm to +130.0 mm
03	x2, x-position, HC2	- 80.0 mm to + 80.0 mm
04	y2, y-position, HC2	- 130.0 mm to +130.0 mm
05	x3, x-position, target	- 37.5 mm to + 37.5 mm
06	y3, y-position, target	- 101.5 mm to +101.5 mm
07	x4, x-position, E counter	- 80.0 mm to + 80.0 mm
08	y4, y-position, E counter	- 130.0 mm to +130.0 mm
09	$\Delta\theta$, horizontal angular dispersion	- 0.12 rad to + 0.12 rad
10	$\Delta\phi$, vertical angular dispersion	- 0.23 rad to + 0.23 rad
11	sum check, HCl	
12	sum check, HC2	
13	θ_p, proton angle	
14	ΔE1	
15	ΔE2	
16	E1 + ΔE2 = ΔESUM	1.5 MeV to 8.5 MeV
17	ET	
18	EB	
19	ET + EB = ESUM	
20	E = ESUM + ΔESUM	25 MeV to 145 MeV
21	ΔE	
22	E1	
23	EPI = ΔE + E1	
24	ΔESUM, hardware	
25	ESUM, hardware	

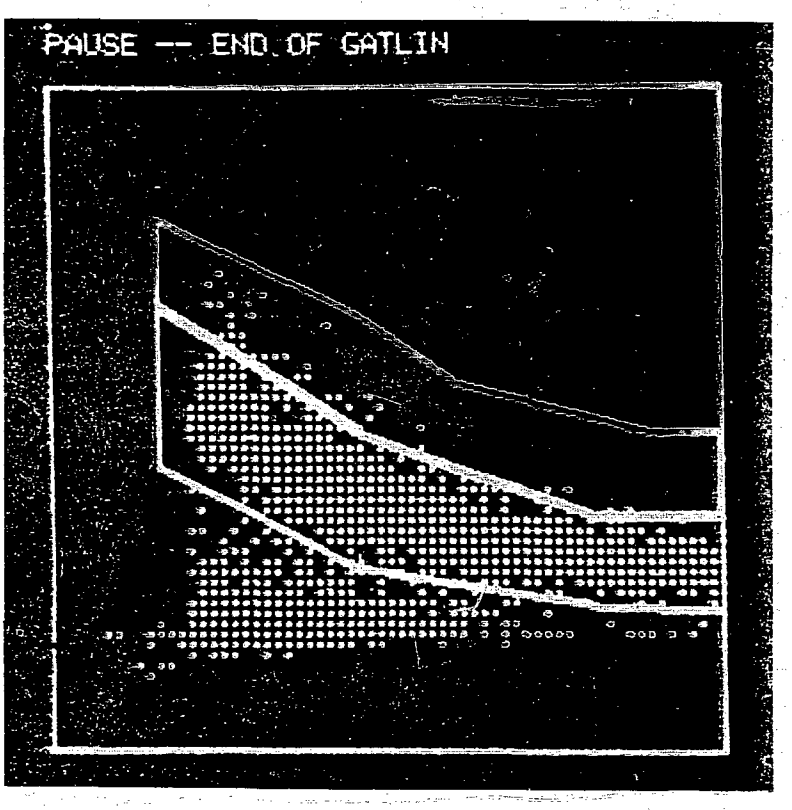

Fig. 28. Particle ID gates for protons and deuterons in the proton arm.

C. SINGLES SPECTRA

Singles spectra were obtained by establishing particle ID gates for protons and deuterons in the proton arm (cf. Fig. 28), but no gates for pions in the pion arm. Figures 29(a)-29(d) display the differential cross sections $d^2\sigma/d\Omega_p dE_p$ for incident π^+ and π^- beams as functions of the knock-out proton kinetic energy (Laboratory) for ^{27}Al, for θ_p = 45°,55° 64° and 90°. Figures 29(e)-29(g) display the same for ^{208}Pb, for θ_p = 45°, 55° and 64°. The error bars shown in these figures reflect primarily statistical uncertainties. Results of the single-arm measurements are summarized in Tables V.2(a)-2(d) for ^{27}Al and in Tables V.3(a)-3(c) for ^{208}Pb. The cross sections presented were calculated by summing the counts in the corresponding spectrum in 10 MeV bites. The total cross sections quoted are the sums obtained by summing over all recoil proton energies. Ratios of π^+ to π^- cross sections were calculated by summing the counts in the spectra for a given θ_p over all recoil proton energies. These ratios are presented in Table V.4.

The singles data indicate that the cross sections for π^+ and π^- incident beams decrease with increasing energy. The initial dip in the cross section is probably due to the energy threshold of the detector system.

The data indicate another significant feature. Inspection of Figs. 29 suggests that the cross sections for both π^+ and π^- particles fall off approximately exponentially with the energy of the observed proton. This feature becomes more prominent when $\theta_p \rightarrow 90°$. Discussion of these results are presented in Section E.

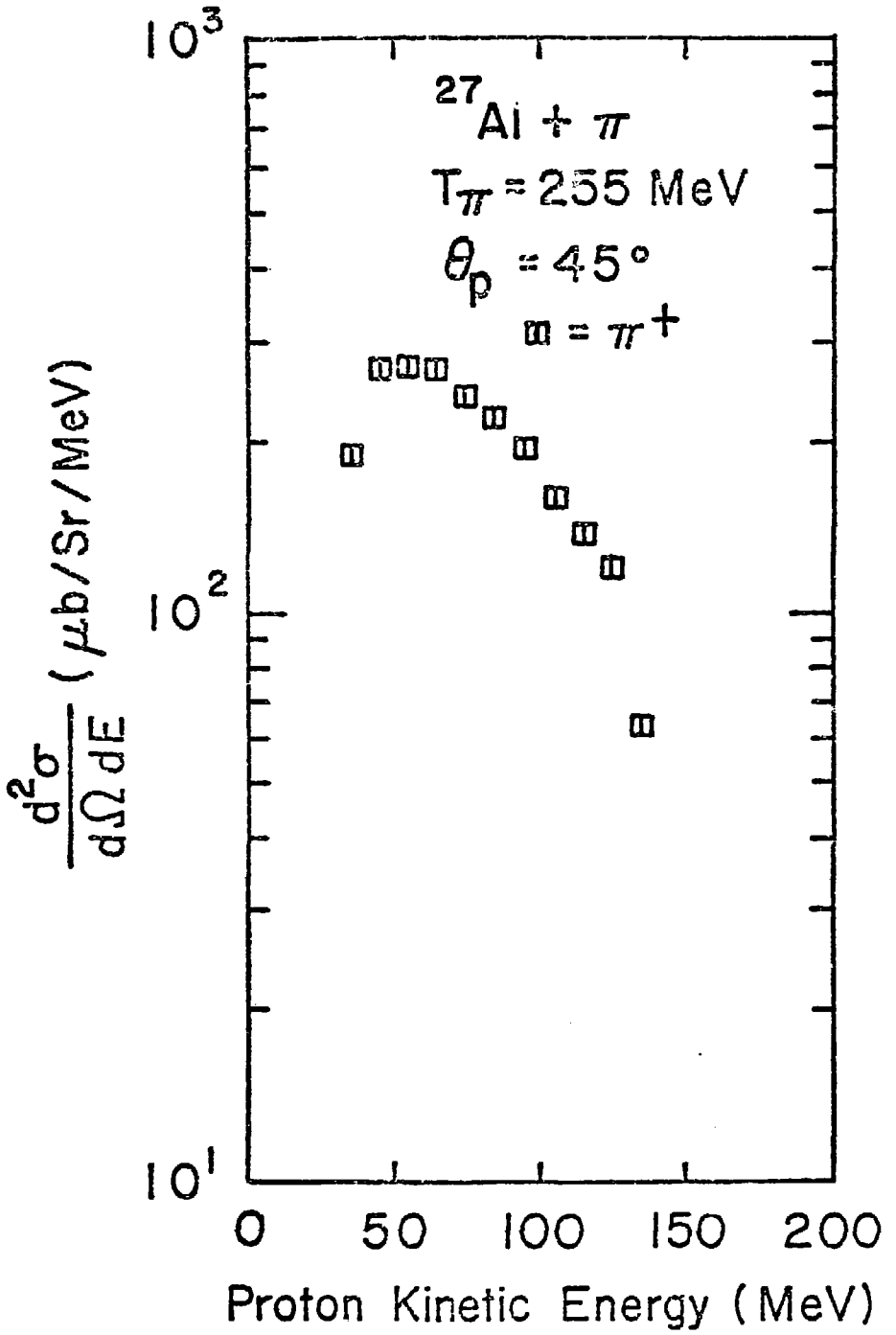

Fig. 29(a). Differential cross section for observing recoil protons at $\theta_p = 45°$ in a single arm measurement on ^{27}Al.

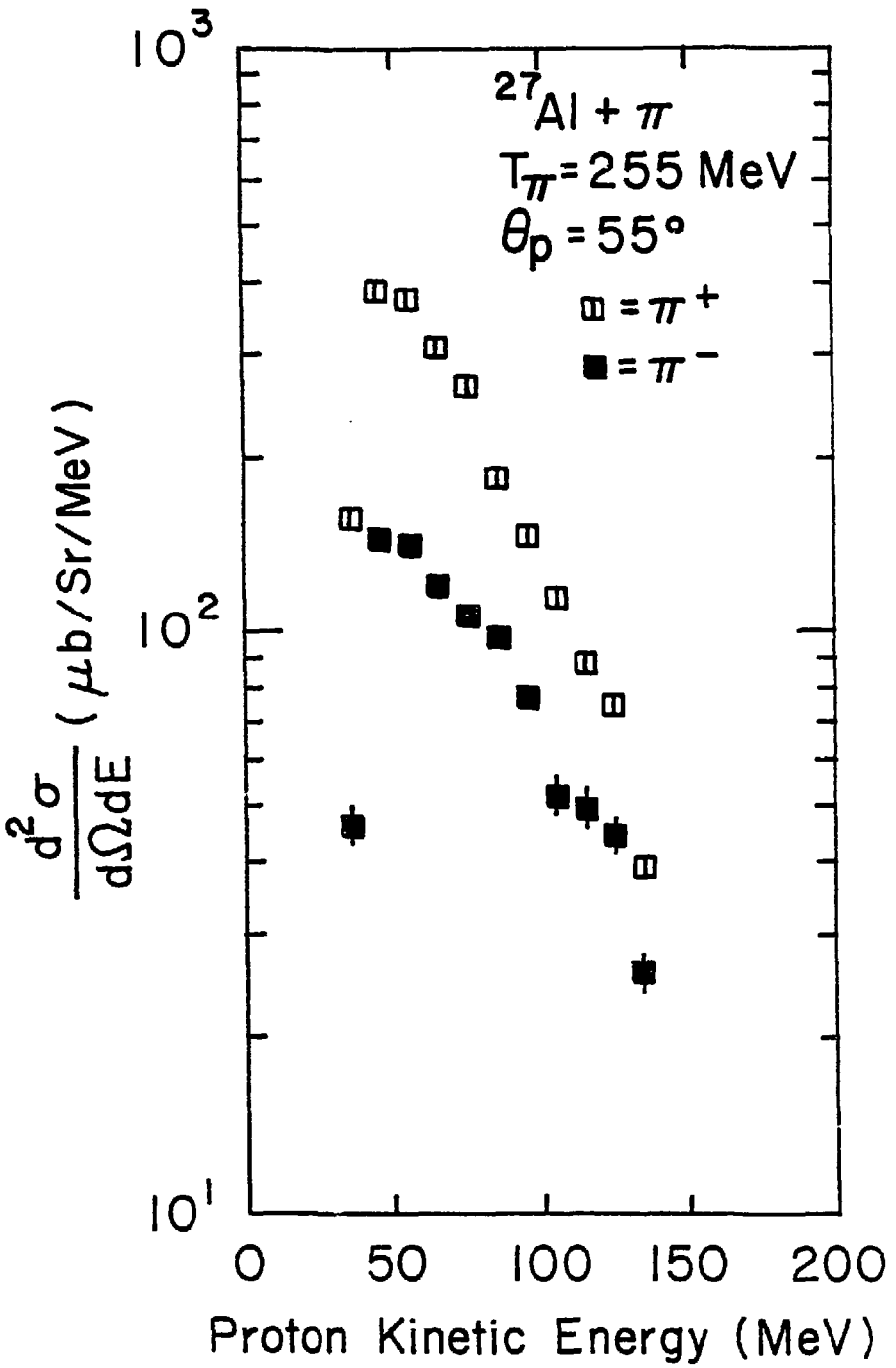

Fig. 29(b). Differential cross sections for obserfing recoil protons at θ_p = 55° in a single-arm measurement on ^{27}Al.

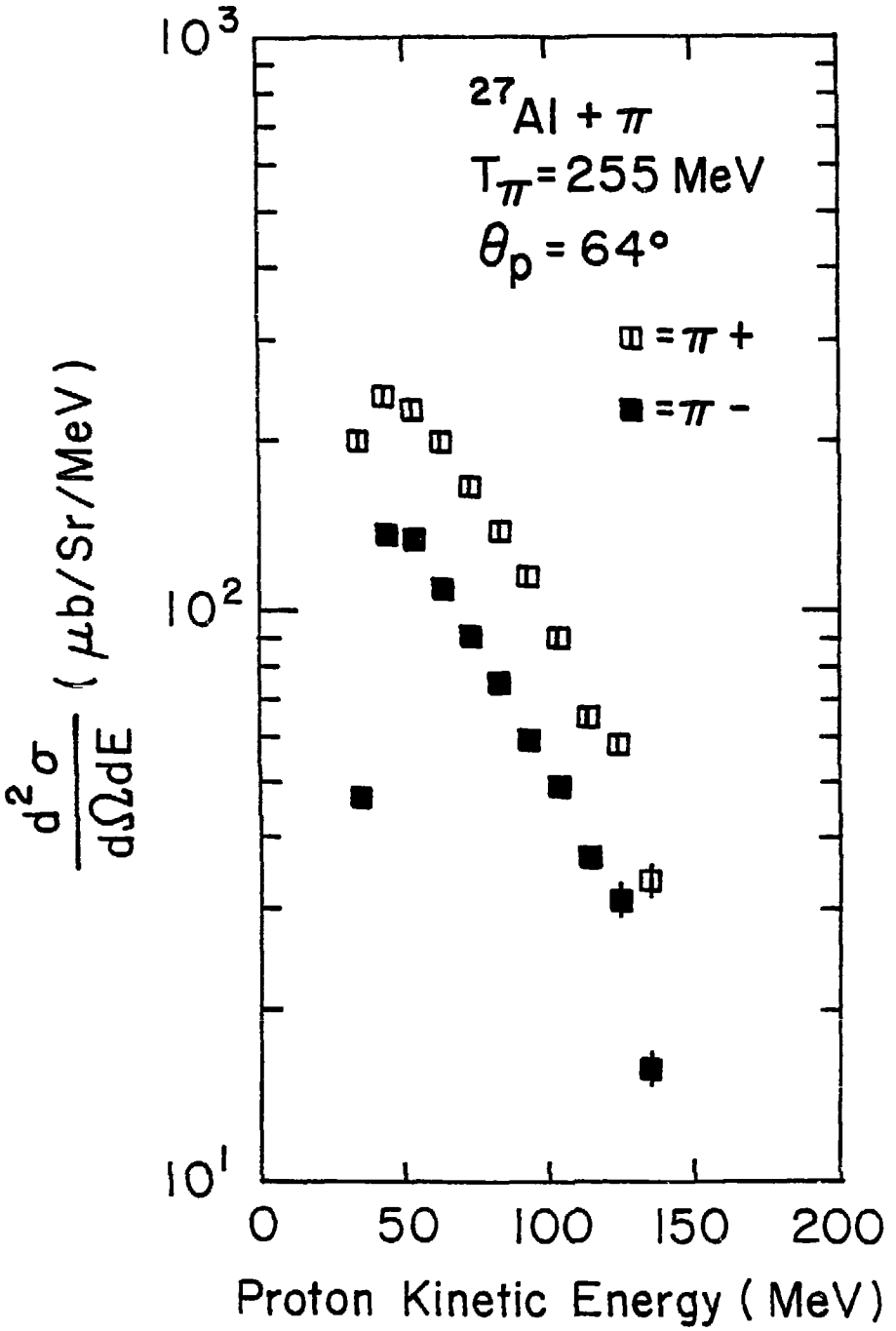

Fig. 29(c). Differential cross sections for observing recoil protons at $\theta_p = 64°$ in a single-arm measurement on ^{27}Al.

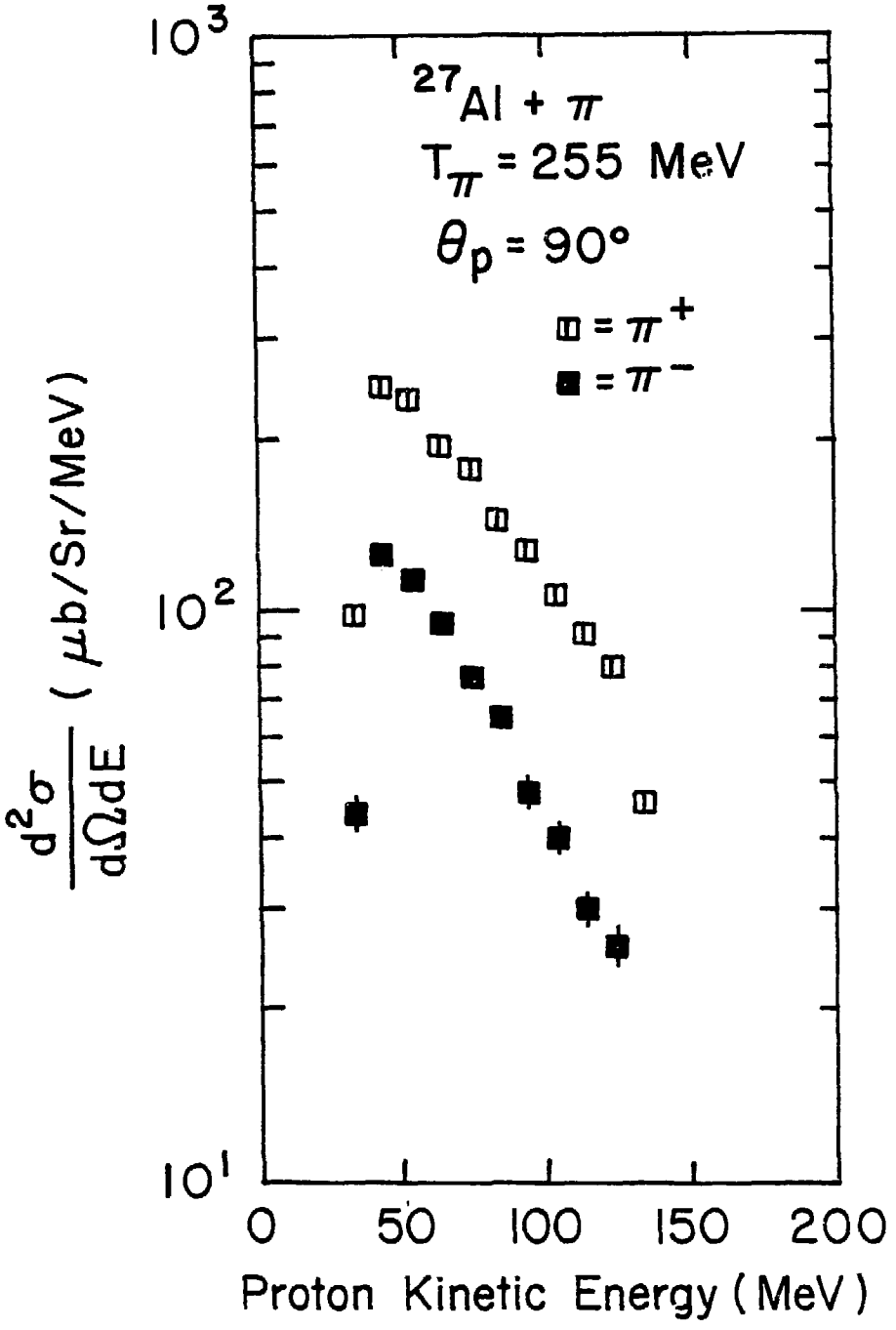

Fig. 29(d). Differential cross sections for observing recoil protons at $\theta_p = 90°$ in a single-arm measurement on ^{27}Al.

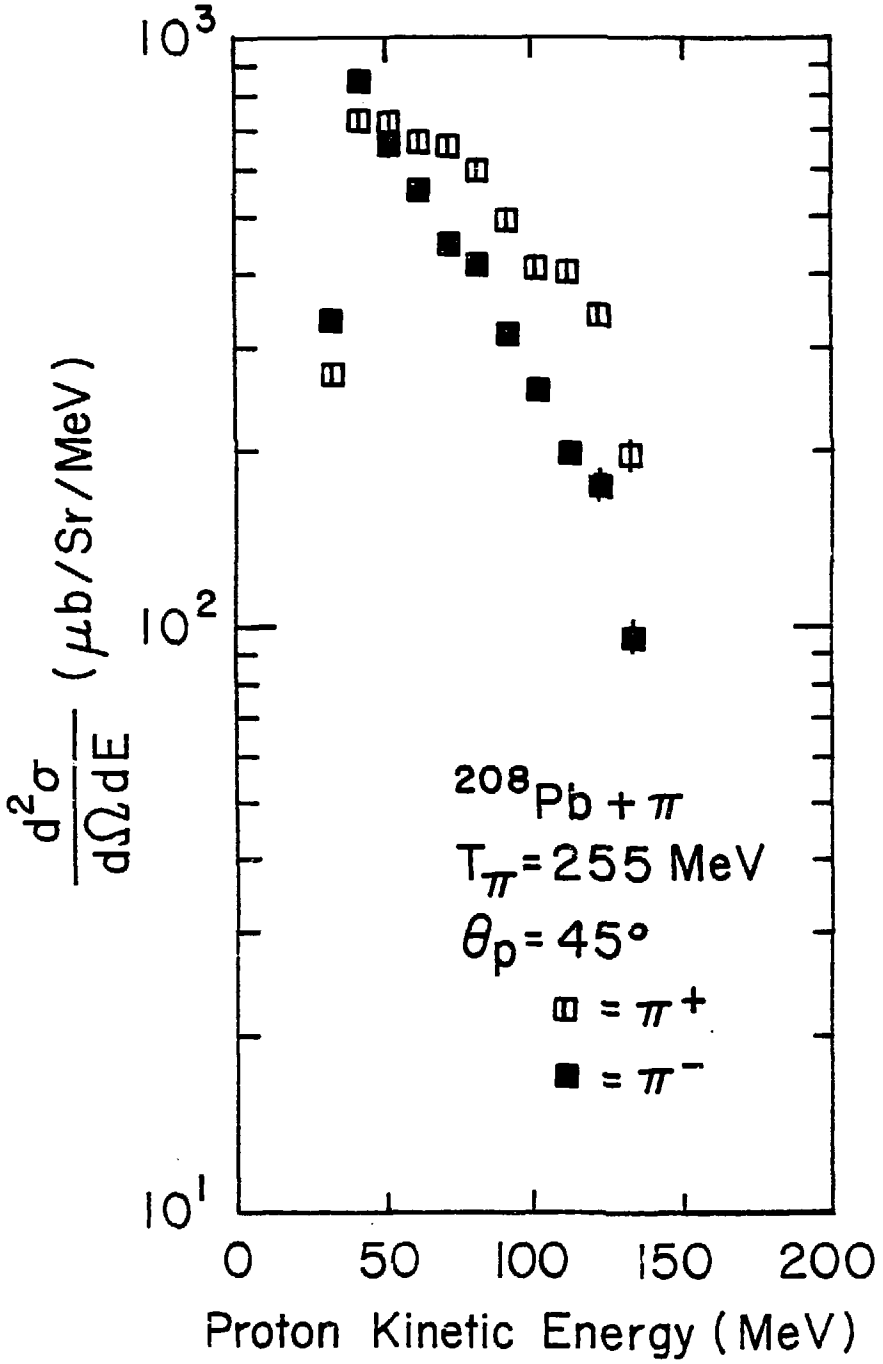

Fig. 29(e). Differential cross sections for observing recoil protons at θ_p = 45° in a single-arm measurement on ^{208}Pb.

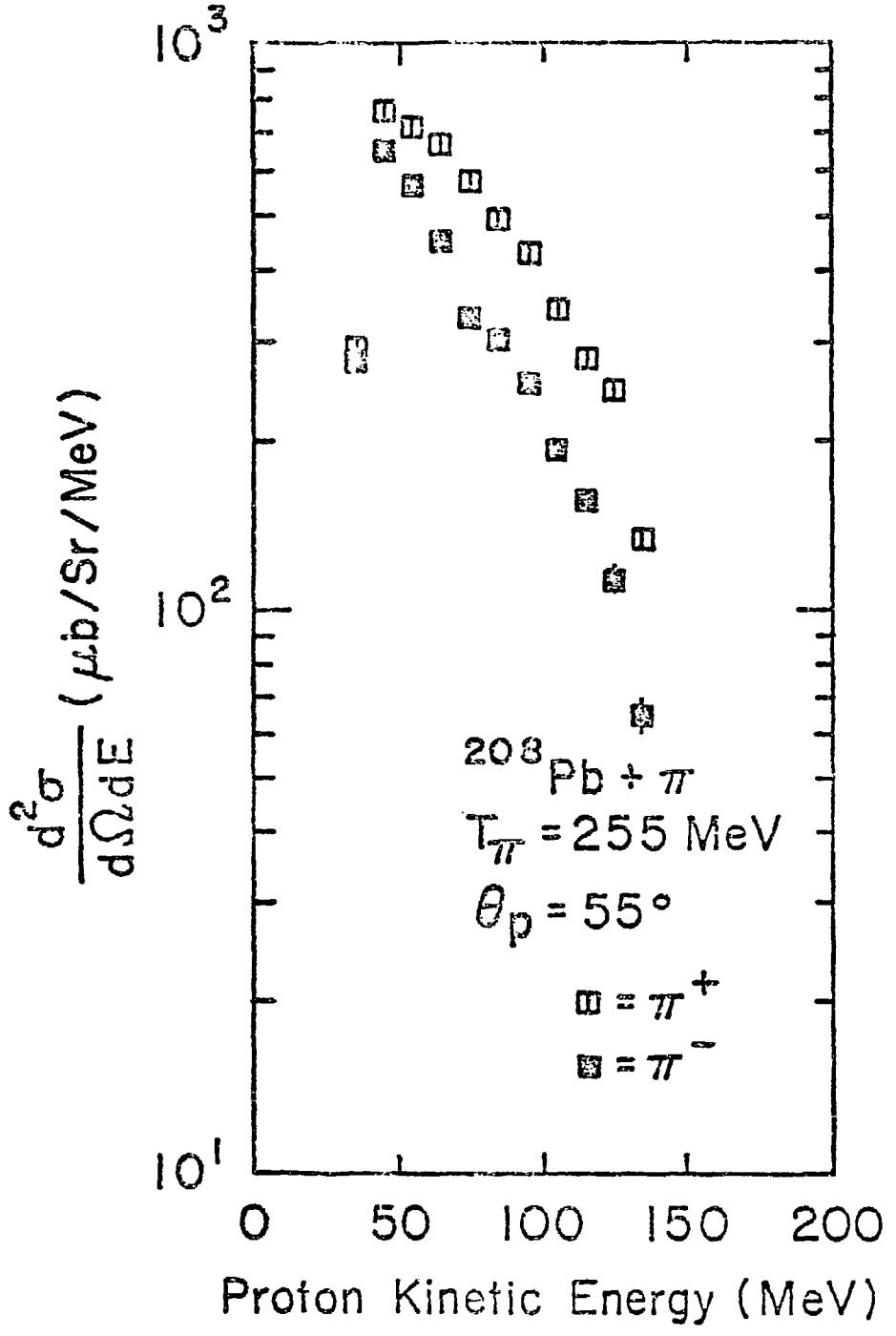

Fig. 29(f). Differential cross sections for observing recoil protons at $\theta_p = 55°$ in a single arm measurement on ^{208}Pb.

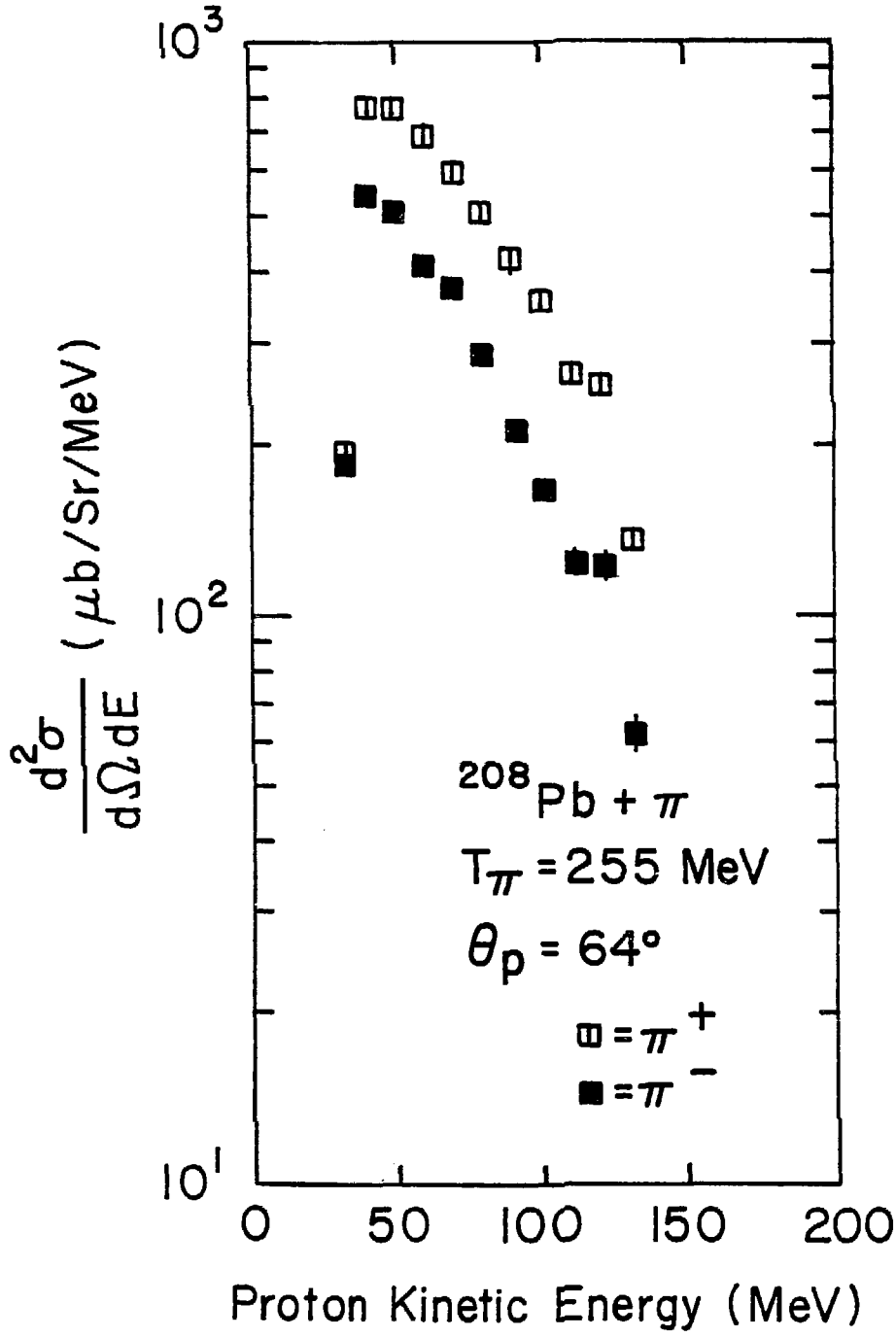

Fig. 29(g). Differential cross sections for observing recoil protons at $\theta_p = 64°$ in a single-arm measurement on ^{208}Pb.

TABLE V-2(a)

Measured π^+ and π^- differential cross sections for $^{27}A\ell$ for $\theta_p = 45°$

T_p (MeV)	σ^+	$\Delta\sigma^+$	σ^-	$\Delta\sigma^-$
35	191.61	3.91		
45	270.53	4.44		
55	272.72	4.42	No Measurement	
65	269.73	4.37		
75	243.36	4.31		
85	222.98	3.50		
95	197.60	3.70		
105	162.04	3.24		
115	140.26	3.07		
125	122.08	2.88		
135	63.74	1.99		

TABLE V-2(b)

Measured π^+ and π^- differential cross sections for $^{27}A\ell$ $\theta_p = 55°$

T_p (MeV)	σ^+	$\Delta\sigma^+$	σ^-	$\Delta\sigma^-$
35	158.04	2.36	46.10	2.14
45	390.81	3.70	146.12	3.79
55	377.42	3.60	142.81	3.70
65	311.89	3.26	121.41	3.39
75	267.13	2.30	107.40	3.18
85	186.41	2.45	98.31	3.08
95	148.65	2.19	77.17	2.72
105	115.88	1.90	52.28	2.44
115	89.51	1.64	49.73	2.17
125	75.52	1.51	44.97	2.07
135	39.56	1.09	25.79	1.57

TABLE V-2(c)

Measured π^+ and π^- differential cross sections for $^{27}A\ell$ for $\theta_p = 64°$

T_p (MeV)	σ^+	$\Delta\sigma^+$	σ^-	$\Delta\sigma^-$
35	199.80	4.12	47.09	1.41
45	239.16	4.17	136.55	2.39
55	227.17	4.01	135.37	2.37
65	199.80	3.81	109.94	2.14
75	166.63	3.46	90.61	1.95
85	138.06	3.10	75.05	1.77
95	115.29	2.89	59.54	1.56
105	89.91	2.48	49.26	1.42
115	65.14	2.03	36.70	1.22
125	58.34	2.01	30.96	1.12
135	33.57	1.53	15.71	0.80

TABLE V-2(d)

Measured π^+ and π^- differential cross sections for ^{27}Al $\theta_p = 90°$

T_p (MeV)	σ^+	$\Delta\sigma^+$	σ^-	$\Delta\sigma^-$
35	98.70	2.15	43.93	1.66
45	247.95	3.43	125.96	2.81
55	233.97	3.32	113.19	2.64
65	194.60	3.04	94.95	2.43
75	178.42	2.92	76.75	2.19
85	144.86	2.62	64.66	2.01
95	127.07	2.46	47.81	1.73
105	106.89	2.25	39.95	1.56
115	91.11	2.08	29.82	1.31
125	79.92	1.93	25.69	1.25
135	45.95	1.57	8.06	0.54

TABLE V-3(a)

Measured π^+ and π^- differential cross sections for ^{208}Pb for $\theta_p = 45°$

T_p (MeV)	σ^+	$\Delta\sigma^+$	σ^-	$\Delta\sigma^-$
35	270.28	8.3	332.79	9.01
45	724.04	13.68	843.96	14.02
55	716.04	13.39	659.45	12.00
65	666.78	13.00	551.87	10.85
75	655.70	12.98	448.18	9.62
85	593.52	12.46	413.62	9.57
95	490.70	11.38	313.84	8.24
105	404.50	9.67	251.96	7.36
115	398.35	10.24	196.78	6.04
125	336.16	9.45	173.36	6.04
135	196.40	7.27	95.32	4.51

TABLE V-3(b)

Measured π^+ and π^- differential cross sections for ^{208}Pb for $\theta_p = 55°$

T_p (MeV)	σ^+	$\Delta\sigma^+$	σ^-	$\Delta\sigma^-$
35	293.06	6.02	279.28	11.80
45	764.68	9.75	652.76	17.48
55	716.65	9.27	568.03	15.80
65	666.78	8.97	453.20	13.85
75	576.89	8.30	331.68	11.49
85	495.62	7.70	303.24	11.49
95	430.36	7.22	254.19	10.45
105	342.32	6.34	194.55	9.08
115	280.13	5.67	157.76	8.09
125	246.27	5.38	113.72	6.72
135	134.22	3.96	65.22	5.15

TABLE V-3(c)

Measured π^+ and π^- differential cross sections for ^{208}Pb for $\theta_p = 64°$

T_p (MeV)	σ^+	$\Delta\sigma^+$	σ^-	$\Delta\sigma^-$
35	193.94	6.48	185.95	8.61
45	770.22	13.94	543.11	14.50
55	767.14	13.89	508.86	13.92
65	685.25	13.23	409.72	12.50
75	593.52	12.29	374.68	12.09
85	509.17	11.20	286.68	10.53
95	423.58	10.50	210.63	9.03
105	355.25	9.45	166.04	7.82
115	264.74	7.92	122.24	6.62
125	252.43	8.08	120.64	6.67
135	135.45	5.88	60.92	4.70

TABLE V-4

Cross section ratios from singles data for ^{27}Al and ^{208}Pb

Target	θ_p	$R = \frac{\sigma(\pi^+,\pi p)}{\sigma(\pi^-,\pi p)}$
^{27}Al	55°	2.37 ± 0.2
	64°	1.95 ± 0.2
	90°	2.31 ± 0.2
^{208}Pb	45°	1.27 ± 0.1
	55°	1.47 ± 0.1
	64°	1.66 ± 0.2

D. COINCIDENCE DATA

$(\pi,\pi p)$ coincidence spectra and cross sections were obtained as follows: First, the status of bit #0 of the coincidence register was checked to determine whether a coincidence occurred between the proton arm and the pion arm. If a coincidence occurred, the identity of the particle in the proton arm was determined from the $E-\frac{dE}{dx}$ plots. Figure 30 displays the proton spectra from the $(\pi,\pi p)$ coincidence measurement on $^{27}A\ell$ for two different angular settings of the detector arms. The coincidence count rates were considerably less than those in the single-arm measurements. Because of the poor statistics, calculations of cross sections as functions of recoil proton energy were not made on the coincidence data. Instead, only the ratios of π^+ and π^- cross sections were determined.

Table V.5 summarizes the cross section ratios observed in the present measurement on $^{27}A\ell$ and ^{208}Pb for the angular settings $(\theta_p,\theta_\pi) = (55°,50°)$ and $(64°,37.5°)$. The value quoted for R for ^{12}C at $(\theta_p,\theta_\pi) = (55°,50°)$ is from a separate experiment[61] performed at LAMPF.

E. DISCUSSION OF RESULTS

The present measurements provide the first worthwhile coincidence data for the quasielastic scattering of fast pions by nuclei. The results obtained in the present study demonstrate three important points. The first one concerns the usefulness of studying the quasielastic

TABLE V-5

Cross Section ratios from coincidence data for ^{27}Al and ^{208}Pb for two angular settings

Target	θ_p, θ_π	$R = \frac{\sigma(\pi^+, \pi p)}{\sigma(\pi^-, \pi p)}$
^{27}Al	55°,50°	6.9 ± 0.7
	64°,37.5°	7.2 ± 0.7
^{208}Pb	55°,50°	4.6 ± 0.5
	64°,37.5°	4.5 ± 0.5
^{12}C	55°,50°	7.9 ± 1.0*

* Preliminary value obtained in a separate experiment[61].

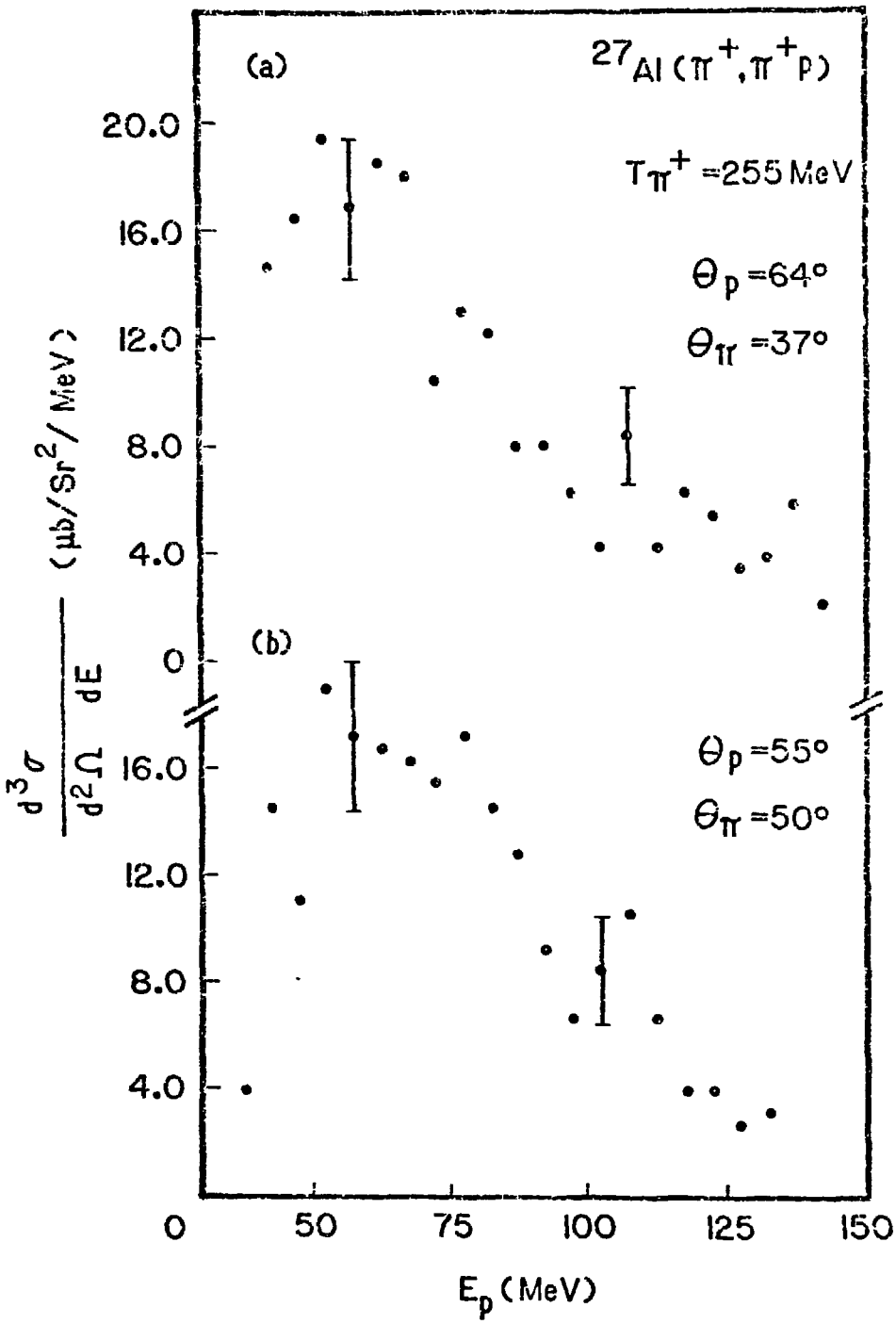

Fig. 30. Typical coincidence spectra.

pion scattering process in a single-arm experiment. As was mentioned in Chapter II, Silbar and Stupin[52] had hoped that a measurement of the recoil proton spectrum might yield valuable information on the gross features of quasielastic scattering. The present study indicates that this would be rather difficult. Comparison of the ratio of cross section values obtained from the singles and the coincidence data indicates that the singles spectra are contaminated by protons from events other than quasielastic scattering. This is further evidenced by the linear dependence of $\ln\sigma$ on E of the singles spectra, which indicates that these spectra are dominated by compound nuclear processes.

The second point concerns the validity of the impulse approximation in describing the quasielastic scattering of pions in the neighborhood of the (3,3) resonance. At T_π = 255 MeV, the incident pions are slightly above the peak of the resonance. However, the ratio of free particle $\pi^{\pm}p$ cross sections at this energy has only fallen to about 8. The $(\pi,\pi p)$ cross section ratio, $R = \frac{\sigma^+}{\sigma^-}$ as observed in the present experiment is less than this value for both ^{27}Al and ^{208}Pb. Thus, it is clear that the cross section ratios are significantly different from the impulse approximation, isospin-coupling and non-charge-exchange limit.

The third point concerns the relative importance of recoil nucleon charge exchange in the quasielastic pion scattering process. The cross section ratios observed in the present measurement and the ratio for ^{12}C Ensted[61], show a strong A-dependence, with R decreasing

with increasing A. Figures 31(a) and (b) display the variation of R with A for different proton momenta as expected from the semiclassical charge exchange model of Chapter III. The values measured in the present experiment are also displayed in the figures. It is seen that at P_p = 650 MeV/c, there is substantial agreement between the predictions of the model and the observed values. There is, however, a problem. The spectra observed in the experiment involved knockout protons of energy 20 MeV < E_p < 140 MeV. Thus, to a first approximation, the average momentum of the observed recoil protons is 365 MeV/c and this is much smaller than the value 650 MeV/c at which agreement is obtained between the charge exchange model predictions and the observed ratios. Nevertheless, the agreement noted above may be best interpreted as supporting the view that the recoil nucleon charge exchange plays an important role in the quasielastic knockout process.

F. CONCLUSION

The present study was aimed at providing a useful starting point in the study of quasielastic pion scattering, employing kinematically complete measurement of the reaction products. Additional studies, such as those planned by the University of Oregon - Oregon State University Medium Energy Nuclear Physics group using the EPICS spectrometer at LAMPF, will be needed to further advance the present knowledge of quasielastic pion scattering process.

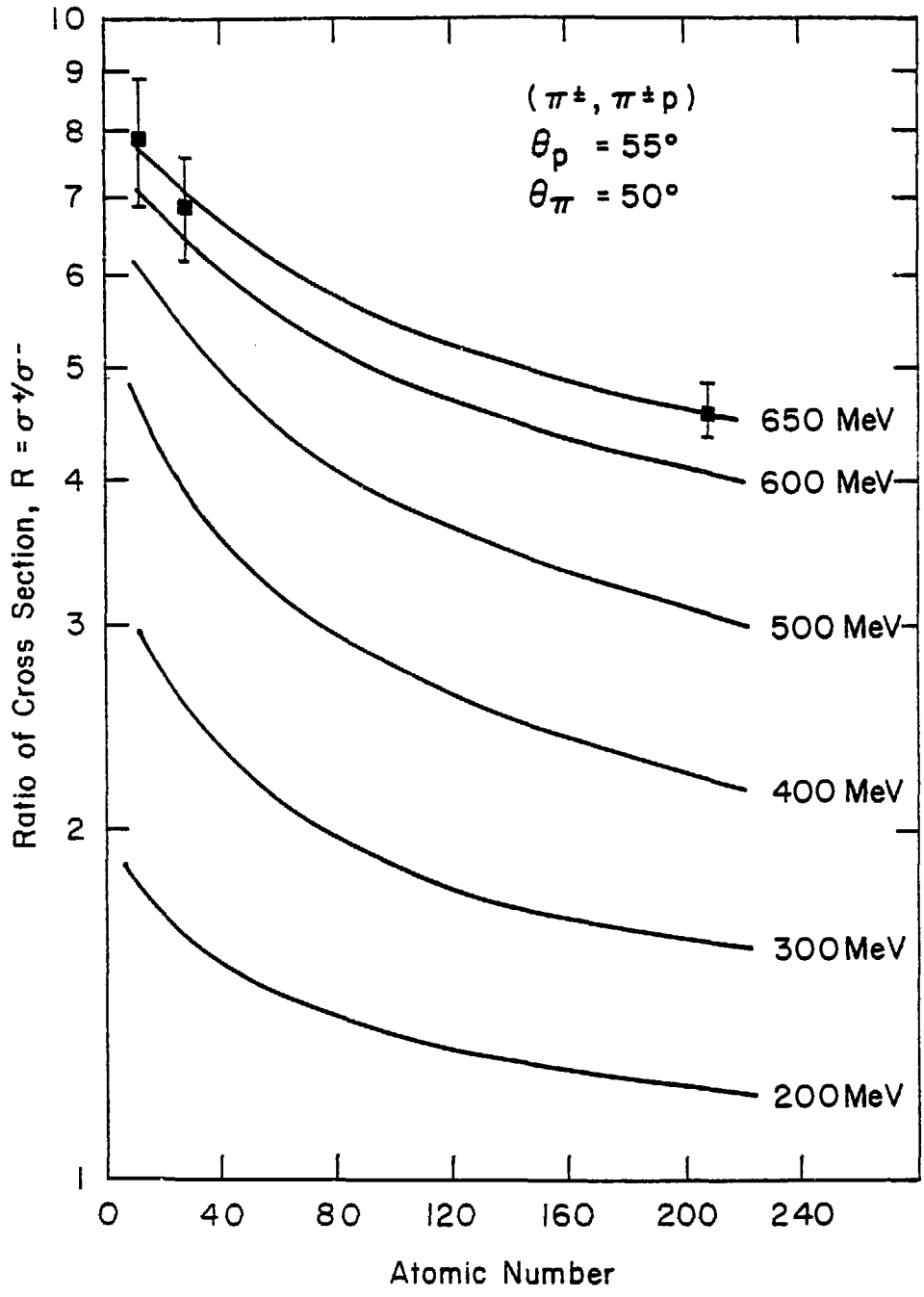

Fig. 31(a). Observed variation of $R = \frac{Q^+}{Q^-}$ with atomic number A for $\theta_p, \theta_\pi = 55°, 50°$. Solid curves represent values calculated from the semiclassical charge-exchange model.

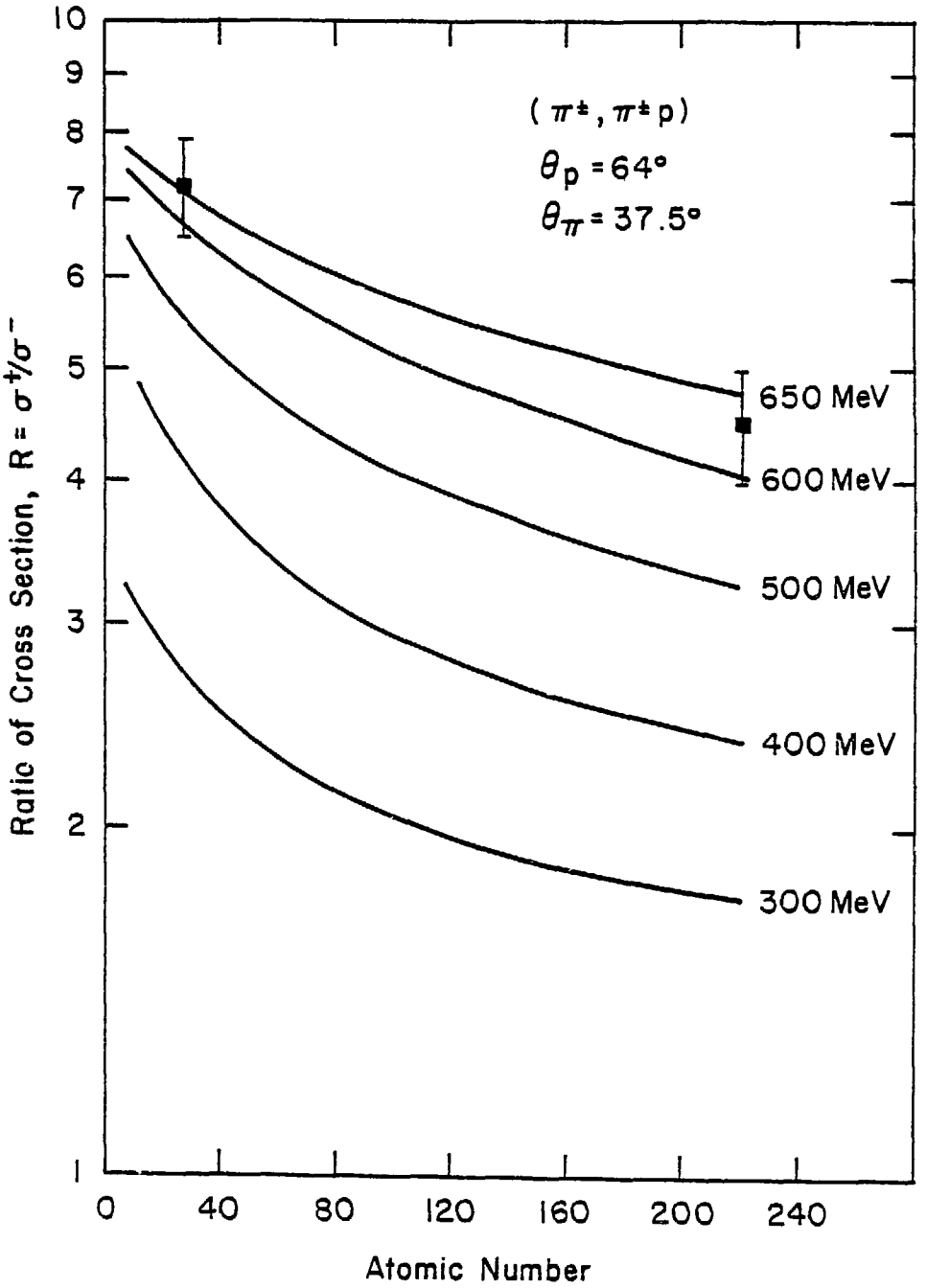

Fig. 31(b). Observed variation of $R = \frac{Q^+}{Q^-}$ with atomic number for $\theta_p, \theta_\pi = 64°, 37.5°$. Solid curves represent values calculated from the semiclassical charge-exchange model.

ACKNOWLEDGMENTS

I am greatly indebted to my thesis adviser, Professor David K. McDaniels for his guidance during the course of this study and I would like to take this opportunity to thank him profoundly for his suggestions and help. Thanks are also due to Professor L. W. Swenson, co-Chairman of my thesis committee, Dr. Richard R. Silbar and Dr. Tilak Sharma for their help and suggestions. It is a pleasure to acknowledge the many useful discussions with Dr. Noby Tanaka, Dr. H. A. Thiessen, Dr. M. E. Hamm, Dr. Charles Goulding, and Dr. M. A. Oothoudt. Personnel at the Clinton P. Anderson Meson Physics Facility have been extremely helpful during my research work at the Facility. Special thanks to Lilly Cordova for typing this thesis.

I am grateful to the USEFI and the IIE for awarding me the Fulbright Fellowship. Financial assistances from the NSF, LAMPF and AWU are gratefully acknowledged.

APPENDIX A

FREE PARTICLE PION NUCLEON CROSS SECTIONS

A. ELASTIC SCATTERING AND CHARGE EXCHANGE

Let σ_p^+ and σ_p^- be the cross sections for the elastic scattering processes,

$$\pi^+ + p \to \pi^+ + p$$

$$\pi^- + p \to \pi^- + p \ , \qquad \text{(A.1)}$$

respectively and let σ_p^0 be the cross section for the charge exchange process,

$$\pi^- + p \to \pi^0 + p \ . \qquad \text{(A.2)}$$

In view of isospin invariance, the scattering processes (A.1) and (A.2) can be described in terms of scattering matrices in isospin space.

Let $A(\frac{1}{2})$ and $M(\frac{1}{2})$ be respectively the scattering amplitude and the scattering matrix associated with the T=1/2 isospin state and $A(\frac{3}{2})$ and $M(\frac{3}{2})$ be those associated with the T=3/2 state. Then, since the scattering matrix is independent of T_z, using the results listed in Table I., the cross sections for the processes (A.1) and (A.2)

can be written as,

$$\sigma_p^+ \propto |\langle \pi^+ p | M | \pi^+ p \rangle|^2$$

$$\propto |\langle \tfrac{3}{2}, \tfrac{3}{2} | M(\tfrac{3}{2}) | \tfrac{3}{2}, \tfrac{3}{2} \rangle|^2$$

$$\propto |A(\tfrac{3}{2})|^2 \qquad \text{(A.3)}$$

$$\sigma_p^- \propto |\langle \pi^- p | M | \pi^- p \rangle|^2$$

$$\propto |\tfrac{1}{3} \langle \tfrac{3}{2}, \tfrac{-1}{2} | M(\tfrac{3}{2}) | \tfrac{3}{2}, \tfrac{-1}{2} \rangle + \tfrac{2}{3} \langle \tfrac{1}{2}, \tfrac{-1}{2} | M(\tfrac{1}{2}) | \tfrac{1}{2}, \tfrac{-1}{2} \rangle|^2$$

i.e. $$\sigma_p^- \propto \tfrac{1}{9} \left| A(\tfrac{3}{2}) + 2 A(\tfrac{1}{2}) \right|^2 \qquad \text{(A.4)}$$

$$\sigma_p^- \propto |\langle \pi^0 n | M | \pi^- p \rangle|^2$$

$$\propto |\tfrac{\sqrt{2}}{3} \langle \tfrac{3}{2}, \tfrac{-1}{2} | M(\tfrac{3}{2}) | \tfrac{3}{2}, \tfrac{-1}{2} \rangle - \tfrac{\sqrt{2}}{3} \langle \tfrac{1}{2}, \tfrac{-1}{2} | M(\tfrac{1}{2}) | \tfrac{1}{2}, \tfrac{-1}{2} \rangle|^2$$

$$\propto \tfrac{2}{9} \left| A(\tfrac{3}{2}) - A(\tfrac{1}{2}) \right|^2 \qquad \text{(A.5)}$$

In a similar way, it may be shown that for πn scattering, the cross sections for the elastic scattering processes,

$$\pi^+ + n \rightarrow \pi^+ + n$$

$$\pi^+ + n \rightarrow \pi^- + n \ ,$$

and the charge exchange process,

$$\pi^+ + n \rightarrow \pi^0 + p$$

are, respectively,

$$\sigma_n^+ \propto \frac{1}{9} \left| A(\tfrac{3}{2}) + 2\, A(\tfrac{1}{2}) \right|^2 \tag{A.6}$$

$$\sigma_n^- \propto \left| A(\tfrac{3}{2}) \right|^2 \tag{A.7}$$

$$\sigma_n^0 \propto \frac{2}{9} \left| A(\tfrac{1}{2}) - A(\tfrac{3}{2}) \right|^2 \tag{A.8}$$

B. TOTAL CROSS SECTIONS

Let A^0 and M^0 be respectively the scattering amplitude and scattering matrix at zero degree scattering angle. Then from the optical theorem, the total cross sections $\sigma_T^{\pm}$ for $\pi^{\pm}$ scattering are given by,

$$\sigma_T^+ = \frac{4\pi}{k} \operatorname{Im} \langle \pi^+ p | M^0 | \pi^+ p \rangle = \frac{4\pi}{k} \operatorname{Im} A^0(\tfrac{3}{2}) \tag{A.9}$$

$$\sigma_T^- = \frac{4\pi}{k} \operatorname{Im} \langle \pi^- p | M^0 | \pi^- p \rangle$$

$$= \frac{4\pi}{k} \left\{ \frac{1}{3} \operatorname{Im} A^0(\tfrac{3}{2}) + \frac{2}{3} \operatorname{Im} A^0(\tfrac{1}{2}) \right\} \tag{A.10}$$

Hence,

$$\sigma_T^- = \frac{1}{3} \sigma_T^+ + \frac{2}{3} \sigma_T(\tfrac{1}{2}) \tag{A.11}$$

where $\sigma_T(\frac{1}{2})$ is the total cross section for scattering in the pure T=1/2 state.

APPENDIX B

QUASIELASTIC $(\pi,\pi N)$ SCATTERING KINEMATICS

The calculations presented below apply to the experimental situation in which the energy and momentum of the recoil nucleon and the direction of the scattered pion are measured. It is assumed that the energy and direction of the incident pion beam are known and that the target nucleus is at rest. For convenience, the Z-axis is taken along the incident beam direction and the scattering plane is defined to be the plane containing the incident beam and the X-axis, i.e., the X-Z plane.

The following definitions are used in the calculations:

$$\gamma_i = 1 + T_i/m_i \ ,$$

$$\alpha_i = (\gamma_i^2 - 1)^{1/2} \ , \qquad \text{(B.1)}$$

where the subscript i denotes the particles involved:

$i = 0 \rightarrow$ incident pion,

$= 1 \rightarrow$ scattered pion,

$= 2 \rightarrow$ recoil nucleon,

$= 3 \rightarrow$ product nucleus;

The symbols T and m denote the kinetic energy and the mass of these particles. Thus,

$$E_i \equiv \gamma_i m_i \ ,$$

$$p_i \equiv \alpha_i m_i \qquad \text{(B.2)}$$

are respectively the total energy and the momentum of particle i. Since the target nucleus is at rest, in the impulse approximation, the momentum of the recoil nucleus is equal to the negative of the Fermi momentum of the struck nucleon; thus,

$$\vec{p}_3 = -\vec{q} \ . \qquad \text{(B.3)}$$

Let M_T be the mass of the target nucleus, E_B the binding energy per nucleon and E_x the excitation energy of the recoiling nucleus. Then, the four relativistic equations which express conservation of energy and momentum are:

Conservation of energy:

$$E_0 + M_T = \sum_{i=1}^{3} E_i + E_B + E_x \ ; \qquad \text{(B.4)}$$

Conservation of Z-momentum:

$$P_0 = \sum_{i=1}^{3} p_i \cos\theta_i \ ; \qquad \text{(B.5)}$$

Conservation of X-momentum:

$$0 = \sum_{i=1}^{3} p_i \sin\theta_i \cos\phi_i \ ; \qquad \text{(B.6)}$$

Conservation of Y-momentum:

$$0 = \sum_{i=1}^{3} p_i \sin\theta_i \sin\phi_i \; ; \tag{B.7}$$

One may eliminate ϕ_3 in Equations (B.6) and (B.7) by squaring and adding them; this gives,

$$p_3^2 \sin^2\theta_3 = p_1^2 \sin^2\theta_1 + p_2^2 \sin^2\theta_2 + 2\, p_1\, p_2 \sin\theta_1 \sin\theta_2 \cos(\phi_1-\phi_2). \tag{B.8}$$

If the ϕ-angles of the scattered pion and the recoil nucleon are the same, then the cosine term on the right-hand side of Equation (B.8) becomes equal to unity; it may be pointed out that such a condition is satisfied when the outgoing pion-nucleon pair is observed in the scattering plane, where,

$$\phi_1 = \phi_2 = 0$$

Under this condition, therefore,

$$p_3^2 \sin^2\theta_3 = p_1^2 \sin^2\theta_1 + p_2^2 \sin^2\theta_2 + 2\, p_1\, p_2 \sin\theta_1 \sin\theta_2 \; . \tag{B.9}$$

From Equation (B.5),

$$p_3^2 \cos^2\theta_3 = p_0^2 + p_1^2 \cos^2\theta_1 + p_2^2 \cos^2\theta_2 + 2\, p_1\, p_2 \cos\theta_1 \cos\theta_2 - 2\, p_0\, p_1 \cos\theta_1 - 2\, p_0\, p_2 \cos\theta_2 \; . \tag{B.10}$$

Adding Equations (B.9) and (B.10), one obtains,

$$p_3^2 = p_0^2 + p_1^2 + p_2^2 + 2\, p_1\, p_2 \cos(\theta_1-\theta_2)$$

$$- 2\, p_0\, p_1 \cos\theta_1 - 2\, p_0\, p_2 \cos\theta_2 \qquad \text{(B.11)}$$

In the above equation, p_0 is known while p_2, θ_1 and θ_2 are measured in the experiment; therefore,

$$Y = p_2 \cos(\theta_1-\theta_2) - p_0 \cos\theta_1 \ , \qquad \text{(B.12)}$$

and,

$$Z = p_0^2 + p_2^2 + m_3^2 - m_1^2 - 2\, p_0\, p_2 \cos\theta_2, \qquad \text{(B.13)}$$

are known quantities. In terms of these quantities, Equation (B.11) may be written as,

$$E_3^2 = E_1^2 + 2\, Y\, p_1 + Z, \qquad \text{(B.14)}$$

where the relations (B.1) and (B.2) have been employed to express the squares of p_1 and p_3 in terms of E_1 and E_3, respectively. Equation (B.4) may now be used to express E_3 in terms of E_1; let,

$$X = E_0 + M_T - (E_2 + E_B + E_x) \ . \qquad \text{(B.15)}$$

For known E_B and given E_x, X is a known quantity. Substituting this in Equation (B.4), one obtains, on squaring,

$$E_3^2 = E_1^2 - 2\, X\, E_1 + X^2 \ . \qquad \text{(B.16)}$$

Comparing this with Equation (B.14), it follows that

$$2\ Y\ p_1 = -\ 2\ X\ E_1 + X^2 - Z$$

On squaring this equation and employing once again, (B.1) and (B.2) to express p_1 in terms of E_1, one obtains the quadratic equation,

$$A\ E_1^{\ 2} + B\ E_1 + C = 0, \tag{B.17}$$

where,

$$A = X^2 - Y^2,$$

$$B = X\ (X^2 - Z),$$

$$C = [(X^2 - Z)^2 + 4\ Y^2\ m_1^{\ 2})/4. \tag{B.18}$$

Equation (B.17) has two possible solutions, given by,

$$E_1^{\pm} = [-B \pm (B^2 - 4\ A\ C)^{1/2}]/[2\ A]. \tag{B.19}$$

Corresponding to each of these two values, E_3 has a particular value. Therefore, one obtains two values for the Fermi momentum of the struck nucleon, which is equal but opposite in sign to p_3;

i.e., $$|q| = (E_3^{\ 2} - m_3^{\ 2})^{1/2} \tag{B.20}$$

Typical values of q are presented in Table B.1 for a range of values of observed proton momentum, for the $(\pi,\pi p)$ reaction on ^{208}Pb nucleus. It is seen that of the two values of q, the one corresponding to E_1^- is too large to be acceptable.

APPENDIX C

SOLUTION OF THE RECOIL NUCLEON TRANSPORT EQUATIONS

The matrix form of the transport equations is:

$$\begin{pmatrix} N_1' \\ N_2' \end{pmatrix} = \rho B \begin{pmatrix} N_1 \\ N2 \end{pmatrix} \tag{C.1}$$

where

$$B = \begin{pmatrix} -(\lambda_a^{-1} + \lambda_n^{-1}) & \lambda_p^{-1} \\ \lambda_n^{-1} & -(\lambda_a^{-1} + \lambda_p^{-1}) \end{pmatrix} \tag{C.2}$$

Equation (C.1) is of the form,

$$N' = \frac{dN}{ds} = A\,N(s) \tag{C.3}$$

where N and N' are the column vectors,

$$N' = \begin{pmatrix} N_1' \\ N_2' \end{pmatrix}$$

$$N = \begin{pmatrix} N_1 \\ N_2 \end{pmatrix} \tag{C.4}$$

and,

$$A = \rho B \tag{C.5}$$

is a square matrix of order 2. (n-1) differentiations of Equation (C.3) yield,

$$\frac{d^n N}{ds^n} = A^n N(s) \tag{C.6}$$

Consider the expansion of N(s) in a Taylor series about s = 0:

$$N(s) = N(o) + \frac{s}{1!}\frac{dN}{ds}\Big|_{s=0} + \frac{s^2}{2!}\frac{d^2N}{ds^2}\Big|_{s=0} + - - . \tag{C.7}$$

In view of (C.6), then

$$N(s) = \left(1 + \frac{As}{1!} + \frac{A^2s^2}{2!} + . . .\right) N(o)$$

or,

$$N(s) = e^{As} N(o) \tag{C.8}$$

Let S_i be a complete set of eigen-columns of A with eigenvalues λ_i^{-1}:

$$AS_i = \lambda_i^{-1} S_i \tag{C.9}$$

Then, N(o) may be expanded in terms of S_i as

$$N(o) = \sum_i a_i S_i \tag{C.10}$$

$$N(s) = \sum_i e^{As} a_i S_i$$

$$= \sum_i e^{\lambda_i^{-1} S} a_i S_i \tag{C.11}$$

Here, $A = \rho B$ is not a diagonal matrix; however one can represent (C.11) in terms of a diagonal matrix $\tilde{A}$ defined by

$$A = \rho\tilde{B} = S^{-1}AS = \rho S^{-1}BS \tag{C.12}$$

Hence,

$$AS = S\tilde{A} \tag{C.13}$$

and

$$F(A)S = Sf(\tilde{A})$$

Now

$$f(A) = f(A)I$$

$$= f(A)SS^{-1}$$

$$f(A) = Sf(\tilde{A})S^{-1} \tag{C.14}$$

Then

$$N(\delta) = e^{As}\, N(o)$$

$$= S\, e^{\tilde{A}s}\, S^{-1}\, N(o) \tag{C.15}$$

or

$$N_i(S) = \sum_k S_{ik}\, e^{\tilde{A}_{kk}s}\, (S^{-1})_{kj}\, N(o)\ . \tag{C.16}$$

Since

$$[f(\tilde{A})]_{ij} = [f(A)]_{ij}\, \delta_{ij}\ , \tag{C.17}$$

$$N_i(s) = \sum_i S_{ik}\, e^{\tilde{B}_{kk}\rho s}\, (S^{-1})_{ij}\, N_j(o)\,. \tag{C.18}$$

Now, at the surface of the nucleus,

$$x = d_N = r \cos\theta_{r,N} \ . \tag{C.19}$$

Thus, the number of nucleons leaving the nucleus in charge state i is given by

$$N_i(d_N) = \sum_j S_{ik} \, e^{\tilde{B}_{kk}\rho d_N} \, (S^{-1})_{kj} \, N_j(o) \tag{C.20}$$

In the above equation d_N is the geometric path length of the nucleon. Calculations of N_i become simpler by replacing ρd_N in (C.20) by $\rho_o R$ where R, defined to be

$$R(r) = \frac{1}{\rho_o} \int_o^\infty \rho(\vec{r} + \hat{k}'s) \, ds \tag{C.21}$$

is the effective nucleon path length.

Writing,

$$M_{ij} = S_{ik} \, e^{\tilde{B}_{kk}R} \, (S^{-1})_{kj} \tag{C.22}$$

the solutions (C.20) become

$$N_i(\vec{r}) = \sum_j M_{ij} \, N_j(o) \ .$$

APPENDIX D

EVALUATION OF M_{ij}'s

From equation (C.12), the diagonal matrix B is given by,

$$\tilde{B} = S^{-1}BS \tag{D.1}$$

The matrix S which diagonalizes B is determined by the characteristic equation

$$|B-DI| = o \tag{D.2}$$

i.e.,
$$\begin{vmatrix} -(D_a + D_n) - D & D_p \\ D_n & -(D_a + D_p) - D \end{vmatrix} = o \tag{D.2}$$

where D's have been used to replace λ^{-1}'s.

This yields

$$[(D_a + D) + D_n][(D_a + D) + D_p] - D_pD_n = o \tag{D.3}$$

The characteristic roots are then,

$$D_1 = -D_a$$

$$D_2 = -(D_a + D_p + D_n) \tag{D.4}$$

Let $\vec{S}_1$ and $\vec{S}_2$ be the column vectors corresponding to D_1 and D_2:

Then

$$(B - D_1 I)\, S_1 = o$$

$$(B - D_2 I)\, S_2 = o \qquad \text{(D.5)}$$

These yield

$$\vec{S}_1 = \begin{pmatrix} \dfrac{D_p}{\sqrt{D_p^{\,2} + D_n^{\,2}}} \\ \dfrac{D_n}{\sqrt{d_p^{\,2} + D_n^{\,2}}} \end{pmatrix}$$

and

$$\vec{S}_2 = \begin{pmatrix} -\dfrac{1}{\sqrt{2}} \\ \dfrac{1}{\sqrt{2}} \end{pmatrix} \qquad \text{(D.6)}$$

Hence, the diagonalizing matrix S is given by

$$S = \begin{matrix} \dfrac{D_p}{\sqrt{D_p^{\,2} + D_n^{\,2}}} & -\dfrac{1}{\sqrt{2}} \\ \dfrac{D_n}{\sqrt{D_p^{\,2} + D_n^{\,2}}} & \dfrac{1}{\sqrt{2}} \end{matrix} \qquad \text{(D.7)}$$

Now,

$$S^{-1} = \frac{1}{\mathrm{Det}(S)} \begin{pmatrix} S_{22} & -S_{12} \\ -S_{21} & S_{11} \end{pmatrix} \tag{D.8}$$

$$S^{-1} = \begin{matrix} \dfrac{\sqrt{Dp^2 + D_n^2}}{D_p + D_n} & \dfrac{\sqrt{D_p^2 + D_n^2}}{D_p + D_n} \\ \dfrac{-\sqrt{2}\, D_n}{D_p + D_n} & \dfrac{\sqrt{2}\, D_p}{D_p + D_n} \end{matrix} \tag{D.9}$$

From the characteristic roots,

$$\tilde{B} = S^{-1} B S$$

$$= \begin{pmatrix} -D_a & o \\ o & -(D_a + D_n + D_p) \end{pmatrix} \tag{D.10}$$

Now, by definition

$$M_{ij} = S_{ik}\, e^{\tilde{B}_{kk} R}\, (S^{-1})_{kj} \tag{D.11}$$

Thus

$$M_{11} = S_{11}\, e^{\tilde{B}_{11}R}\, (S^{-1})_{11} + S_{12}\, e^{\tilde{B}_{22}R}\, (S^{-1})_{21}$$

$$= \frac{D_p}{\sqrt{D_p^{\,2} + D_n^{\,2}}}\, e^{-D_a R}\, \frac{\sqrt{D_p^{\,2} + D_n^{\,2}}}{D_p + D_n}$$

$$+ \; -\frac{1}{\sqrt{2}}\, e^{-(D_a+D_n+D_p)}\, \frac{-\sqrt{2}\, D_n}{D_p + D_n}$$

i.e.,

$$M_{11} = \frac{D_p}{D_p + D_n}\, e^{-D_a R} + \frac{D_n}{D_p + D_n}\, e^{-(D_a+D_n+D_p)R} \qquad \text{(D.12)}$$

Similarly

$$M_{12} = \frac{D_p}{D_p + D_n}\, e^{-D_a R} - \frac{D_p}{D_p + D_n}\, e^{-(D_a+D_n+D_p)R} \qquad \text{(D.13)}$$

$$M_{21} = \frac{D_n}{D_p + D_n}\, e^{-D_a R} - \frac{D_n}{D_p + D_n}\, e^{-(D_a+D_n+D_p)R} \qquad \text{(D.14)}$$

$$M_{22} = \frac{D_n}{D_p + D_n}\, e^{-D_a R} + \frac{D_p}{D_p + D_n}\, e^{-(D_a+D_n+D_p)R} \qquad \text{(D.15)}$$

Remembering that (cf. Equations III.12)

$$D_a = \lambda_a^{-1} = A\,\sigma_{N,abs} \ ,$$

$$D_p = \lambda_p^{-1} = Z\,\sigma_{N,ex} \ ,$$

$$D_n = \lambda_n^{-1} = N\,\sigma_{N,ex} \ , \qquad \text{(D.16)}$$

Equations (D.12), (D.13), (D.14), and (D.15) can be reduced to the form,

$$M_{11} = \frac{e^{-\alpha R}}{A}\left(Z + N\,e^{-\beta R}\right)$$

$$M_{12} = \frac{e^{-\alpha R}}{A}\left(Z - Z\,e^{-\beta R}\right)$$

$$M_{21} = \frac{e^{-\alpha R}}{A}\left(N - N\,e^{-\beta R}\right)$$

$$M_{22} = \frac{e^{-\alpha R}}{A}\left(N + Z\,e^{-\beta R}\right) \qquad \text{(D.17)}$$

where

$$\alpha = A\,\sigma_{N,abs}$$

$$\beta = A\,\sigma_{N,ex} \ . \qquad \text{(D.18)}$$

APPENDIX E

QUASEX-

PROGRAM LISTING

A listing of the FORTRAN program QUASEX is given.

LASL Identification number: LP-1012

```
      PROGRAM QUASEX(INPUT,OUTPUT)
C
C     CALCULATES QUASI-ELASTIC CROSS SECTION WHEN OUTGOING PROTON IS
C     OBSERVED. CHARGE EXCHANGE PROCESSES INCLUDED.
C     WOODS-SAXON DENSITY.  CALCULATES S AND P AS FUNCTION OF SIGABS
C     PION ABSORPTION PROPORTIONAL TO RHO SQUARED.
C
C     INPUT DECK AS FOLLOWS ---
C     CARD 1. FORMAT (3F10.5).  TPI, SIGMA(PI+,P), SIGMA(PI-,P).
C     CARD 2. FORMAT(6F10.5).  THETA, TPR(RECOIL PROTON K.E.),
C         SIGMA(P,P), SIGMA(P,N),BETAN,SIGMA(ISO)
C     CARD 3. FORMAT (5F10.5).  ANUM, ZNUM, XI, RHLF, ATHK.
C     CARD 4. FORMAT (4I5).  NEPTS, NZPTS, NPHISS0, NSPTS, IPNCH.  IF
C          IPNCH = 0 (OR IS BLANK), NO PUNCHED OUTPUT.
C
      COMMON ANUM,ZNUM,ANUM,RHOZRO,RHLF,ATHK,NSPTS,DELS,RSQ
      REAL NNUM
      REAL LSCTPL, LSCTMI, LABSPL, LABSMI
      DIMENSION XPL(2,4),XMI(2,4),XZPL(2,4),XZMI(2,4)
      DIMENSION CPHI(20),BSTHCPH(20),BPISTCP(20)
      DIMENSION YPHIP(2,4),YPHIN(2,4)
      DIMENSION LABSPL(4), LABSMI(4)
      DIMENSION SIGABS(4), ALPHABS(4), RATIO(4)
C
      PI = 3.14159265359
      XMP=938.232
      XMPSQ=XMP*XMP
      IPRINT = 0
C
   10 READ 1000, TPI,SIGPIP,SIGPIM
      PRINT 2110, TPI,SIGPIP,SIGPIM
C
   20 CONTINUE
      READ 1000,THETA,TPI
C
  100 READ 1000, ANUM, ZNUM, XI, RHLF, ATHK
      RHOZRO = (3.*ANUM)/(4.*PI*RHLF**3)
      X = ATHK/RHLF
      ERKTS = 1. + (PI*X)**2 + 2.*X**3/EXP(1./X)
      RHOZRO = RHOZRO/ERKTS
      PRINT 1010, ANUM, ZNUM, XI, RHLF, ATHK, RHOZRO
C
      ANUM = ANUM - ZNUM
      SIGPIL = (ZNUM*SIGPIP + NNUM*SIGPIM)/ANUM
      SIGPIMI = (ZNUM*SIGPIM + NNUM*SIGPIP)/ANUM
C
C     ALL MEAN FREE PATH LENGTHS ARE IN FERMIS, AS ARE NUCLEAR RADIUS,
C          THICKNESS, ETC.
C
      LSCTPL = 10./(RHOZRO*SIGPIPL)
      LSCTMI = 10./(RHOZRO*SIGPIMI)
      IF(IPRINT.NE.0) GO TO 105
      PRINT 2130, LSCTPL,LSCTMI
  105 CONTINUE
C
      FABSPL = (NNUM*ZNUM + XI*NNUM**2)/ANUM**2
      FABSMI = (NNUM*ZNUM + XI*ZNUM**2)/ANUM**2
      DO 107 IL1 = 1,4
      SIGABS(IL1) =10.*IL1
```

```
      ALPHABS(IL1) = (4./(1.+XI))*SIGABS(IL1)/(10.*RHOZRO)
C
C     SIGABS IS IN MB, ALPHABS ALREADY IN FM**-1
C
      LABSPL(IL1) = 1./(FABSPL*RHOZRO**2 + ALPHABS(IL1))
      LABSMI(IL1) = 1./(FABSMI*RHOZRO**2 + ALPHABS(IL1))
  107 CONTINUE
C
      IF(IPRINT.NE.0) GO TO 109
      PRINT 9010, SIGABS, ALPHABS
      PRINT 9020, LABSPL,LABSMI
  109 CONTINUE
      PRINT 1015,THETA,THPI
C
  110 READ 1001, NRPTS, NZPTS, NPHI, NSPTS, IPNCH
      IF (NPHI .GT. 50) NPHI = 50
      IF(IPRINT.NE.0) GO TO 112
      PRINT 1020, NRPTS, NZPTS, NPHI, NSPTS
  112 CONTINUE
C
      RMAX = RHLF + 5.*ATHK
      DELR = RMAX/NRPTS
      DELPHI = 2.*PI/NPHI
      DELS = 2.*RMAX/NSPTS
      TEMPRO = RHOZRO*DELR*DELPHI
      TEMPRO = TEMPRO /ANUM
C
      BETN=70620.
  115 CONTINUE
      READ 1002,NEWLIM
      DO 600 NEW=1,NEWLIM
      READ 1000,PPP,SIGPP,SIGPN,TFISC,SPIPL,SPIMI
      EPR=PPP*PPP+XMPSQ
      TPROT=SQRT(EPR)-XMP
      SIGNUC = (ZNUM*SIGPP + NNUM*SIGPN)/ANUM
      SIGNEX=BETN*(TPROT**(-1.5))
      RPIPL=(ZNUM*SPIPL+NNUM*SPIMI)/ANUM
      RPIMI=(ZNUM*SPIMI+NNUM*SPIPL)/ANUM
      PRINT 2120, PPP,TPROT,SIGPP,SIGPN,SIGNEX
      PRINT 2125,TFISC,SPIPL,SPIMI,RPIPL,RPIMI
      EPSIP=RHOZRO*RPIPL/10.
      EPSIN=RHOZRO*RPIMI/10.
      ALFA=SIGNUC*RHOZRO/10.
      BETA=SIGNEX*RHOZRO/10.
      PHI = -DELPHI/2.
      DO 120 I = 1, NPHI
      PHI = PHI + DELPHI
      CPHI(I) = COS(PHI)
  120 CONTINUE
C
C
C     NEST OF LOOPS.  R, Z, AND PHI -- ON THE OUTSIDE.  AFTER THE
C     PATH LENGTHS C AND E ARE CALCULATED THERE ARE SECONDARY INTERNAL
C     LOOPS TO STORE RESULTS FOR DIFFERENT SIGABS IN THE X-ARRAYS.
C
      DO 130 J=1,2
      DO 130 IABS = 1,4
      XPL(J,IABS)=0.
      XMI(J,IABS)=0.
  130 CONTINUE
```

```
C
      PANG=THETA*PI/180.
      PIANG=THPI*PI/180.
      STH=SIN(PANG)
      CTH=COS(PANG)
      STHPI=SIN(PIANG)
      CTHPI=COS(PIANG)
C
C
      B = -DELB/2.
      NO=1
      NP=2
      DO 500 IB = 1, NBPTS
      B = B + DELB
      DO 200 I = 1, NPHI
      BPISTCP(I)=B*STHPI*CPHI(I)
  200 BSTHCPH(I) = B*STH*CPHI(I)
      BSQ = B*B
      ZLIM = SQRT(RMAX**2 - BSQ)
      DELZ = 2.*ZLIM/NZPTS
      Z = -ZLIM - DELZ/2.
      DO 210 J=1,2
      DO 210 IABS = 1,4
      XZPL(J,IABS)=0.
      XZMI(J,IABS)=0.
  210 CONTINUE
C
      DO 400 IZ = 1, NZPTS
      Z = Z + DELZ
      RSQ = BSQ + Z*Z
      DNSTY = RHO(SQRT(RSQ))
      ZCTH = Z*CTH
      ZPICTH=Z*CTHPI
C
      DO 220 JABS=1,4
      DO 220 NN=1,2
      YPHIP(NN,JABS)=0.
      YPHIP(NN,JABS)=0.
  220 CONTINUE
      DO 300 IPHI = 1, NPHI
      EL2 = BSTHCPH(IPHI) + ZCTH
      CALL PATH(EL2,D2,E2)
      ALFACP=ALFA*D2
      BETACP=BETA*D2
      EM1=ZNUM*ANUM*EXP(-BETACP)
      EM2=1.-EXP(-BETACP)
      EM11=EM1*EXP(-ALFACP)/ANUM
      EM12=EM2*ZNUM*EXP(-ALFACP)/ANUM
      EL3=BPISTCP(IPHI)+ZPICTH
      CALL PATH(EL3,D3,E3)
      YP1=D3*EPSIP
      YM1=D3*EPSIM
      DO 250 IABS=1,4
      YP2=E3/LABSPL(IABS)
      YM2=E3/LABSMI(IABS)
      YP=EXP(-YP1-YP2)
      YM=EXP(-YM1-YM2)
      YPHIP(NO,IABS)=YPHIP(NO,IABS)+EM11*YP
      YPHIP(NP,IABS)=YPHIP(NP,IABS)+EM12*YP
      YPHIM(NO,IABS)=YPHIM(NO,IABS)+EM11*YM
```

```
      YPHIM(NP,IABS)=YPHIM(NP,IABS)+EM12*YM
  250 CONTINUE
  300 CONTINUE
C
C     ENDS PHI LOOP
C
      EL1 = -Z
      CALL PATH (EL1,D1,E1)
      TSCTPL = D1/LSCTPL
      TSCTMI = D1/LSCTMI
      DO 350 IABS = 1,4
      TABSPL = E1/LABSPL(IABS)
      TABSMI = E1/LABSMI(IABS)
      XABSAPL = EXP(-TSCTPL-TABSPL)
      XABSAMI = EXP(-TSCTMI-TABSMI)
      XABSAPL = DNSTY*XABSAPL
      XABSAMI = DNSTY*XABSAMI
      XZPL(NQ,IABS)=XZPL(NQ,IABS)+XABSAPL*YPHIP(NQ,IABS)
      XZPL(NP,IABS)=XZPL(NP,IABS)+XABSAPL*YPHIP(NP,IABS)
      XZMI(NQ,IABS)=XZMI(NQ,IABS)+XABSAMI*YPHIM(NQ,IABS)
      XZMI(NP,IABS)=XZMI(NP,IABS)+XABSAMI*YPHIM(NP,IABS)
  350 CONTINUE
  400 CONTINUE
C
C     ENDS Z LOOP
C
      TEMPB = B*DEL2
      DO 480 IABS = 1,4
      XPL(NQ,IABS)=XPL(NQ,IABS)+TEMPB *XZPL(NQ,IABS)
      XPL(NP,IABS)=XPL(NP,IABS)+TEMPB *XZPL(NP,IABS)
      XMI(NQ,IABS)=XMI(NQ,IABS)+TEMPB *XZMI(NQ,IABS)
      XMI(NP,IABS)=XMI(NP,IABS)+TEMPB *XZMI(NP,IABS)
  480 CONTINUE
  500 CONTINUE
C
C     ENDS B LOOP
C
C
      DO 580 IABS = 1,4
      XPL(NQ,IABS)=XPL(NQ,IABS)*TEMPNQ
      XPL(NP,IABS)=XPL(NP,IABS)*TEMPNQ
      XMI(NQ,IABS)=XMI(NQ,IABS)*TEMPNQ
      XMI(NP,IABS)=XMI(NP,IABS)*TEMPNQ
      CMINS=ZNUM*XMI(NQ,IABS)+S.*ANUM*XMI(NP,IABS)
      CPLUS=S.*ZNUM*XPL(NQ,IABS)+ANUM*XPL(NP,IABS)
      RATIO(IABS)=CPLUS/CMINS
  580 CONTINUE
C
C
C     PRINT OUT
C
      PRINT 3010, SIGABS
      PRINT 3030, (XPL(NQ,IABS),IABS=1,4)
      PRINT 3035, (XPL(NP,IABS),IABS=1,4)
      PRINT 3040, (XMI(NQ,IABS),IABS=1,4)
      PRINT 3045, (XMI(NP,IABS),IABS=1,4)
      PRINT 3050,RATIO
  600 CONTINUE
      PRINT 3000, D1,D2,D3
      IPRINT = 1
```

```
C
 800  CONTINUE
C
      READ 1002,NCHOIZ
C
C     NCHOIZ=1 - NEW PION ENERGY
C     NCHOIZ=2 - NEW PROTON ANGLE AND ENERGY, SAME T(PI)
C     NCHOIZ=3 - NEW  TARGET, SAME T(PI)
C     NCHOIZ=4 - SAME TARGET,T(PI),T(P) BUT NEW NBPTS
C
      IF(NCHOIZ.EQ.4) GO TO 110
      IF(NCHOIZ.EQ.3) GO TO 100
      IF(NCHOIZ.EQ.2) GO TO 20
      IF(NCHOIZ.EQ.1) GO TO 10
C
C
 1000 FORMAT (6F10.5)
 1001 FORMAT (5I5)
 1002 FORMAT(I2)
 1010 FORMAT (//1H0,7HANUM = ,F5.0,8X,7HZNUM = ,F5.0,8X,6HXI    = ,F5.3,
     1     7X,7HSHELF = ,F8.3,5X,7HATHA = ,F8.3,5X,9HRHOZRO = ,F10.7)
 1015 FORMAT(//1H0,8HTHETA = ,F7.2,5X*1HETAPI =*F7.2)
 1020 FORMAT (//1H0,8HNBPTS = ,I4,8X,8HNZPTS = ,I4,8X,7HNPHI = ,I4,9X,
     1     8HNSPTS = ,I4)
 2110 FORMAT (1H0,8HTPI =    ,F8.3,4X,8HSIGPIP =,F10.5,2X,8HSIGPIM =,
     1     F10.5,2X)
 2120 FORMAT (1H0,8HPPROT = ,F8.3,4X,8HTPN =    ,F10.5,2X,8HSIGPP = ,
     1F10.5,2X,8HSIGPN = ,F10.5,2X,8HSIGNEX =,F10.5)
 2125 FORMAT(1H0,*SCATTERED PION KE =*F8.3,//6X,*PI+ AND PI- CROSS *,
     1 *SECTIONS ARE - *,2F8.3,5X*RPIPL/MI =*2F8.3)
 2130 FORMAT (1H0,8HLSCTPL =,F10.5,2X,8HLSCTMI =,F10.5)
 2160 FORMAT(1H0,*BETA=0. CALLING EXIT*)
 3000 FORMAT (1H0,25X,6HCPI = ,F8.5,7X,5HCP = ,F8.5,7X*CSPI =*F8.5)
 3010 FORMAT (1H0,20X,9HSIGABS = ,4X,F9.2,7F12.2)
 3030 FORMAT(1H0,20X*GPL = *4X,8F12.5)
 3035 FORMAT(1H0,20X*PPL = *4X,8F12.5)
 3040 FORMAT(1H0,20X*QMI = *4X,8F12.5)
 3045 FORMAT(1H0,20X*PMI = *4X,8F12.5)
 3050 FORMAT(1H0,18X*RATIO = *4X,8F12.5)
 4000 FORMAT(5X,5F10.5,4I5)
 4010 FORMAT (3HXPL,3F9.5)
 4011 FORMAT (3HXMI,8F9.5)
 5010 FORMAT (1H0,*SIGABS *,4F10.5,/,1H0,*ALPHABS*,4F10.5)
 5020 FORMAT (1H0,*LABSPL *,4F10.5,/1H0,*LABSMI *,4F10.5)
 5050 FORMAT(3I4,4F12.5)
      STOP
      END
```

```
      SUBROUTINE PATH(EL,D,E)
      COMMON ANUM,ZNUM,RNUM,RHOZRC,RHLF,ATHK,NSPTS,DELS,RSC
      S = -DELS/2.
      D = 0.
      E = 0.
      DO 100 I = 1,NSPTS
      S = S + DELS
      RPR = SQRT(RSC + S*S + 2.*EL*S)
      DNSTY = RHO(RPR)
      IF (DNSTY .LT. 0.0001) GO TO 150
      D = D + DNSTY
      E = E + DNSTY*(ENSTY
  100 CONTINUE
  150 D = DELS*D
      E = DELS*E
      RETURN
      END
```

```
      FUNCTION RHO(RPR)
      COMMON ANUM,ZNUM,RNUM,RHOZRC,RHLF,ATHK,NSPTS,DELS,RSC
      RHO = 1./(1. + EXP((RPR-RHLF)/ATHK))
      RETURN
      END
```

APPENDIX F

FLOW CHART OF CAREAD

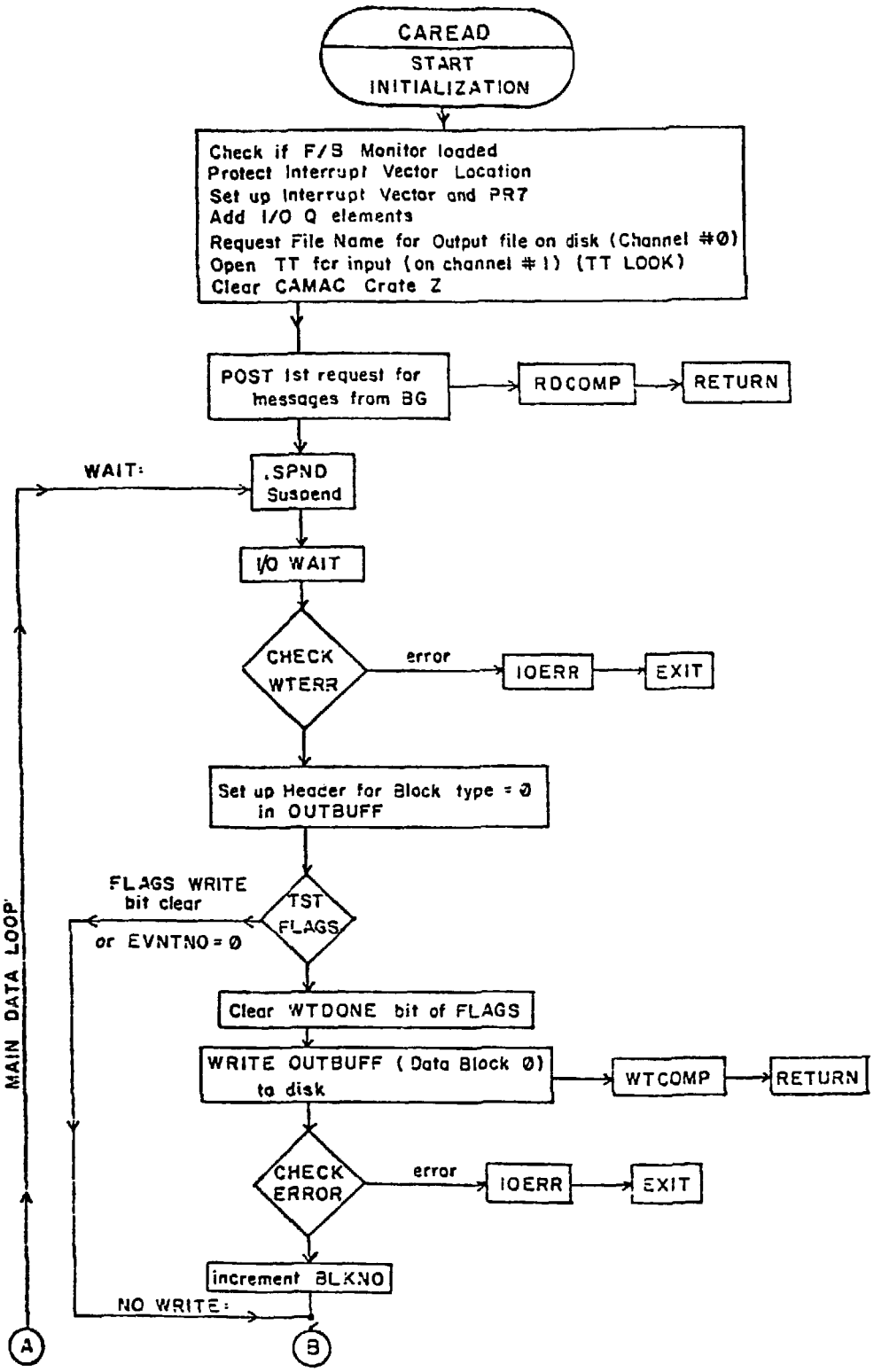

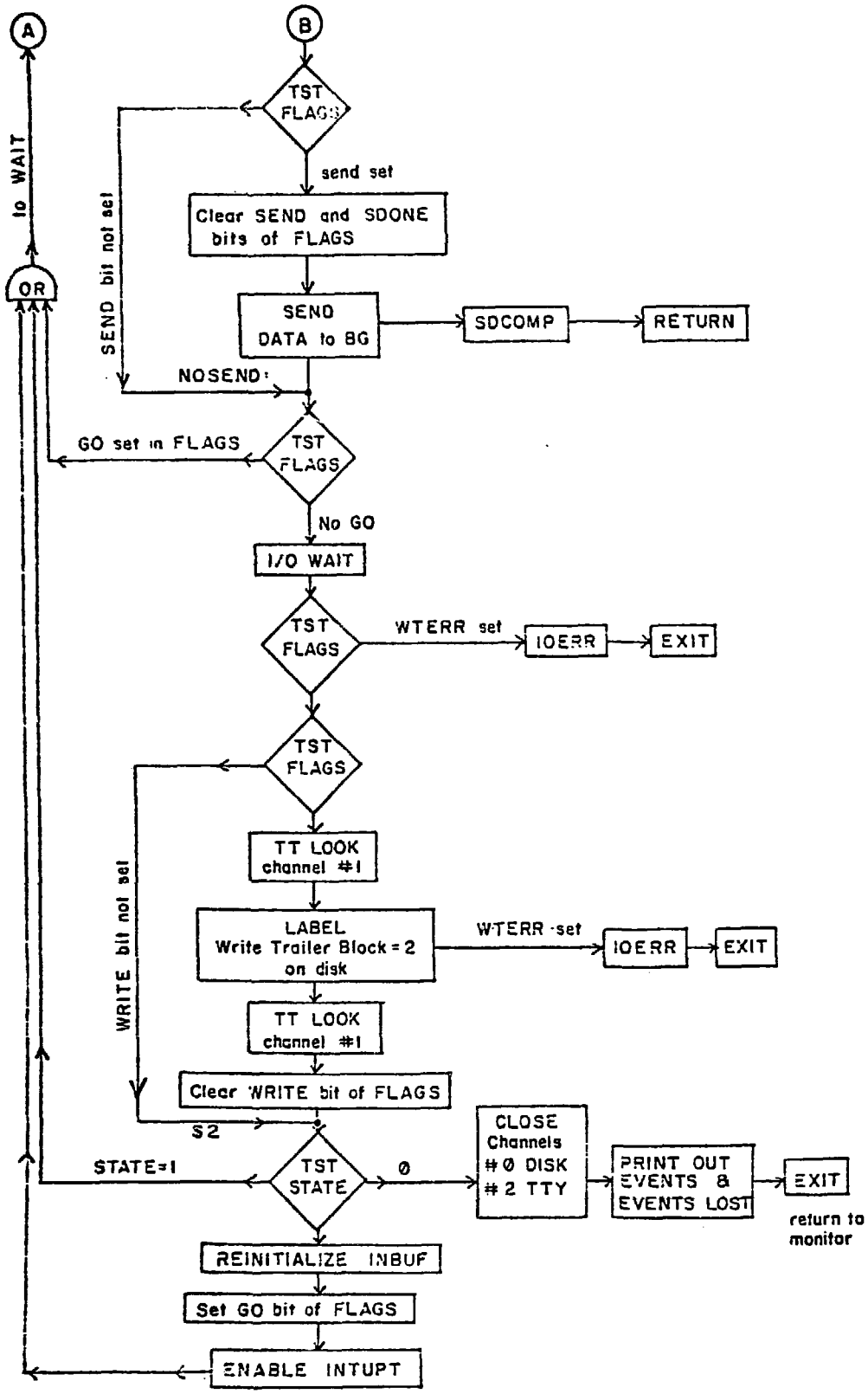
A
B
to WAIT
OR
TST FLAGS
send set
Clear SEND and SDONE bits of FLAGS
SEND bit not set
SEND DATA to BG
SDCOMP
RETURN
NOSEND:
GO set in FLAGS
TST FLAGS
No GO
I/O WAIT
TST FLAGS
WTERR set
IOERR
EXIT
TST FLAGS
WRITE bit not set
TT LOOK channel #1
LABEL Write Trailer Block = 2 on disk
WTERR set
IOERR
EXIT
TT LOOK channel #1
Clear WRITE bit of FLAGS
S2
STATE=1
TST STATE
0
CLOSE Channels # 0 DISK # 2 TTY
PRINT OUT EVENTS & EVENTS LOST
EXIT
return to monitor
REINITIALIZE INBUF
Set GO bit of FLAGS
ENABLE INTUPT

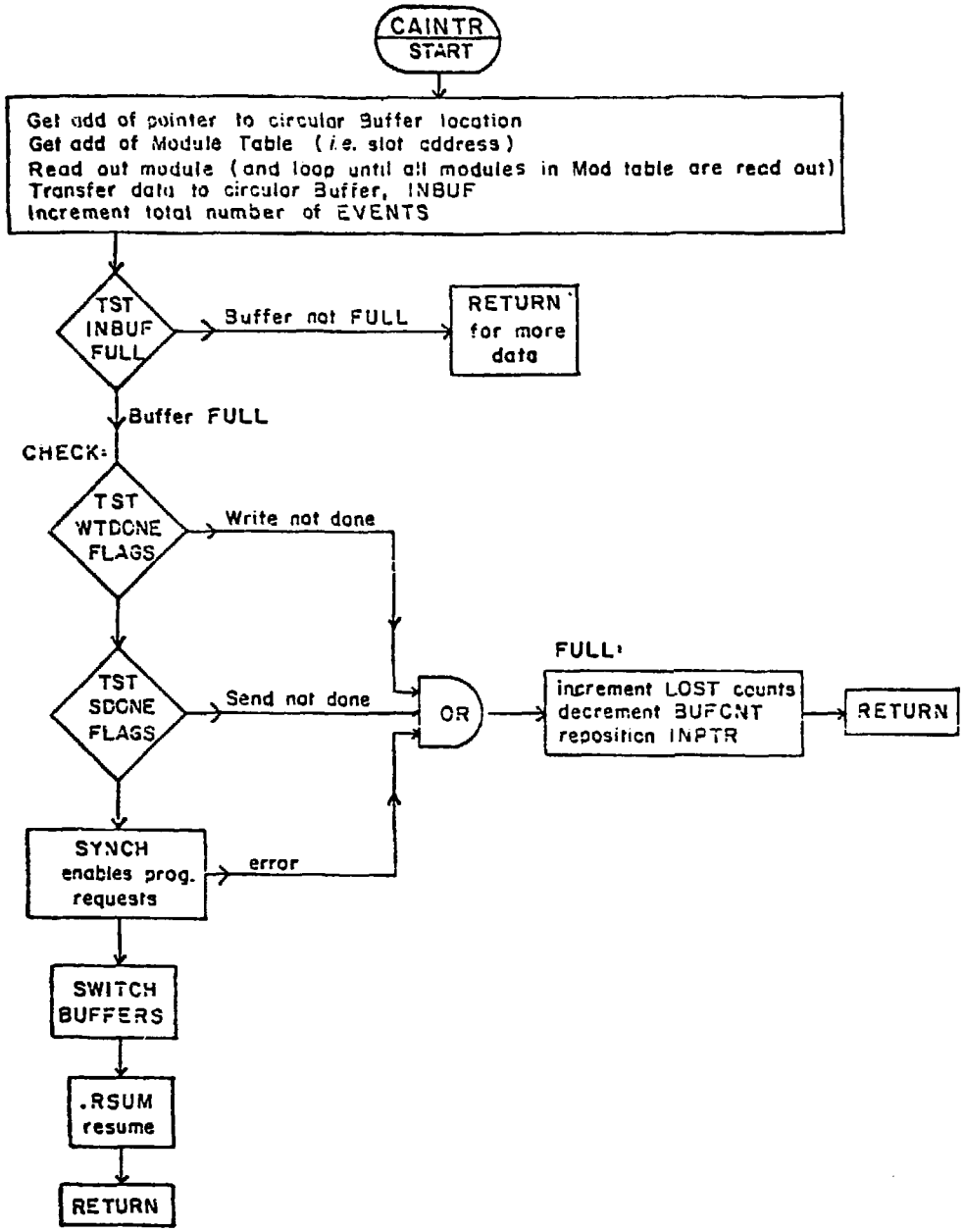
CAINTR
START
Get add of pointer to circular Buffer location
Get add of Module Table (i.e. slot address)
Read out module (and loop until all modules in Mod table are read out)
Transfer data to circular Buffer, INBUF
Increment total number of EVENTS
TST INBUF FULL
Buffer not FULL
RETURN for more data
Buffer FULL
CHECK:
TST WTDONE FLAGS
Write not done
TST SDONE FLAGS
Send not done
OR
FULL:
increment LOST counts
decrement BUFCNT
reposition INPTR
RETURN
SYNCH enables prog. requests
error
SWITCH BUFFERS
.RSUM resume
RETURN

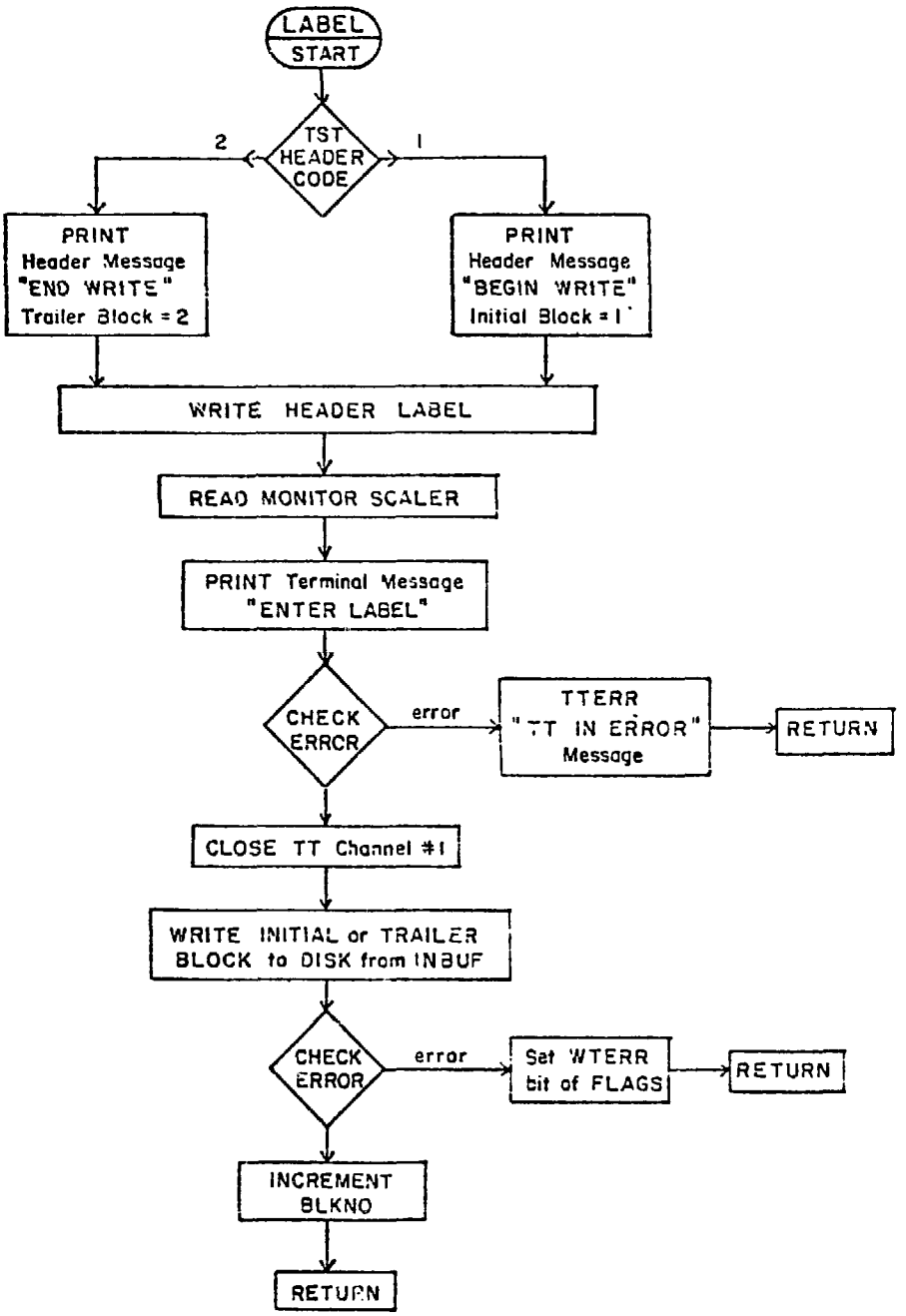
LABEL START
TST HEADER CODE
2
1
PRINT Header Message "END WRITE" Trailer Block = 2
PRINT Header Message "BEGIN WRITE" Initial Block = 1
WRITE HEADER LABEL
READ MONITOR SCALER
PRINT Terminal Message "ENTER LABEL"
CHECK ERRCR
error
TTERR "TT IN ERROR" Message
RETURN
CLOSE TT Channel #1
WRITE INITIAL or TRAILER BLOCK to DISK from INBUF
CHECK ERROR
error
Set WTERR bit of FLAGS
RETURN
INCREMENT BLKNO
RETURN

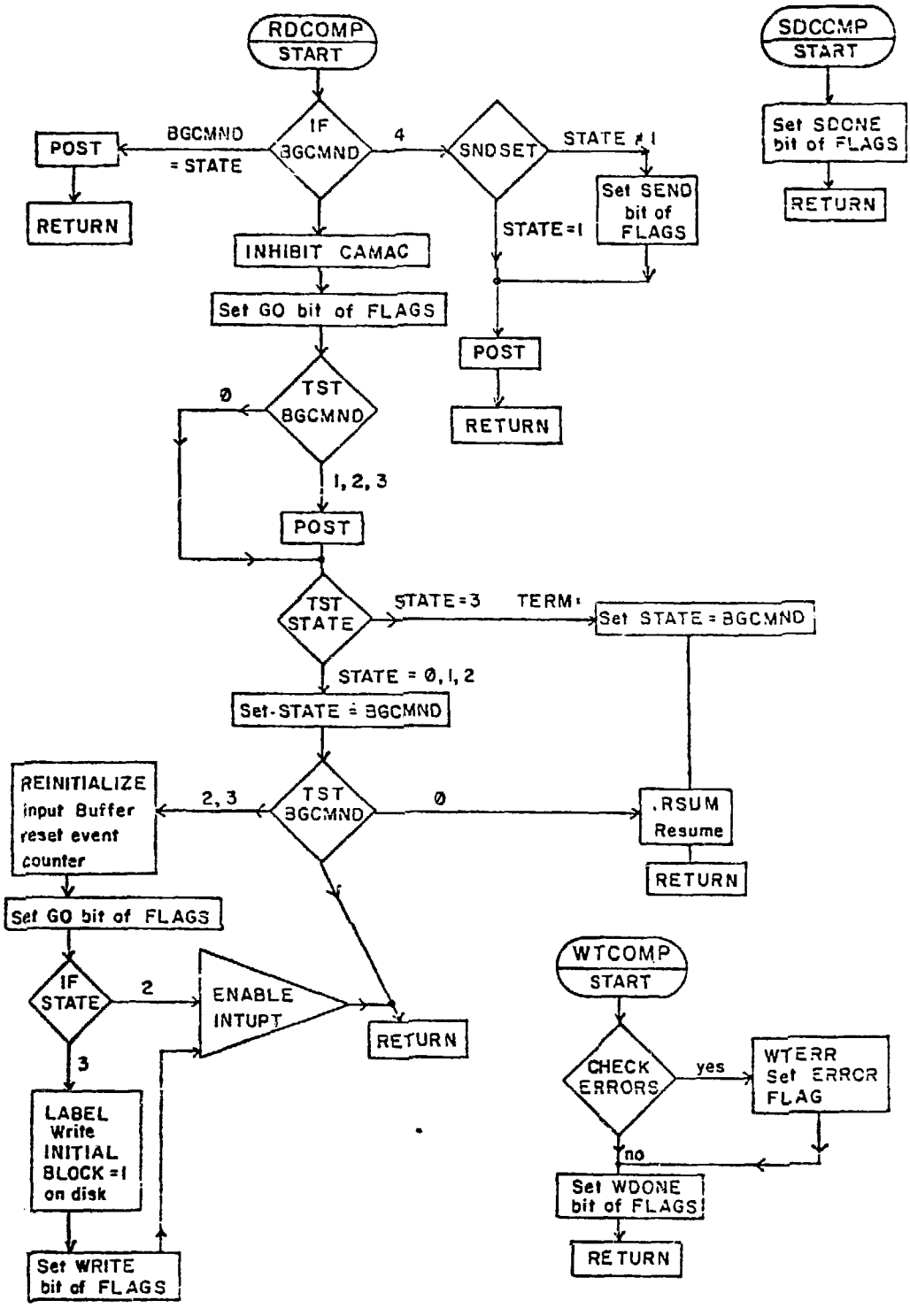
RDCOMP START
IF BGCMND
BGCMND = STATE
POST
RETURN
4
SNDSET
STATE ≠ 1
Set SEND bit of FLAGS
STATE=1
INHIBIT CAMAC
Set GO bit of FLAGS
POST
RETURN
TST BGCMND
0
1, 2, 3
POST
SDCCMP START
Set SDONE bit of FLAGS
RETURN
TST STATE
STATE=3
TERM
Set STATE = BGCMND
STATE = 0, 1, 2
Set-STATE = BGCMND
REINITIALIZE input Buffer reset event counter
2, 3
TST BGCMND
0
.RSUM Resume
RETURN
Set GO bit of FLAGS
IF STATE
2
ENABLE INTUPT
RETURN
3
LABEL Write INITIAL BLOCK =1 on disk
Set WRITE bit of FLAGS
WTCOMP START
CHECK ERRORS
yes
WTERR Set ERROR FLAG
no
Set WDONE bit of FLAGS
RETURN

REFERENCES

1. C. M. G. Lattes, H. Muirhead, G. P. S. Occhialini, and C. F. Powell, Nature 159, 694 (1947).
2. D. S. Koltun, Adv. Nucl. Phys. 3, 71 (1969).
3. J. M. Eisenberg in Proc. LAMPF Summer School on Pion-Nucleus Scattering, eds. W. R. Gibbs and B. F. Gibson, Los Alamos Scientific Laboratory Report, LA-5443-C (1973).
4. M. M. Sternheim and R. R. Silbar, Ann. Rev. Nucl. Sci. 24, 249 (1974).
5. J. Hufner, Phys. Repts. 21C, 1 (1976).
6. F. Becker and Y. A. Batusov, Rivista Nuov. Cim. 1, 309 (1971).
7. N. Kemmer, Proc. Roy. Soc. A166, 127 (1938); also, Proc. Camb. Phil. Soc. 34, 354 (1938).
8. H. L. Anderson, E. Fermi, E. A. Long, R. Martin, and D. E. Nagle, Phys. Rev. 85, 934 (1952); H. L. Anderson, E. Fermi, E. A. Long, and D. E. Nagle, Phys. Rev. 85, 936 (1952); H. L. Anderson, E. Fermi, R. Martin, and D. E. Nagle, Phys. Rev. 91, 155 (1953).
9. A. A. Carter, J. R. Williams, D. V. Bugg, P. J. Bussey, and D. R. Dance, Nucl. Phys. B26, 445 (1971).
10. G. Bizard, J. Duchon, J. Seguinot, J. Yonnet, P. Bareyre, C. Bricman, G. Valladas, and G. Villet, Nuov. Cim. 44A, 999 (1966).
11. T. J. Devlin, J. Solomon, and G. Bertsch, Phys. Rev. Lett. 14, 1031 (1965).

12. W. W. Lock and D. F. Measday in Intermediate Energy Nuclear Physics, p. 101 (Methuen, London, 1970).

13. A. Donnachie, Proc. 14th Int. Conf. on High-Energy Physics, Vienna (1968), p. 139 (CERN, Geneva, 1968).

14. A. H. Rosenfeld, N. Barash-Schmidt, A. Barbaro-Galtieri, L. R. Price, P. Soding, C. G. Wohl, M. Roos, and W. J. Willis, Rev. Mod. Phys. 40, 77 (1968).

15. F. de Hoffman, N. Metropolis, and E. F. Alei, Phys. Rev. 95, 1586 (1954).

16. J. B. Walter, private communication.

17. N. D. Gabitzsch, G. S. Mutchler, C. R. Fletcher, E. V. Hungerford, L. Coulson, D. Mann, T. Witten, M. Furic, G. C. Phillips, B. Mayes, L. Y. Lee, J. Hudomalj, J. C. Allred, and C. Goodman, Phys. Lett. 47B, 234 (1973).

18. K. M. Watson, Phys. Rev. 89, 575 (1953).

19. T. P. Kopaleishvili, Particles and Nuclei, Vol. 2, Part 2, 87 (1973).

20. T. Berggren and H. Tyren, Ann. Rev. Nucl. Sci. 16, 153 (1966).

21. G. Jacob and Th. A. J. Maris, Rev. Mod. Phys. 38, 121 (1966).

22. R. Serber, Phys. Rev. 72, 1114 (1947).

23. C. Zupancic, Rev. Mod. Phys. 37, 330 (1965).

24. R. R. Silbar, Phys. Rev. C11, 1610 (1975).

25. R. M. Frank, J. L. Gammel, and K. M. Watson, Phys. Rev. 101, 891 (1956).

26. H. A. Thiessen and S. Sobottka, 'A Proposal for EPICS: A High Resolution Pion Beam and Spectrometer Facility for Nuclear Structure Research at LAMPF,' Los Alamos Scientific Laboratory Report, LA-4534-MS.

27. P. L. Reeder and S. S. Markowitz, Phys. Rev. 133, B639 (1964).

28. A. M. Poskanzer and L. P. Remsberg, Phys. Rev. 134, B779 (1964).

29. C. O. Hower and S. Kaufman, Phys. Rev. 144, 917 (1966).

30. V. M. Kolybasov, Yad. Fiz 2, 144 (1965) [English translation: Sov. J. Nucl. Phys. 2, 101 (1966)].

31. O. D. Dalkarov, Phys. Lett. 26B, 610 (1969).

32. F. Selleri, Phys. Rev. 164, 1475 (1967).

33. D. T. Chivers, E. M. Rimmer, B. W. Allardyce, R. C. Witcomb, J. J. Domingo, and N. W. Tanner, Nucl. Phys. A126, 129 (1969).

34. M. A. Moinester, M. Zaider, J. Alster, D. Ashery, S. Cochavi, and A. I. Yavin, Phys. Rev. C8, 2039 (1973).

35. P. J. Karol, A. A. Caretto, Jr., R. L. Klobuchar, D. M. Montgomery, R. A. Williams, and M. V. Yester, Phys. Lett. 44B, 459 (1973).

36. M. V. Yester, A. A. Caretto, Jr., M. Kaplan, P. J. Karol, and R. L. Klobuchar, Phys. Lett. 45B, 327 (1973).

37. M. Zaider, J. Alster, D. Ashery, M. A. Moinester, and A. I. Yavin, Phys. Rev. C10, 938 (1974).

38. B. J. Lieb, H. S. Plendl, H. O. Funsten, W. J. Kossler, and C. E. Stronach, Phys. Rev. Lett. 34, 965 (1975).

39. N. P. Jacob, Jr. and S. S. Markowitz, Phys. Rev. C13, 754 (1976).

40. B. J. Dropesky, G. W. Butler, C. J. Orth, R. A. Williams, G. Friedlander, M. A. Yates, and S. B. Kaufman, Phys. Rev. Lett. 34, 821 (1975).

41. L. H. Batist, V. D. Vitman, V. P. Koptev, M. M. Makarov, A. A. Naberezhnov, V. V. Nelyubin, G. Z. Obrant, V. V. Sarantsev, and G. V. Scherbakov, Nucl. Phys. A254, 480 (1975).

42. P. W. Hewson, Nucl. Phys. A133, 659 (1969).

43. D. Robson, Ann. Phys. 71, 277 (1972).

44. D. H. Wilkinson, J. Phys. Soc. Jap., Suppl. 24, 469 (1968).

45. V. M. Kolybasov, Phys. Lett. 27B, 3 (1968); V. M. Kolybasov and N. Ya. Smorodinskaya, Phys. Lett. 30B, 11 (1969).

46. R. Seki, Nuov. Cim. 9A, 235 (1972).

47. M. M. Sternheim and R. R. Silbar, Phys. Rev. Lett. 34, 824 (1975).

48. J. E. Monahan and F. J. D. Serduke, Phys. Rev. Lett. 36, 224 (1976).

49. H. Plendl and A. Rechter (private communication).

50. P. J. Karol, Phys. Rev. Lett. 36, 338 (1976).

51. R. R. Silbar, J. N. Ginocchio, and M. M. Sternheim, Phys. Rev. C15, 371 (1977).

52. R. R. Silbar and D. M. Stupin, Phys. Rev. C12, 1089 (1975).

53. M. M. Sternheim and R. R. Silbar, Phys. Rev. D6, 3117 (1972).

54. P. Varghese, R. R. Silbar and M. M. Sternheim, Phys. Rev. C14, 1893 (1976).

55. QUASEX is a modified version of the co developed by Silbar and Stupin (Ref. 52).

56. These chambers were constructed by Ed McCrea at Oregon State University.

57. D. M. Lee, S. E. Sobottka, and H. A. Thiessen, Los Alamos Scientific Laboratory Report, LA-5617-MS.

58. H. A. Thiessen, J. C. Kallne, J. F. Amann, R. J. Peterson, S. J. Greene, S. L. Verbeck, G. R. Burleson, S. G. Iverson, A. W. Obst, K. K. Seth, C. F. Moore, J. E. Bolger, W. J. Braithwaite, D. C. Slater, and C. L. Morris, Los Alamos Scientific Laboratory Report, LA-6663-MS.

59. Data acquisition program developed by Kurt Kohler.

60. Online analysis program written by Mark Greenfield with additions and modifications by T. C. Sharma and P. Varghese.

61. Measured in Experiment #93 at LAMPF.

☆ U.S. GOVERNMENT PRINTING OFFICE 1978—677-013/192